République Algérienne Démocratique et Populaire
Ministère de l'Enseignement Supérieure et de la Recherche Scientifique
Université Mohamed Khider - Biskra

Faculté des Science et de la technologie
Département: chimie industrielle

Ref : ……..

Thèse Présentée en vue de l'obtention du Diplôme de

Doctorat en Génie des Procédés
Option : Génie des Matériaux

Synthèse et caractérisation des couches minces à base d'oxyde pour l'application photocatalytique

Présentée par :

Nourelhouda Mokrani

Soutenue publiquement le : …. / …. / 2025

Devant le jury compose de :

Pr. Saâd RAHMANE	**Professeur**	**Université de Biskra**	**Président**
Dr. Elhachmi GUETTAF TEMAM	**M.C.A**	**Université de Biskra**	**Encadreur**
Pr. Hachemi BEN TEMAM	**Professeur**	**Université de Biskra**	**Co encadreur**
Pr. Abdelkrim MERZOUGUI	**Professeur**	**Université de Biskra**	**Examinateur**
Dr. Fouad KERMICHE	**M.C.A**	**Ecole Normale Supérieur de Sétif**	**Examinateur**

Democratic and People's Republic of Algeria
Ministry of Higher Education and Scientific Research
Mohamed Khider University – Biskra

Faculty of Science and Technology
Department: industrial chemistry

Ref : ……..

Thesis Presented with a view to obtaining the Diploma of

Doctorate in Process Engineering
Option: Materials Engineering

Synthesis and characterization of oxide-based thin films for photocatalytic application

Presented by:
Nourelhouda Mokrani

Publicly supported on: …. / …. / 2025

Before the jury composed of:

Pr. Saâd RAHMANE	**Professor**	**University of Biskra**	**President**
Dr. Elhachmi GUETTAF TEMAM	**M.C.A**	**University of Biskra**	**Supervisor**
Pr. Hachemi BEN TEMAM	**Professor**	**University of Biskra**	**Co Supervisor**
Pr. Abdelkrim MERZOUGUI	**Professor**	**University of Biskra**	**Examiner**
Dr. Fouad KERMICHE	**M.C.A**	**High Education School Setif**	**Examiner**

Dedication

With deepest reverence and heartfelt devotion, I dedicate this doctoral dissertation to the cherished of my beloved parents, whose unwavering dedication to excellence and discipline shaped the very essence of my journey, guiding me to this pinnacle of achievement.

I am very grateful to my parents and sisters: **Lobna, Zineb, Kaltoum and Saoussan** and two brothers for their support, encouragement and above all their unconditional love which has always been a motivation source. Your prayers for me was what sustained me this far. Thanks to my brother's wife for always supporting me, not forgetting the children at home who make the times sweeter: **Nedhal, Assinat, Ilyes**.

Finally, I owe thanks to my friends who gave me a considerable emotional support (even remotely) and encouragements during my pursuit of Ph.D. degree that made the completion of thesis possible.

Acknowledgments

At the end of my PhD journey, I would like to express my sincere gratitude to all the people who had a contribution to this work and made it possible through their support and advice.

I sincerely thank Dr. **Elhachmi Guettaf Temam**, the supervisor of this thesis, for his help and support to overcome all the difficulties and put together all the pieces to make this project finally work. I would like thank Professor **Hachemi Ben Temam** co-supervisor of this thesis, not only for his enlightening advice and for generous support, but also for his extreme kindness, on personal and professional level as well.

I would like to thank the president members of the jury: Professor **Saâd RAHMANE** (University of Biskra), for having accepted to evaluate this thesis and sharing with me his huge knowledge. I am deeply grateful to **Dr. Fouad Kermiche** (High Education School Setif) and Professor **Merzougui Abdelkrim** (University of Biskra) who accepted to examiners this Ph.D. thesis.

I spent most of my time in the Physics Laboratory of Thin Layers and Applications (PTLA) laboratory of the research laboratories of the University of Biskra where I completed the majority of the work in this thesis. Everyone in PTLA has supported me in a way or two. I thank engineer **Brahim Gasmi, Hanane Touhami** and **Prof Abdelouahab Ouahab** for their help on experimental setup, technical issues and sample characterizations as well as the many fruitful scientific discussions. Their time and efforts were indispensable for my thesis to proceed. I am also thankful for all the other members of PTLA who have contributed to my work via different manners.

All my colleagues of the PTLA (with special thanks to **Hadjer Barkat, Ouarda Ben Massoud, Lamya Lahag, Linda Abdelli, Imane Saoula, Fatima Djenidi, Mohammad Althamthami and Okba Ben Khetta**) I had the good fortune to meet during the three years of this Ph.D. thesis

Abstract

The development of Sr-doped ZnO thin films using the Successive Ionic Layer Adsorption and Reaction (SILAR) method represents a significant step forward in advancing photocatalytic materials for environmental remediation. This study systematically investigates the effects of varying Sr concentrations (1, 3, 5, and 7 wt.%) on the structural, optical, and photocatalytic properties of ZnO thin films. X-ray diffraction analysis confirmed the polycrystalline nature of the films; with an observed increase in crystallite size along the (100) plane as Sr doping concentration increased. Notably, films with 5 wt.% Sr displayed exceptional photocatalytic efficiency under natural sunlight, achieving methylene blue degradation rates of up to 94.82% over three cycles, demonstrating remarkable stability and reusability. The photocatalytic activity of these films extended to the degradation of rose bengal and was particularly effective under basic pH conditions, with a maximum degradation rate of 97.60% achieved by films containing 40 wt.% Sr. Optical studies revealed that Sr doping led to a linear increase in the bandgap energy, enhancing the films' light absorption and electron-hole pair generation. Additionally, the integration of chemical additives, including ethylene glycol (EG), polyethylene glycol (PEG), ethylenediaminetetraacetic acid (EDTA), ethanolamine (EA), sodium dodecyl sulfate (SDS), and butynediol (BD), was explored to further tailor the films' properties. These additives influenced the films’ morphology, hydrophilicity, and photocatalytic performance, with EA-incorporated films achieving 92.53% degradation of methylene blue and EDTA-modified films showing a notable 23.68% degradation of amoxicillin. The research also highlighted the interplay between doping and additives in modulating structural and optical characteristics. While Sr doping enhanced crystallinity and photocatalytic activity, certain additives reduced the bandgap energy and improved hydrophilicity, critical for pollutant adsorption and photocatalysis. Furthermore, this study emphasizes the potential of Sr-doped ZnO thin films for diverse environmental applications, particularly in water purification and wastewater treatment. Future work could explore the integration of these films with heterojunctions or advanced nanostructures to further optimize their performance.

Keywords: Sr-doped ZnO, SILAR, Photocatalysis, Methylene blue, Rose bengal, XRD, Additives, Water purification, Hydrophilicity.

Table of Contents

Chapter I : Scientific Background

Chapter II : Development and Characterization of Pure ZnO and ZnO/Sr Thin Films by SILAR Method

Chapter III : Enhancing Photocatalytic Stability of Hydrophilic Sr-Doped ZnO Thin Films via SILAR Method

Chapter IV: Impact of High Strontium Concentrations on the Structure of Zinc Thin Films and Their Application in Degrading Methylene Blue and Rose Bengal

Chapter V : Effect of Different Additives on Sr-doped ZnO Thin Films For The Removal of MB and AMX Using The Photocatalytic Process

List of abbreviations and symbols

SILAR	Successive Ionic Layer Adsorption and Reaction
XRD	X-ray diffraction
UV-vis	Ultraviolet-Visible spectroscopy
UVI	ultraviolet index
SEM	Scanning electron microscopy
EDS	Energy Dispersive X-ray
AFM	Atomic force microscope
FWHM(β)	Full width half maximum
ϑ	Diffraction angle
K	shape factor
D	crystallite size
N	number of crystallites
T	thickness of the film
Δ	dislocation density
a, b, c	lattice parameter
Ra	Arithmetic mean roughness (g/ml)
Rq	Root-mean-square roughness (nm)
Rsk	Skewness (nm)
Rku	Kurtosis (nm)
Θ	Angle of the water droplet (°)
ϑ_1,ϑ_2	Left (1)and Right(2) angle of the water droplet
M	Mass of the film in (g)
Eg	Bandgap Energy
H	Planck's constant
N	Radiation frequency
A	Relates the absorptivity
A	Constant independent of energy
CB	Conduction band
CV	Valence band
C_t	concentration at time t (mmol/L or ppm)
C_0	Initial concentration (mmol/L or ppm)
T	Time
ROS	Reactive oxygen species
e-	Electron
h^+	Hole
$O^{\cdot -}$	Superoxide
$OH^{\cdot}$	Hydroxyl radicals
R	Rate
k_{app}	Pseudo 1st rate constant (h-1)
K_L	langmuir constant
S_{MB}	specific surface area(MB)
MB	Methylene Blue

AMX	Amoxicillin
AB	Antibiotic
RB	Rose bangal
DW	Double distilled water
ZnO	Zinc Oxide
Sr	Strontium
NaOH	Sodium hydroxide
HCl	Hydrochloric acid
H_2O_2	Hydrogen peroxide
EDTA	Ethylenediaminetetraacetic acid
EA	Ethanolamine
EG	Ethylene glycol
PEG	Polyethylene glycol
SDS	Sodium dodecyl sulfate
BD	2-Butyne-1,4-diol
wt %	Weight Percentage

List of tables

Chapter II

Chapter III

Chapter IV

Chapter V

List of figures and Schemes

Chapter I

Chapter II

Chapter III

Chapter IV

Chapter V

General introduction

Harmful pollutants from industrial activities pose significant threats to aquatic ecosystems, groundwater quality, and the health of humans, animals, and plants. Contaminated water typically contains high levels of heavy metals, pharmaceutical residues, dyes, and other pollutants. Dye contamination can cause health issues such as skin irritation, respiratory problems, nausea, and even cancer. Methylene Blue (MB), a cationic azo dye, is an affordable organic compound widely used in various applications. It is primarily employ in the production of inks and in medical applications. Water recycling is an effective solution to address water shortages and manage wastewater. The water can be reuse for domestic purposes by eliminating organic pollutants through a photocatalytic process.

Photocatalysis represents a highly promising technological approach for the abatement of environmental contaminants [1]. While efficient, sustainable, and ecologically compatible, photocatalysis requires significant advancements in material design to overcome limitations and improve industrial applicability [2].This process is environmentally sustainable, harnessing renewable solar energy and producing no harmful by-products [3.].Tailoring the optical and morphological properties of photocatalytic materials can enhance their efficacy for various applications [4]Optimizing these materials is crucial for improving photocatalytic systems in environmental remediation and sustainable energy applications [5].Among these materials, zinc oxide is widely used because of its non-toxicity and abundance in nature [6].

Zinc oxide (ZnO) is widely used in photocatalysis for pollutant degradation, water splitting, and CO_2 reduction [7]. Its wide bandgap (3.37 eV) [8, 9, 10, 11], however, restricts light absorption to the ultraviolet spectrum (<400 nm), which accounts for only 3–5% of solar radiation, limiting its solar energy utilization [12]. Additionally, the rapid recombination of photogenerated electron-hole pairs and slow surface water oxidation kinetics further hinder its efficiency and practical application [13]. Various strategies, including element doping, quantum dot sensitization, noble metal deposition, heterostructure construction, and cocatalyst integration, have been explore to address these challenges. Recent studies focus on enhancing ZnO's photocatalytic performance by doping it with elements like aluminum [14], nickel [15], iron [16], manganese [17], copper, and strontium. Doped zinc oxide thin films have gained significant attention as transparent conducting electrode materials. Various deposition techniques have been utilized to fabricate doped zinc oxide thin films, including chemical vapor deposition (CVD) [18], magnetron sputtering [19], pulsed laser deposition (PLD) [20], spray pyrolysis [21], and the successive ionic layer adsorption and reaction (SILAR) method [22,23,24].

In the last three decades, the Successive Ionic Layer Adsorption and Reaction (SILAR) method has emerged as a versatile solution-based technique for thin-film deposition. This method is cost-effective, straightforward, and suitable for large-area deposition [25]. It supports various substrates, including insulators, semiconductors, metals, and temperature-sensitive materials like polyester, as the deposition process occurs at or near room temperature [26]. The low-temperature SILAR process prevents substrate oxidation and corrosion, making it highly attractive. Producing high-quality thin films requires optimizing conditions like precursor concentrations, complexing agents, solution pH, and the durations of adsorption, reaction, and rinsing [27]. This thesis discusses the preparative parameters, structural and optical properties of the films, and the theoretical principles of the SILAR method.

While many studies have reported the synthesis of ZnO thin films for photocatalytic applications [28,29,30,31], few have explored the effect of strontium added concentration to Zn on the degradation of dyes [32]. To the best of our knowledge, no prior research has examined how variations in Sr concentration combined with different additives influence the degradation rate. In this study, we prepared strontium-added ZnO thin films on a glass substrate via SILAR by dip-coating technique and studied the effect of strontium added concentrations on the properties of ZnO thin films. The main objective of this research is to find the optimum concentration of strontium dopant that gives high properties suitable for the Sr-doped ZnO thin films for application in photocatalysis. The aim and novelty of this work are developed in the next section.

Objectives of the Ph.D. work and Manuscript outline

The primary objective of my thesis is to investigate the effect of strontium concentration on the properties of ZnO for photocatalytic applications. The degradation mechanisms were investigated on different pollutant molecules (methylene blue, rose bangal and amoxicillin) over pure ZnO and Sr/ZnO thin films. Films were synthesized by finely tuning the solution parameters such as temperature, acidity and strontium concentration. Different concentration of strontium, were deposited on glass substrates via SILAR method by dip coating technique. With the characterization techniques available in the PTLA laboratory in the University of

BISKRA (SEM, EDX, XRD, UV-vis, profilometer) the properties will be studied by morphological, structural and optical studies of the layers. The findings of this study offer important insights into the advancement of highly efficient photocatalytic systems for environmental remediation. These themes are explored in greater detail in the subsequent chapter.

In chapter I provides the general context and essential bibliographical information necessary to understand the study. The initial section will cover the qualities of zinc oxide, focusing on its properties and applications. The subsequent section examines strontium, highlighting its intrinsic characteristics, including crystallographic network structure, optical attributes, and morphological properties. It also emphasizes the significant role of stimulants, particularly the effects of concentration on the various properties of the material. Additionally, this chapter discusses thin films and their applications, especially those made of zinc. Finally, it explores some applications of doped zinc oxide in various fields, particularly in water purification through photocatalytic methods, including the application of our work.

The chapter II presents experimental details on the deposition of thin films of pure ZnO and Sr-doped ZnO on glass substrates using the SILAR method, along with the preparation of solutions. It also discusses various characterization techniques to analyze the structural, morphological, and optical properties of the thin films, specifically X-ray diffraction (XRD), scanning electron microscopy (SEM), atomic force microscopy (AFM), mechanical profilometer, and UV-Vis spectroscopy. In addition, it provides a detailed experimental method for photocatalytic applications and describes the technique used in this study to determine the water contact angle, which involved the use of the sitting water droplet method.

Chapter III investigated the structural, optical, wettability, and photocatalytic properties of ZnO films with varying concentrations of strontium (0, 1, 3, 5, and 7 wt.%) prepared using the SILAR technique. The results indicated that Sr-doped ZnO thin films, particularly those with 5 wt.% Sr, exhibited enhanced photocatalytic activity, achieving an impressive 94.82% degradation of methylene blue under sunlight. Additionally, these films demonstrated excellent stability and reusability over three cycles, emphasizing their potential for environmental applications, especially in water treatment and pollutant degradation.

The chapter IV demonstrates the successful synthesis of Sr-doped ZnO thin films using the SILAR technique, highlighting its simplicity, affordability, and effectiveness. A novel aspect of this study is the production of ZnO thin films with high concentrations of strontium doping (0, 20, 40, 60, and 80 wt.%). The performance of these films will be evaluated by examining their photocatalytic efficiency in degrading methylene blue (MB) and rose bengal (RB) under natural sunlight. Furthermore, the study will investigate the degradation of methylene blue in the presence of hole scavengers and varying solution acidity to assess the films' effectiveness under different conditions, particularly in the sample with 40 wt.% Sr.

Chapter V presents a detailed comparative analysis of the influence of various additives (EG, PEG, EA, EDTA, BD, and SDS) on the structural, morphological, optical, and surface characteristics of Sr-doped ZnO (5 wt.%) thin films synthesized via the Successive Ionic Layer Adsorption and Reaction (SILAR) technique. The incorporation of different additives was systematically linked to modifications in the crystal structure, surface roughness, and optical properties of the ZnO:Sr layers, demonstrating their critical role in tuning photocatalytic efficiency. Particularly those with EA exhibited enhanced photocatalytic activity, achieving an impressive 92.53% degradation of methylene blue under sunlight. By tailoring these properties, the additives enabled enhanced light absorption, charge carrier dynamics, and surface activity, which are pivotal for the photocatalytic degradation of organic pollutants, specifically methylene blue (MB) and amoxicillin (AMX).

The key findings of this thesis have been identified and discussed in the general conclusion, along with proposed future directions stemming from this doctoral research.

References of general introduction

[1] Abuzeyad, Osama H., et al. "Merits photocatalytic activity of rGO/zinc copper ferrite magnetic nanocatalyst for photodegradation of methylene blue (MB) dye." *Discover Nano* 20.1 (2025): 1-16.

[2] Wazzan, Ghaida M., et al. "Annealing Temperature Effects of Seeded ZnO Thin Films on Efficiency of Photocatalytic and Photoelectrocatalytic Degradation of Tetracycline Hydrochloride in Water." *Catalysts* 15.1 (2025): 71

[3] Mageswari, Kumar, et al. "Enhancement of Photocatalytic and Antimicrobial Properties of SHMP-capped with Ni and Gd-Doped Zinc oxide nanoparticles." *Hybrid Advances* (2025): 100377

[4] Tebbi, Sara Oumenoune, et al. "Green Synthesis of Sustainable and Cost-Effective TiO2-SiO2-Fe2O3 Heterojunction Nanocomposites for Rhodamine B Dye Degradation Under Sunlight." *Water* 17.2 (2025): 168.].

[5] Faaizatunnisa, Nuhaa, et al. "Optimized photocatalytic degradation of 2-naphthol using ZnO/rGO nanocomposites synthesized from palm kernel shell waste." *Journal of Water Process Engineering* 70 (2025): 106977.

[6] Haritha, A. H., et al. "Influence of annealing temperature on the photocatalytic efficiency of sol-gel dip-coated ZnO thin films in methyl orange degradation." *Open Ceramics* 21 (2025): 100727

[7] Singsumphan, Kittiyaporn, et al. "Low-voltage electrophoretic deposition of silver nanoparticles on ZnO nanorods thin films for enhanced visible-light photocatalysis." *Optik* 322 (2025): 172179

[8] Ahmed, Sohail, et al. "A nanosized crack-free thin film of ZnO synthesis by AACVD method for photoelectrochemical green hydrogen production." *International Journal of Hydrogen Energy* 100 (2025): 792-799.

[9] Podia, Mohit, and Awnish Kumar Tripathi. "Role of shallow donor defects in inducing broad visible Photoluminescence in ZnO thin film." *Journal of Luminescence* (2025): 121083.

[10] Akash, R., et al. "Fabrication of high-performance UV photodetector using Gallium doped ZnO thin films by Nebulizer Spray Pyrolysis method." *Optical Materials* (2025): 116715

[11] Benrezgua, Elhadj, et al. "Synthesis of low-content Mn-doped ZnO thin films: Characterizations and density functional theory studies." *Inorganic Chemistry Communications* 172 (2025): 113710.

[12] Yang, Lili, et al. "Fabrication of composite structures for full spectrum photon management in solar energy utilization." *Thin Solid Films* 752 (2022): 139250

[13] Wang, Pan, Gabriel Benitez, and Frances Houle. "Influence of hole transport and thermal reactions in photo-driven water oxidation kinetics on crystalline TiO2." (2024).

[14] Transformation of cadmium hydroxide to cadmium oxide thin films synthesized by SILAR deposition process: Role of varying deposition cycles

[15] Khan, Muhammad Amer Saeed, et al. "Band gap tunability in DC sputtered Ni-doped ZnO thin films for wide usage in optoelectronic gadgets." *Physica B: Condensed Matter* 686 (2024): 416076.

[16] Battas, Manale, et al. "Light scattering effect of iron doped zinc oxide thin films through structural and optical analysis." *Optik* 255 (2022): 168704

[17] Vallejo, William, Alvaro Cantillo, and Carlos Díaz-Uribe. "Improvement of the photocatalytic activity of ZnO thin films doped with manganese." *Heliyon* 9.10 (2023).

[18] El Khouja, Outman, et al. "Investigation of structural and optical properties of Mg doped ZnS thin films prepared by Mist-CVD technique: Experimental and theoretical aspects." *Materials Chemistry and Physics* 313 (2024): 128707.

[19] Muthitamongkol, P., et al. "The effects of the argon plasma treatments on transparent conductive aluminum-dope zinc oxide thin films prepared by the pulsed DC magnetron sputtering." *Materials Today: Proceedings* 4.5 (2017): 6248-6253.

[20] Wang, Song, et al. "Ultraviolet-A-transparent aluminum-doped zinc oxide thin film electrodes by pulsed laser deposition." *iScience* (2025).

[21] Fernandes, MatheusHorstmann, et al. "Chloride-doped ZnO thin films prepared by spray pyrolysis: effects on microstructural, optical, and photocatalytic properties." *Micro and Nanostructures* 177 (2023): 207550.

[22] Yücel, Yasin, ÖmerOtuzbir, and ErsinYücel. "Surface roughness prediction in SILAR coating process of ZnO thin films: Mathematical modelling and validation." *Materials Today Communications* 34 (2023): 105101.

[23] Khan, Mohd Taukeer, et al. "Enhancement of photodetector performance of aluminum-doped zinc oxide thin films fabricated via SILAR method: Structural, optical, and electrical analysis." *Inorganic Chemistry Communications* 169 (2024): 112973.

[24] Nkamuo, C. J., et al. "Tuning the properties of manganese-doped zinc oxide nanostructured thin films deposited by SILAR approach." *Chemistry of Inorganic Materials* 2 (2024): 100038.

[25] Khan, Mohd Taukeer, et al. "Enhancement of photodetector performance of aluminum-doped zinc oxide thin films fabricated via SILAR method: Structural, optical, and electrical analysis." *Inorganic Chemistry Communications* 169 (2024): 112973

[26] Patwary, Md Abdul Majed. "Thin Films Processed by SILAR Method." *Thin Films-Deposition Methods and Applications*. IntechOpen, 2022

[27] Nwanya, A. C., et al. "Transformation of cadmium hydroxide to cadmium oxide thin films synthesized by SILAR deposition process: Role of varying deposition cycles." *Journal of the Association of Arab Universities for Basic and Applied Sciences* 20.1 (2016): 49-54.

[28] Ibraheem, A. Mohamed, and J. Kamalakkannan. "Sustainable scientific advancements modified Ag2O-ZnO thin films characterization and application of photocatalytic purification of carcinogenic dye in deionizer water and contaminated sea water solutions and synthetic, natural based dye-sensitized solar cells." *Materials Science for Energy Technologies* 3 (2020): 183-192.

[29] Daher, Elie A., et al. "New approach for designing wrinkled and porous ZnO thin films for photocatalytic applications." *Colloids and Surfaces A: Physicochemical and Engineering Aspects* 658 (2023): 130628.

[30] Karakaya, Seniye, and Leyla Kaba. "Wrinkle type nanostructured of Al-Ce co-doped ZnO thin films for photocatalytic applications." *Surfaces and Interfaces* 44 (2024): 103655.

[31] Haritha, A. H., et al. "Influence of annealing temperature on the photocatalytic efficiency of sol-gel dip-coated ZnO thin films in methyl orange degradation." *Open Ceramics* 21 (2025): 100727.

[32] Javaid, Alqa Saeeda, et al. "Synthesis and characterization of efficient Sr-doped ZnO nanostructures for optoelectronic, and photocatalytic applications." *Inorganic Chemistry Communications* 162 (2024): 112175.

Chapter I:

Scientific Background

I.1. Introduction

Zinc oxide (ZnO) is an exceptional semiconductor material, widely recognized for its outstanding physical and chemical properties, which make it suitable for a broad spectrum of applications. This chapter establishes the context of the study and provides the essential bibliographical background required to understand the research.

The discussion begins by exploring the remarkable properties of ZnO, focusing on its crystallographic structure, optical attributes, and the versatility it demonstrates across various fields, including electronics, catalysis, and environmental remediation. The introduction then transitions to an examination of strontium (Sr), a vital element known for its unique characteristics. Emphasis placed on its crystallographic framework, optical properties, and its ability to modulate material performance through doping, with particular attention to its role as a stimulant in enhancing the functional attributes of ZnO.

The chapter concludes by highlighting the synergy between ZnO and strontium through doping, which has demonstrated significant potential in photocatalytic applications, particularly for environmental remediation, such as water purification. This fusion of ZnO's inherent properties with Sr doping opens new frontiers for advanced technological applications, setting the stage for further exploration in subsequent chapters.

I.2. Zinc oxide (ZnO)

I.2.1. Zinc oxide properties

I.2.1.1. Chemical properties

Zinc oxide (ZnO) is a highly versatile material, exhibiting exceptional chemical properties that enable its use across diverse applications, including gas sensing, catalysis, and environmental remediation. Its ability to function as a gas absorber and sensor for gases such as H_2S, CO_2, H_2, and CH_4 significantly enhanced by its nanostructured forms, such as nanorods and interconnected tetrapods. These structures improve sensitivity and response times, particularly at lower operating temperatures, making ZnO a preferred choice over traditional gas sensors [1,2]. ZnO also demonstrates remarkable photochemical catalytic capabilities when dispersed in liquids. It facilitates reactions such as the conversion of oxygen to ozone, ammonia to nitrate, and the reduction of methylene blue. This property has positioned ZnO as an essential component in photocatalytic processes [1]. Furthermore, thin films of ZnO have been employed to enhance copper deposition processes, showcasing their multifunctionality in advanced technological applications [2].However, challenges remain in optimizing the growth and characterization of high-quality ZnO, which is crucial for advancing its applications in electronics and environmental monitoring [3,4].

Despite these advantages, challenges persist in optimizing the growth and characterization of high-quality ZnO, which is essential for advancing its role in electronics, catalysis, and environmental monitoring. Recent research has focused on developing novel porous forms of ZnO using innovative methods such as ultrasonic excitation in acoustic cavitation reactors. This technique facilitates the interaction between NH_3 and $Zn(OH)_2$ under low-temperature conditions, leading to the synthesis of high-performance materials suitable for catalytic and sensing applications [5].

In summary, ZnO's unique chemical properties, coupled with its tunable nanostructures and adaptability, make it a promising candidate for future technological innovations in both industrial and environmental sectors.

I.2.1.2. Physical properties

Zinc oxide (ZnO) exhibits a wide range of physical properties that make it one of the most versatile semiconductors for technological applications. These properties influenced by factors such as doping, deposition methods, and substrate conditions.

ZnO thin films typically possess a polycrystalline hexagonal wurtzite structure, with crystallite sizes ranging from 13.30 nm to 26.7 nm depending on preparation techniques and dopants used. These films are commonly synthesized using methods such as chemical spray pyrolysis and sputtering, which allow for precise control over their structural properties [6,7,8].

Doping is a critical factor in tailoring ZnO's physical attributes. For instance, aluminum doping improves the mechanical properties, such as hardness and tensile strength, while also reducing electrical resistivity and enhancing optical transmittance to approximately 80% [9]. Similarly, boron doping has been shown to enhance the structural and optical characteristics of ZnO films, making them suitable for specialized applications [8,10].

Another significant property of ZnO is its energy band gap, typically around 3.28 eV. This band gap is crucial for applications in optoelectronics, particularly in photovoltaic devices. The ability to tune this property through doping and other modifications further enhances its utility in energy-related applications [10].

In summary, the physical properties of ZnO thin films are highly tunable, providing immense potential for applications in fields such as electronics, optics, and renewable energy. The interplay between structural parameters, doping, and synthesis techniques offers pathways to optimize ZnO films for specific technologic al needs.

I.2.1.3. Structural properties

Zinc oxide (ZnO) crystallizes in three primary structures: wurtzite, zinc blende, and rock salt. Among these, the wurtzite structure is the thermodynamically stable phase at ambient conditions, while the rock salt structure forms under high pressure, and the zinc blende structure can only be stabilized when grown on cubic substrates [11,12,13].

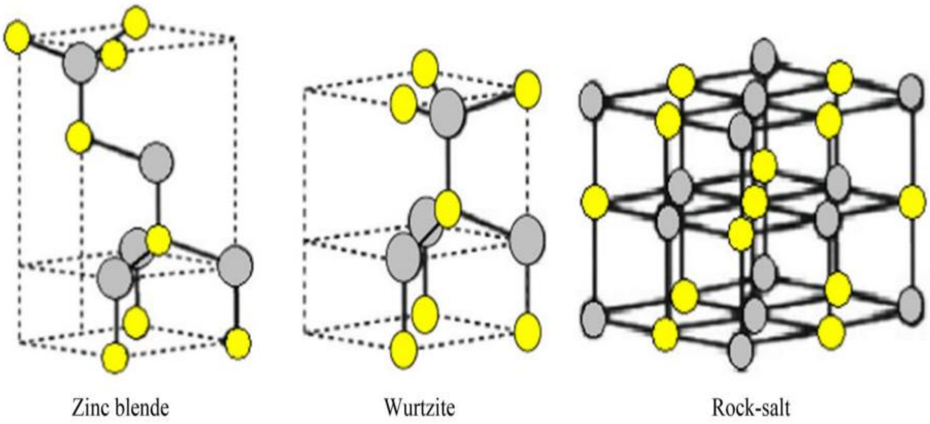

Figure I.1. Different forms of ZnO.

ZnO thin film generally crystallizes in the wurtzite (hexagonal) structure. This structure is a stack of compact double layers (Zn and O), along the [0001] axis, also known as c axis. In this wurtzite structure, the lattice parameters of ZnO are: a= 0.3249 nm, c= 0.5206 nm, it belongs to the symmetry group $P6_3mc$ [14], group number 186 in the Bravais classification [13]. Figure **I.2** shows the wurtzite structure of ZnO. In this figure, the cations and anions shown in two distinct tetrahedral forms. In one, there is a cation in the centre atom, whereas in the other, the anion encircled by four cations in the corners. With respect to the coordination forms, it symbolises a standard sp^3 covalent bond [15].

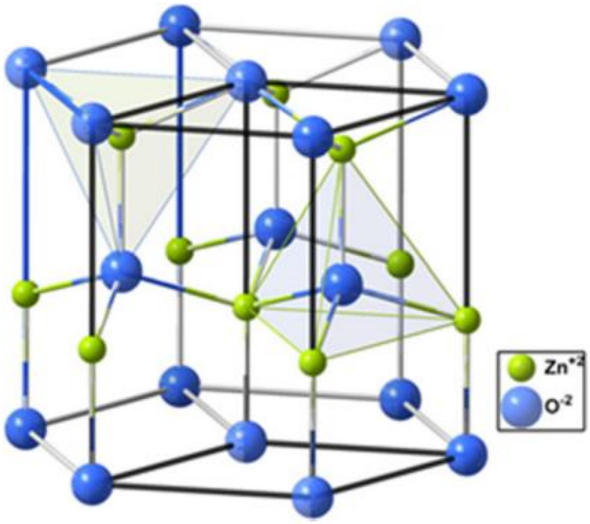

Figure I.2. Wurtzite structure of ZnO.

In the wurtzite structure, Zn and O atoms form a tetrahedral coordination, symbolizing a typical sp3 covalent bond. However, the Zn-O bond also exhibits a degree of ionic character due to the significant electro negativity of oxygen, which attracts zinc electrons. This ionic character influences the crystal's overall structural stability and its remarkable physical and chemical properties [15,16].

Under high pressure, the wurtzite phase transitions to the rock salt structure, demonstrating the material's polymorphic nature. This transformation occurs at pressures exceeding approximately 9 GPa, highlighting ZnO's adaptability to varying environmental conditions [17].

In summary, the structural properties of ZnO, particularly its wurtzite configuration, contribute significantly to its stability and functionality. These attributes are crucial for a wide range of applications, including electronics, optoelectronics, and catalysis.

I.2.1.4. Electronic band structure and optical properties

The electronic configurations of oxygen and zinc are as follows [18]:

Oxygen (O): $\mathbf{1s^2\ 2s^2\ 2p^4}$

Zinc (Zn): $\mathbf{1s^2\ 2s^2\ 2p^6\ 3s^2 3p^6\ 3d^{10}\ 4s^2}$

In the ZnO semiconductor, the valence band (VB) is primarily formed by the 2p orbitals of oxygen, while the conduction region is predominantly composed of the 4s orbitals of zinc.The enhanced conductivity observed in degenerate n-type semiconductors, particularly in pristine oxide layers, is primarily attributed to a high density of charge carriers, specifically electrons. This phenomenon influenced by structural irregularities and deviations from stoichiometry, which introduce anion vacancies and metal interstitials that act as donor-like states, enhancing electron conduction [19]. The mobility of these electrons, however, remains lower than the overall conductivity of the material, as indicated by the relationship between carrier density and mobility in degenerate electron gases [20]. Additionally, the presence of high electron densities can lead to significant effects on the material's electronic properties, such as band gap narrowing, which exacerbated by the random distribution of donor atoms [21]. Thus, while the abundance of charge carriers boosts conductivity, structural irregularities play a crucial role in determining the overall electronic behavior of these semiconductors [22].

Zinc oxide (ZnO) is a versatile transparent semiconductor with a refractive index of approximately 2, known for its exceptional absorption and scattering properties in the ultraviolet (UV) spectrum. When exposed to high-energy light ($E > 3.4$ eV) or electron bombardment, ZnO exhibits luminescence, emitting photons across various wavelengths, including near-ultraviolet ($\lambda = 350$ nm) and visible light, particularly green light around $\lambda = 550$ nm [3]. The synthesis of ZnO nanoparticles has demonstrated significant UV absorbance, achieving over 95% transmission in the UVA range (320-400 nm)[23]. Furthermore, ZnO nanomaterials are being explored for biomedical applications due to their biocompatibility and antibacterial properties, highlighting their potential in advanced technologies [24].The ability to tailor ZnO's properties through growth techniques and doping enhances its applicability in diverse fields, including optoelectronics and biomedicine, making it a material of great interest for future research and development [3].

I.2.1.5. Mechanical properties

Zinc oxide (ZnO) is a versatile semiconductor with unique properties that make it suitable for various applications, particularly in electronics and ceramics. Its modest hardness of 4.5 on the Mohs scale is complemented by advantageous characteristics such as high thermal conductivity, low thermal expansion, and a high melting point, which enhance its utility in ceramic applications [3,25]. ZnO exhibits the highest piezoelectric tensor among semiconductors with tetrahedral bonds, making it particularly valuable for piezoelectric applications requiring strong electromechanical coupling [3,26].

I.2.2. ZnO thin films

Zinc oxide (ZnO) thin films have garnered significant attention due to their outstanding properties and potential applications in diverse technological fields, including optoelectronics, gas sensors, and environmental remediation. These films are highly valued for their unique combination of optical, electrical, and photocatalytic characteristics, which can be further tuned by adjusting their structural and compositional properties [27,29].

ZnO thin films are typically synthesized using various deposition techniques such as chemical spray pyrolysis, sol-gel, spin coating sputtering, and atomic layer deposition. Each method offers advantages in tailoring film properties for specific applications. For instance, thin films produced via sputtering exhibit superior adhesion and uniformity, making the mideal for photovoltaic devices and sensors [30]. Similarly, spray pyrolysis has proven effective in creating films with controlled thickness and crystallinity, crucial for photocatalytic and optoelectronic applications [31].

I.2.3. Applications of ZnO in thin films

One of the key applications of ZnO thin films lies in photocatalysis. These films demonstrate high efficiency in degrading organic pollutants, such as dyes, under ultraviolet (UV) light. For instance, ZnO/TiO_2 heterostructured thin films have achieved over 80% degradation of methylene blue, highlighting their enhanced photocatalytic performance compared to single-component films [27]. Additionally, doping ZnO thin films with elements such as copper or strontium has further improved their photocatalytic activity, enabling effective degradation of pollutants like Rhodamine B and methyl orange [28,29].

The structural properties of ZnO thin films, such as their crystalline orientation and surface morphology, significantly influence their performance. These characteristics can be controlled by varying deposition parameters, such as substrate, temperature, precursor concentration, and annealing conditions. Advanced techniques like doping and the creation of ZnO-based heterostructures have also enabled enhanced light absorption, improved charge carrier separation, and greater overall efficiency in applications ranging from water purification to energy harvesting [32,33].

In summary, the adaptability and multi functionality of ZnO thin films make them an essential material in addressing critical environmental and technological challenges. Their tunable properties, combined with advancements in fabrication methods, position ZnO thin films as a cornerstone for innovative solutions in photocatalysis, energy, and sensor technology.

I.3. Strontium

I.3.1. Properties of strontium

I.3.1.1. Chemical properties

Sr, a member of the alkaline earth elements, holds an intermediary position between Ca and Ba in various chemical aspects. It is primarily present in nature as $SrSO_4$ (celestite), with occurrences of $SrCO_3$ (strontianite) in different regions across the globe. The element Sr derived its name from the Scottish village of Strontian, where its unique characteristics were initially identified by Crawford and Cruikshanks [34].

I.3.1.2. Physical properties

Strontium is classified as an element within group II of the periodic table of elements. With an atomic number of 38 and an atomic weight of 87.62 amu (atomic mass unit), it exhibits an outer electron shell configuration of $5s^2$, thereby placing it among the alkaline-earth metals (AEMs) group. Strontium typically displays an oxidation state of þ2, although þ1 is observed on rare occasions [35].

I.3.1.3. Structural Properties

Strontium exhibits a face-centered cubic (fcc) structure under standard conditions, with its lattice parameters significantly influenced by temperature and pressure. Understanding these structural properties is essential for various applications, particularly in materials science.

Strontium typically adopts an fcc structure, which is crucial for its stability and applications in ferroelectric materials like strontium bismuth niobate ($SrBi_2Nb_2O_9$)[36].

The structural properties of strontium oxide (SrO) also reveal phase transitions (**fig I.3**), notably from the rocksalt (B1) to cesium chloride (B2) structures under high pressure, with a transition pressure of approximately 38.5 GPa [37].

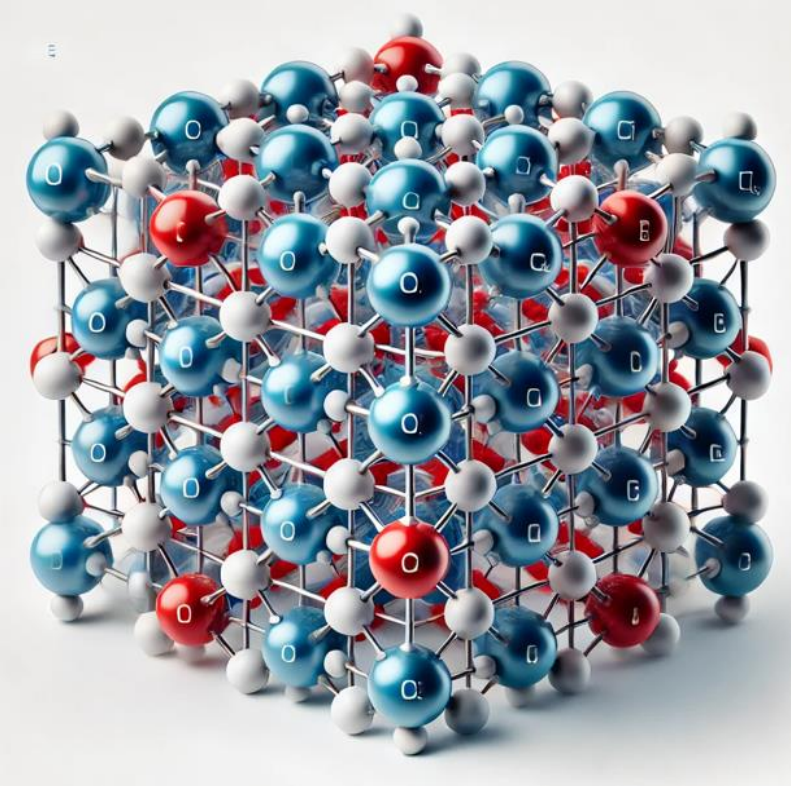

Figure I.3. The image of the crystal structure of SrO in the rock salt arrangement.

Precise lattice parameters are vital for predicting material behavior. In strontium titanate, for instance, the cubic to tetragonal phase transition occurs around 105 K (Kelvin), affecting its lattice dynamics [38].

The lattice parameters can vary with temperature, impacting the material's electronic and mechanical properties.

I.3.1.4. Electronic Properties

Strontium (Sr), with an electronic configuration of [Kr]5s², exhibits notable electronic properties that contribute to its metallic character. Its low ionization energy facilitates the easy removal of valence electrons, enhancing its conductivity. The following sections elaborate on these aspects.

Strontium's electronic configuration indicates two loosely held valence electrons in the 5s orbital, which is characteristic of alkaline earth metals. This configuration results in relatively low ionization energy, making it easier to ionize compared to other elements. The low ionization energy is a key factor in strontium's metallic character, allowing it to readily lose electrons and form positive ions [39].

Strontium is recognized for its excellent electrical conductivity, attributed to its loosely held valence electrons. This property is essential for applications in electronics and energy storage [40].

Studies on strontium compounds, such as strontium stannate, reveal that doping with alkali ions enhances conductivity by creating additional energy bands, which facilitate electron transport [41].

In contrast, while strontium exhibits strong metallic properties, its compounds can display semiconductor behavior under certain conditions, indicating a complex interplay between its elemental and compound forms [42].

I.3.1.5. Optical Properties

Strontium exhibits distinct optical properties that influence its absorption, refractive index, and luminescence. These characteristics are crucial for various applications, particularly in materials science and photonics. Strontium compounds, such as strontium manganite ($SrMnO_3$), demonstrate specific absorption bands in the electromagnetic spectrum; with optical gaps ranging from 1.3 to 1.5 eV depending on the treatment method [43].This absorption behavior is essential for applications in solar cells, where efficient light absorption is critical. The refractive index of strontium materials is a fundamental property that affects light bending. It often measured using spectroscopic techniques, which help in identifying and confirming the purity of strontium compounds [10]. This property is vital in optical applications, influencing how light interacts with materials. Certain strontium compounds exhibit luminescent properties, emitting light when excited by energy sources. This phenomenon linked to their electronic structure and explored through various spectroscopic methods [44] such luminescence can be harnessed in lighting and display technologies.

While strontium's optical properties are well-studied, the complexity of its interactions with light suggests that further research could uncover additional applications and enhance our understanding of its behavior in different environments.

I.3.1.6. Mechanical Properties

Strontium, a metal with unique mechanical properties, exhibits relatively low density, moderate hardness, and elastic behavior, making it suitable for various applications, particularly in biomedical fields. The following sections elaborate on these properties.

Strontium has a lower density compared to many metals, which contributes to its lightweight nature, beneficial in applications where weight reduction is critical [45].

The hardness of strontium classified as moderate, allowing it to be effectively utilized in alloying with biodegradable metals to enhance their mechanical properties [46].For instance, strontium-doped bioactive glasses showed significant increases in compressive strength, indicating improved hardness [47].

Strontium demonstrates elastic behavior, returning to its original shape after stress removal. This property is crucial in applications such as bone regeneration, where strontium-modified scaffolds have shown enhanced mechanical properties and elasticity [48].

While strontium's properties are advantageous, concerns regarding its systemic application in high doses for osteoporosis treatment highlight the need for careful consideration in its use [49].

I.3.2. Application of Strontium

Strontium is a chemical element exhibiting a wide range of applications. Its compounds find utility in the manufacturing of ceramics, glass, pyrotechnics, pigments, fluorescent lighting, and pharmaceuticals. Strontium exists in several isotopic forms, with strontium-90 being the most prevalent radioactive isotope [50].

Beyond its use in pyrotechnics and metallurgy, strontium serves as a coloring agent, a component in vacuum tubes, condensers, and optical glass. Its deoxidizing properties are beneficial in copper and bronze refining. Additionally, it enhances the castability of aluminum alloys. The radioactive isotope strontium-89 employed in cancer therapy as a radiation source. In agriculture, strontium compounds contribute to beet sugar production. Our research focused on utilizing strontium as a zinc activator within a photocatalytic process to eliminate dyes and pollutants from water bodies.

I.4. Thin Films

I.4.1. What is a thin film?

Thin films are extremely thin layers of material that are typically between a few nanometres and several micrometres thick and have different physical, chemical and mechanical properties due to their low dimensionality. These films are typically deposited onto substrates [51] employing methods such as spin coating, chemical vapor deposition

(CVD), and physical vapor deposition (PVD), or atomic layer deposition (ALD). The nanoscale thickness of thin films gives rise to distinct optical behaviors, such as interference and transparency, and enables their use in applications like anti-reflective coatings and optical filters. Additionally, thin films play a critical role in modern electronics, where they used to fabricate semiconductors, transistors, and other microelectronic components. Their ability to serve as protective barriers, conductive layers, or insulators makes them indispensable in energy technologies, including thin-film solar cells and advanced battery systems. The precise control of thin-film properties, such as composition, structure, and thickness, allows scientists to tailor their functionalities for specific applications, driving advancements in nanotechnology, renewable energy, and material science.

Thin films have emerged as a significant platform for photocatalytic applications due to their high surface-area-to-volume ratio, tunable optical properties, and controlled electronic structure. Photocatalytic thin films are typically composed of semiconducting materials such as titanium dioxide (TiO_2), zinc oxide (ZnO), or bismuth vanadate ($BiVO_4$), which can harness light energy to drive chemical reactions. These films are widely employed in environmental remediation, where they facilitate the degradation of organic pollutants in water and air under UV or visible light irradiation. Additionally, thin-film photocatalysts are instrumental in solar-driven water splitting to generate hydrogen, offering a sustainable route for clean energy production. The uniformity and precision in film thickness enable enhanced light absorption and charge carrier separation, improving photocatalytic efficiency. Furthermore, advancements in thin-film fabrication techniques, such as atomic layer deposition (ALD), chemical vapor deposition (CVD) and successive ionic layer adsorption and reaction (SILAR) allow for the creation of heterostructures and doped films that further optimize photocatalytic performance. These attributes make thin films a cornerstone in developing innovative solutions for energy and environmental challenges.

I.4.2. Thin film growth physics

Thin film growth is a complex physical process that involves the deposition of atoms, molecules, or ions onto a substrate to form a thin, continuous layer. The growth dynamics influenced by factors such as deposition method, substrate, temperature, deposition rate, and the nature of the substrate surface. Initially, the process begins with nucleation, where small clusters of atoms form on the substrate. This is followed by growth stages such as island growth (Volmer-Weber), layer-by-layer growth (Frank-van der Merwe), or a combination of both (Stranski-Krastanov) [52], which are illustrated in Figure **I.4**. These growth modes depend on the surface energy interactions between the film material and the substrate. Kinetic factors, such as surface diffusion, adsorption, desorption, and incorporation of atoms, play a critical role in determining the morphology and crystallinity of the thin film. Understanding the physics of thin film growth is essential for tailoring properties like thickness, uniformity, and structural phases to suit applications in electronics, optics, and energy devices.

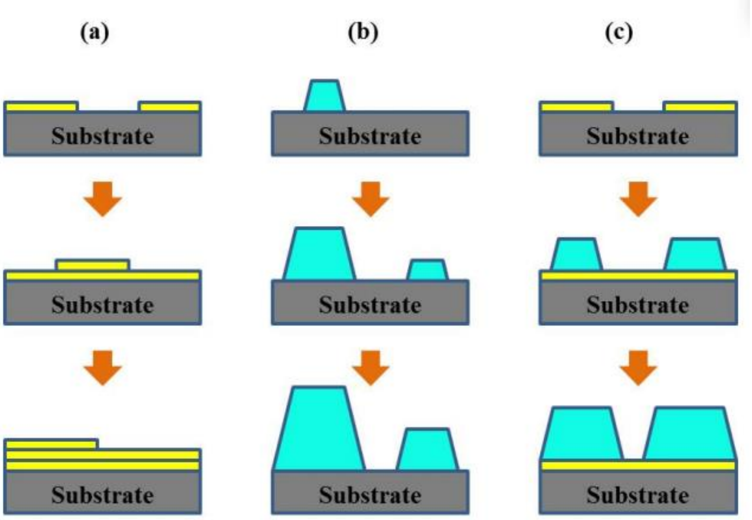

Figure I.4. Schematic diagram of growth mode: (a) layer-by-layer,(b) Island, (c) Stranski growth mode.

I.4.3. Thin film deposition technique

Various methods are available for thin film deposition, including physical techniques like physical vapor deposition (PVD), evaporation, and sputtering, as well as chemical approaches such as chemical vapor deposition (CVD), Sol gel, spray pyrolysis, and SILAR. The classification of these methods shown in figure **I.5**:

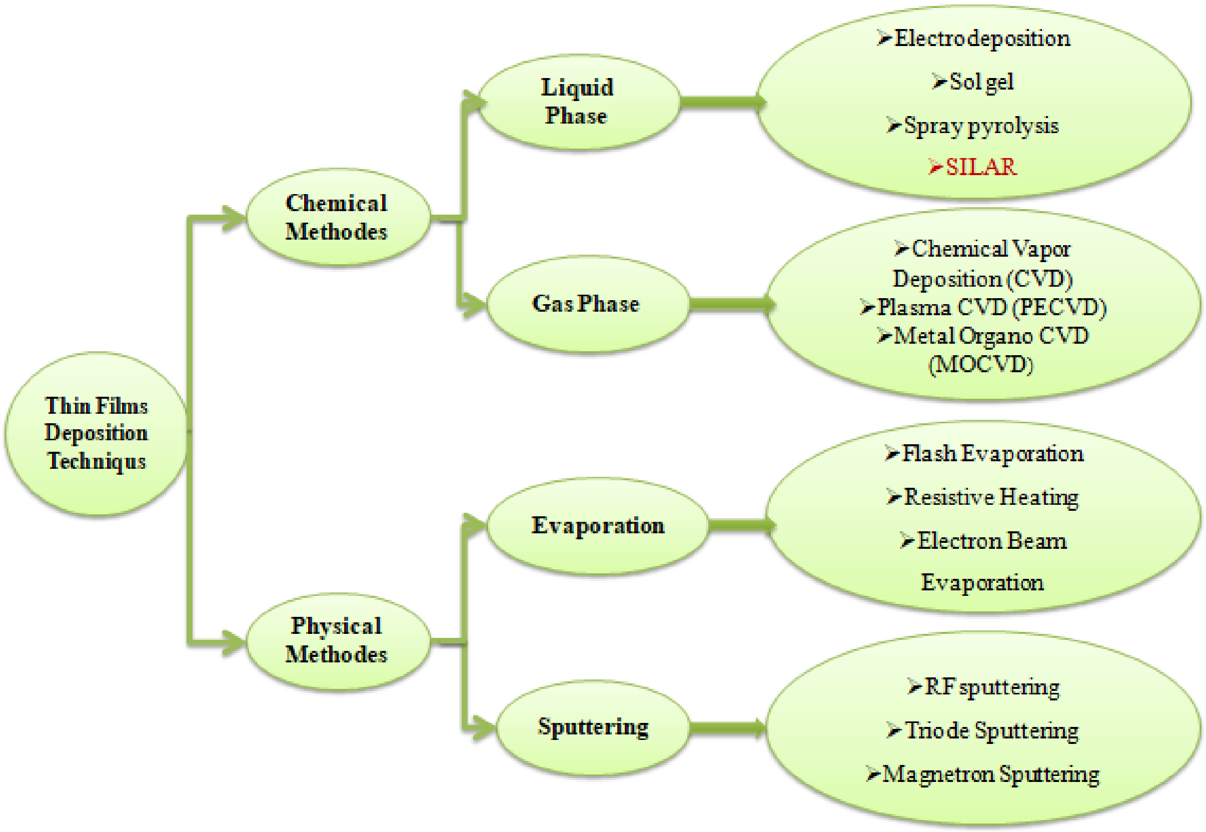

Figure I.5. Classification of thin film deposition techniques.

The figure **I.5** of thin film deposition techniques, as presented in the diagram, elegantly organizes the diverse approaches into two primary categories: chemical and physical methods. This structured layout reflects the thoughtful progression of technological advancements in materials science. Chemical methods, rooted in liquid and gas-phase reactions, highlight the ingenuity of utilizing solutions or gaseous precursors to achieve precise film growth. Techniques like SILAR, electrochemical deposition, and sol-gel processes display the power of chemistry in constructing thin films with remarkable control over their properties. On the other hand, physical methods emphasize direct manipulation of materials through evaporation or sputtering, where energy sources like electron beams or RF sputtering systems transform solid precursors into meticulously deposited films. The scheme itself is a testament to the interdisciplinary nature of thin-film science, bridging chemistry, physics, and engineering.

I.4.4. Applications of thin films

Thin films, which defined as ultra-thin layers of various materials, offer a wide range of applications due to their special properties. In optics, these films used to improve both light transmission and reflection in devices such as anti-reflective coatings and mirrors. In the field of electronics, they form the basic components of transistors, semiconductors and insulators. In the field of magnetic, thin films facilitate data storage and sensor technology. In mechanics, they provide protective functions, increased hardness and lubrication. In the energy sector, they are indispensable for the functionality of solar cells, batteries and fuel cells. Other applications include decorative coatings, biomedical devices, sensors and optical data storage systems. His inherent versatility, precision and cost-effectiveness make thin films an invaluable asset for today's technological advancement. In addition, thin films are of great importance for photocatalysis, a process in which light energy used to catalyze chemical reactions.

The photocatalysis of thin films to enhance photocatalytic reactions, particularly for environmental remediation and energy applications. These films, often composed of semiconductors, facilitate the generation of reactive species under light irradiation, which can degrade organic pollutants or produce hydrogen from water. The performance of thin films in photocatalysis is influenced by various factors, including film thickness, surface morphology, and crystallinity. A notable example of thin film photocatalysis involves zinc oxide (ZnO), a wide-bandgap semiconductor known for its strong photocatalytic properties. ZnO thin films can be fabricated using techniques such as DC sputtering followed by thermal oxidation. Studies have shown that ZnO films oxidized at lower temperatures (e.g., 300°C) exhibit superior photocatalytic activity compared to those oxidized at higher temperatures (e.g., 600°C and 900°C). This enhanced activity attributed to better optical quality and reduced defects in the films, which facilitate efficient electron-hole pair generation under UV light, making ZnO thin films effective for applications like the degradation of organic dyes in wastewater treatment.

I.5. Photocatalysis

The photocatalytic process involves the excitation of a semiconductor material, such as titanium dioxide (TiO_2) or zinc oxide (ZnO), when exposed to light of sufficient energy. Upon absorption of photons, electron-hole pairs are generated, initiating redox reactions that degrade pollutants. These reactions result in the breakdown of complex organic molecules into simpler, environmentally benign components like carbon dioxide and water.

Key advantages of photocatalysis include its reliance on renewable light energy, its versatility in treating diverse pollutants, and it’s potential for application in air and water purification systems. Moreover, the process operates at ambient conditions, making it energy-efficient and eco-friendly. Despite its promise, challenges such as limited light absorption, electron-hole recombination, and the need for effective photocatalyst materials remain areas of active research.

This study focuses on the application of photocatalysis for pollutant elimination, highlighting its principles, mechanisms, and potential to address the growing demand for clean water and a healthier environment.

I.5.1. Photocatalysis mechanisms

The basic concepts of photocatalysis explain the essential mechanisms by which light-induced catalytic reactions occur, primarily using semiconductors as photocatalytic agents. This phenomenon utilises photon energy to promote chemical changes. The following is a comprehensive treatise on the key principles:

1) Light Absorption

Photocatalysts, typically semiconductors, absorb photons of light whose energy matches or exceeds the material's bandgap energy (Eg).

This absorption promotes an electron (e^-) from the valence band (VB) to the conduction band (CB), creating a positively charged hole (h^+) in the VB:

$$Photocatalyst + h\nu \rightarrow e^-_{CB} + h^+_{VB} \qquad (01)$$

2) Charge carrier separation and migration

The photoexcited electron-hole pairs must be separated and transported to the surface of the photocatalyst. Efficient separation is essential to minimize recombination, which can otherwise release the absorbed energy as heat or light.

3) Surface redox reactions

The separated charges drive chemical reactions on the photocatalyst's surface:

Oxidation by holes (h^+):

Holes oxidize substances like water (H_2O) or hydroxide ions (OH^-) to generate reactive oxygen species (ROS), such as hydroxyl radicals ($OH\cdot$):

$$h^+ + H_2O \rightarrow OH^\cdot + H^+ \qquad (02)$$

Reduction by electrons (e–):

Electrons reduce oxygen molecules adsorbed on the surface, forming superoxide anions (O^{2-}):

$$e^- + O_2 \rightarrow O_2^- \qquad (03)$$

4) Reaction with Target Molecules

The reactive species ($\cdot OH$, O_2^-, etc.) and direct red-ox reactions degrade or convert target molecules. Pollutants, organic compounds, or other substances are broken down into simpler, less harmful products like carbon dioxide (CO_2) and water (H_2O).

5) Recombination of Charge Carriers (Undesirable Process)

Electrons and holes can recombine without participating in reactions, releasing energy as heat or light:

$$\mathrm{e}^-(CB) + h^+(VB) \rightarrow heat/light \qquad (04)$$

This reduces the overall efficiency of the photocatalytic process.

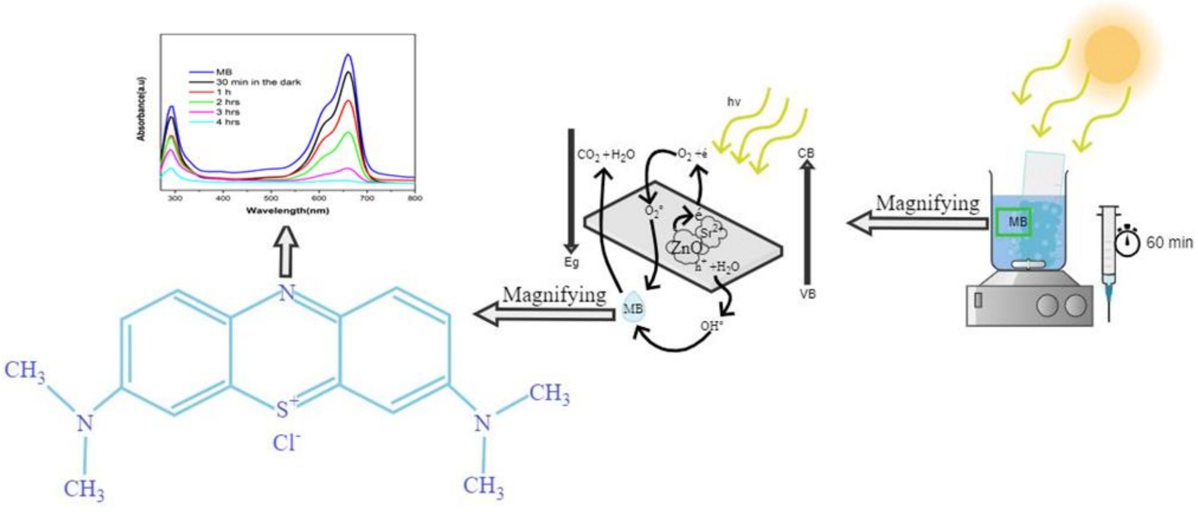

Figure I.6. Schematic representation of the photocatalytic degradation of methylene blue through a semiconductor.

The figure **I.6** on the top indicates the absorbance spectra of MB over time, highlighting the changes in absorbance as the reaction progresses—showing a decrease in absorbance at around 660 nm corresponding to the MB peak, indicating degradation. In the central diagram, the photocatalytic process is shown where UV light (hv) activates the ZnO, generating electron-hole pairs (e^- and h^+). These charge carriers facilitate the formation of reactive oxygen species, such as hydroxyl radicals (•OH) and superoxide anions ($O_2^{\bullet -}$), which react with MB molecules, ultimately leading to their degradation. The right part of the image depicts the magnifying setup used to enhance the light intensity for the reaction to achieve greater efficiency, suggesting that under optimal conditions (such as exposure to sunlight for 60 minutes), the photocatalytic process can significantly reduce the concentration of MB in solution, demonstrating the potential of photocatalysis in wastewater treatment applications.

I.5.2. Factors Influencing Photocatalysis

I.5.2.1. Bandgap energy (E_g)

The band gap energy of a photocatalyst is a fundamental parameter that dictates its ability to absorb light and drive chemical reactions. An ideal band gap allows the absorption of photons with adequate energy to excite electrons from the valence band to the conduction band, generating electron-hole pairs critical for photocatalytic processes. Recent studies have focused on engineering the band gap to enhance photocatalytic efficiency under visible light irradiation. For instance, doping titanium dioxide (TiO_2) with bismuth has been shown to significantly reduce its band gap, thereby extending its light absorption into the visible spectrum and improving its photocatalytic performance [53]. A finely tuned band gap is critical for balancing light absorption and preventing rapid recombination of electron-hole pairs. Advances in doping, heterojunctions, and nanostructuring have further demonstrated how band gap engineering can enhance photocatalytic performance, as reviewed comprehensively by Zhang et al [54]. Thus, the interplay of band gap energy and photocatalytic activity underscores the importance of materials science in addressing global challenges such as water purification, hydrogen production, and CO_2 reduction.

I.5.2.2. Photocatalyst properties

The enhancement of photocatalytic activity is intricately linked to factors such as high surface area, crystalline structure, and doping. A high surface area provides more active sites for photocatalytic reactions, facilitating greater interaction between the catalyst and reactants. For instance, mesoporous structures with increased surface areas have been shown to improve photocatalytic performance [55].

The crystalline structure of a photocatalyst significantly influences its efficiency. For instance, studies have shown that the (001) of ZnO facets exhibit higher catalytic activity due to their higher surface energy and increased availability of active sites. Additionally, the presence of oxygen vacancies and other intrinsic defects within the crystal lattice can introduce localized energy states, extending light absorption into the visible spectrum and further enhancing photocatalytic efficiency. Therefore, tailoring the crystalline structure of ZnO, including controlled exposure of specific facets and defect engineering, presents a promising strategy for optimizing its performance in photocatalytic applications [56].

Doping introduces foreign atoms into the photocatalyst's lattice, modifying its electronic structure and enhancing light absorption. For example, doping zinc oxide (ZnO) with strontium (Sr) introduces significant modifications to its electronic structure, thereby enhancing its photocatalytic performance. The incorporation of Sr^{2+} ions into the ZnO lattice alters the band gap energy, facilitating improved light absorption and charge carrier dynamics. Recent studies have demonstrated that Sr-doped ZnO exhibits superior photocatalytic activity compared to undoped ZnO. For instance, Sr-doped ZnO nanoparticles have shown enhanced degradation efficiency of organic pollutants under sunlight irradiation, achieving up to 99% degradation of methylene blue, 90% of Rhodamine B, and 93% of methyl orange, attributed to the modified electronic properties and increased surface area provided by Sr doping [57].

Additionally, Sr-doped ZnO thin films prepared by the SILAR method have demonstrated remarkable photocatalytic performance, achieving 94.82% degradation of methylene blue under sunlight, indicating the potential of Sr doping in enhancing the photocatalytic efficiency of ZnO-based materials [58].

These findings underscore the effectiveness of Sr doping in tuning the electronic and structural properties of ZnO, making it a promising strategy for developing efficient photocatalysts for environmental remediation applications. We will clarify this in the further course of this dissertation.

I.5.2.3. Light intensity

Light intensity is a critical factor influencing the efficiency of photocatalytic processes. At low light intensities, the rate of photocatalytic degradation is directly proportional to the light intensity, following first-order kinetics. However, as light intensity increases, this relationship can deviate due to factors such as the recombination of charge carriers. Excessive light intensities may lead to increased recombination rates, resulting in diminished photocatalytic efficiency [59]. Therefore, optimizing light intensity is essential to maximize photocatalytic performance, ensuring sufficient photon flux to generate charge carriers while minimizing recombination losses [60]. This balance is crucial for the effective design and implementation of photocatalytic systems in environmental and energy-related applications [61].

I.5.2.4. Reaction environment

The efficiency of photocatalytic processes is profoundly influenced by environmental factors such as oxygen levels, water presence, and pH.

Oxygen serves as a crucial electron acceptor in photocatalysis; its presence can significantly enhance the degradation rates of pollutants. For example, research has demonstrated that the presence of oxygen shortens the illumination time required for the complete degradation of certain contaminants, thereby enhancing the speed of the photocatalytic process [62].

Water, as a solvent and reactant, plays a vital role in photocatalytic reactions. The presence of water can influence the generation of reactive oxygen species (ROS), which are crucial for the decomposition of organic pollutants. In addition, the interaction between aqueous molecules and the surface of the photocatalyst can influence the adsorption of pollutants and the overall effectiveness of the photocatalytic mechanism [63].

The pH of a solution plays a crucial role in photocatalytic processes [64]. This is because pH influences several key factors that impact the efficiency of these reactions [65]. Firstly, it affects the surface charge of the photocatalyst, which can significantly impact the adsorption of pollutants onto its surface [66]. Secondly, pH can alter the speciation of the pollutant itself, changing its reactivity towards the generated reactive oxygen species (ROS) like hydroxyl radicals[67].For example, some pollutants may exist in different forms at different pH values, with some forms being more susceptible to degradation than others. Finally, pH can influence the generation and stability of these ROS, which are essential for the degradation process. Studies have shown that optimal pH values often exist for specific photocatalytic systems, where the interplay of these factors leads to the highest degradation rates [68].

I.5.3. Applications of Photocatalysis

Photocatalysis stands at the forefront of sustainable technology, offering versatile solutions across multiple domains. Photocatalysts effectively degrade organic pollutants in water and air, transforming harmful substances into benign end products. They also facilitate the removal of heavy metals and hazardous chemicals, contributing to cleaner ecosystems [69]. In the quest for renewable energy, photocatalytic water splitting has emerged as a promising method to produce hydrogen fuel, a clean energy carrier. Additionally, solar-driven photocatalytic conversion of CO_2 into fuels or valuable chemicals offers a pathway to mitigate greenhouse gas emissions while generating useful products. Photocatalytic materials are employed to create antimicrobial surfaces capable of killing bacteria and viruses, enhancing hygiene in medical facilities and public spaces [70]. Photocatalysis provides green pathways for producing valuable chemical compounds, reducing the need for harsh reagents and energy-intensive processes, thereby aligning with principles of sustainable chemistry [68].

I.6. Degradation of Methylene Blue (MB)

Methylene Blue is a common dye used in textiles, pharmaceuticals, and biology, and its release into water is a significant environmental concern due to its toxicity and persistence. Photocatalysis effectively degrades MB into non-toxic products:

Upon UV or visible light irradiation, MB adsorbed on the photocatalyst undergoes complete mineralization, resulting in$CO_2$and water.

Methylene blue, a widely used organic dye, poses environmental concerns due to its toxicity and recalcitrance to biodegradation. Photocatalysis, a promising technology for environmental remediation, can effectively degrade methylene blue. Semiconductor-based photocatalysts, such as titanium dioxide (TiO_2)[69]and zinc oxide (ZnO) [70], can absorb light energy and generate highly reactive species, like hydroxyl radicals. These radicals can oxidize the complex structure of methylene blue, breaking it down into simpler, less harmful compounds. By optimizing the properties of the photocatalyst, including its bandgap, surface area, and crystallinity, the efficiency of methylene blue degradation can be significantly improved.

I.7. Conclusion

This chapter has provided a comprehensive foundation for understanding the key materials at the heart of this study. The versatile properties and wide-ranging applications of zinc oxide (ZnO) have been thoroughly examined, underscoring its critical role in technological advancements across various fields, including electronics, optoelectronics, and environmental remediation. Additionally, the fundamental properties of strontium (Sr), including its crystallographic structure, optical behavior, and morphological characteristics, have been explored in detail.

Particular attention was given to the synergistic effects of strontium doping on ZnO, with an emphasis on how Sr concentration influences the structural, optical, and catalytic properties of ZnO. This combination offers exciting potential for innovative applications, particularly in the realm of photocatalytic water purification, where Sr-doped ZnO can address critical environmental challenges.

The insights gained from this chapter not only establish the theoretical framework but also serve as a foundation for the experimental studies and practical applications presented in the subsequent chapters. By bridging fundamental material science with applied research, this work aims to advance the development of efficient and sustainable solutions for environmental and technological needs.

References of chapter I

[1] Zhang, Qiuping, et al. "Zinc oxide nanorods for light-activated gas sensing and photocatalytic applications." *ACS Applied Nano Materials* 6.19 (2023): 17445-17456.

[2] Knoepfel, Abbey, Bed Poudel, and Sanju Gupta. "Surface-Catalyzed Zinc Oxide Nanorods and Interconnected Tetrapods as Efficient Methane Gas Sensing Platforms." *Chemosensors* 11.9 (2023): 506.

[3] Saravade, Vishal, et al. "Advances in growth, doping, and devices and applications of zinc oxide." *Journal of Vacuum Science &Technology*A 42.2 (2024).

[4] Al-darwesh, Mouhaned Y., et al. "Synthesis and characterizations of zinc oxide nanoparticles and its ability to detect O2 and NH3 gases." *Results in Chemistry* 6 (2023): 101064.

[5] Liao, Xilin, et al. "Construction of BiOI/TiO2 flexible and hierarchical S-scheme heterojunction nanofibers membranes for visible-light-driven photocatalytic pollutants degradation." *Science of the Total Environment* 806 (2022): 150698.

[6] López-Suárez, Alejandra, and Dwight R. Acosta. "The Influence of Different Solvents on the Physical Properties of ZnO Thin Films." *Journal of Composites Science* 8.8 (2024): 332.

[7] Hmoud, Hamsa Abdul Kareem. "The Effect of Aluminum Dopant on some physical Properties of Zinc Oxide Thin Films Via Chemical Spray Pyrolysis." *Journal of the College of Basic Education* 30.123 (2024): 1-13.

[8] Merdan, M., and Hikmat A. Banimuslem. "Synthesis, characterization and LDA+ U calculations of zinc oxide nanoparticles." *Physica Scripta* 99.6 (2024): 065942.

[9] Kumar, Arun, Ashaq Hussain Sofi, and M. A. Shah. "Augmented Structural and Optical Features of CuO-and Al-Doped CuO Nanostructures." *Iranian Journal of Science* 47.5 (2023): 1883-1891.

[10] Álvarez-Vázquez, J. I., et al. "Physical properties of aluminum doped Zinc Oxide thin films and single wall carbon nanotubes bilayers with potential application in photovoltaics devices." *Engineering Research Express* 5.3 (2023): 035034.

[11] Espitia, Paula Judith Perez, et al. "Zinc oxide nanoparticles: synthesis, antimicrobial activity and food packaging applications." *Food and bioprocess technology* 5 (2012): 1447-1464.

[12] Rahman, Ashmalina, et al. "Zinc oxide and zinc oxide-based nanostructures: biogenic and phytogenic synthesis, properties and applications." *Bioprocess and Biosystems Engineering* 44.7 (2021): 1333-1372.

[13] S Rahmane. Elaboration et caracterisation de couches minces par spray pyrolyse et pulverisation magnetron. PhD thesis. *University of Mohamad Khider-Biskra*. 2008.

[14] N Kouidri. Contribution à l'étude de couches minces d'oxydes transparents conducteurs à base de zinc et cobalt par spray pneumatique. PhD thesis. *University of Mohamad Khider-*Biskra. 2019.

[15] Bhuiyan, Mohammad Ruhul Amin, and Hayati Mamur. "A Brief Review on the Synthesis of Zno Nanoparticles for Biomedical Applications." *Iranian Journal of Materials Science & Engineering* 18.3 (2021).

[16] BOUABDALLAH Abdelghani. Caractérisation structurale et optique De nanocristaux de ZnO, PhD thesis. *University of Constantine1*. 2013.

[17] Vegard Skiftestad Olsen. Synthesis and Characterization of Homoepitaxial ZnO Thin Films, Master's Thesis. universityof OSLO; 2016.

[18] H Slimi. Élaboration et caractérisation de couches minces co-dopées In, Co, préparées par la pulvérisation cathodique, applications aux cellules photovoltaïques. PhD thesis. *University of Littoral Côte Opale, University of Sfax*. 2019

[19] Rajshekar, Kadiyam, and D. Kannadassan. "A comprehensive density-of-states model for oxide semiconductor thin film transistors." *Journal of Computational Electronics* 20 (2021): 2331-2341.

[20] Palenskis, Vilius. "The effective density of randomly moving electrons and related characteristics of materials with degenerate electron gas*." AIP Advances* 4.4 (2014).

[21] Lowney, Jeremiah R., and Jon C. Geist. "Comparison of models of the built-in electric field in silicon at high donor densities*." Journal of applied physics* 55.10 (1984): 3624-3627.

[22] Thuselt, F., and K. Unger. "High Carrier Densities and Gap Shrinkage in p–i–n-Type Structures." *physica status solidi* (a) 84.2 (1984): 677-691.

[23] Turtogtokh, Enkhtuya, and Galya Tsermaa. "Sol-Gel Synthesis and Optical Characterization of Zno Nanoparticles." *Materials Science Forum*. Vol. 1083. Trans Tech Publications Ltd, 2023.

[24] Ruhul Amin Bhuiyan, Mohammad, HayatiMamur, and Ömer Faruk Dilmaç. "Zinc Oxide Nanomaterials for Biomedical Applications." *Advances in Organic Synthesis*: Volume 18. Bentham Science Publishers, 2023. 190-235.

[25] Hegde, Vinayakprasanna N. "Study on structural, morphological, elastic and electrical properties of ZnO nanoparticles for electronic device applications." *Journal of Science: Advanced Materials and Devices* 9.3 (2024): 100733.

[26] Ghahfarokhi, MojdehRahnama, et al. "Nano ZnO: Structure, Synthesis Routes, and Properties." *ZnOand Their Hybrid Nano-Structures: Potential Candidates for Diverse Applications* 146 (2023): 1-34.

[27] Park, Ji Young, Jeong Hwan Han, and Byung Joon Choi. "High-performance of ZnO/TiO2 heterostructured thin-film photocatalyst fabricated via atomic layer deposition." *Journal of Vacuum Science & Technology* A 42.3 (2024).

[28] Shobana, T., R. Sakthi Sudar Saravanan, and D. Kathirvel. "Effect of Copper Inclusion in Zinc sulfide Thin Films for Photocatalytic Applications." *J. Environ. Nanotechnol* 13.1 (2024): 234-242.

[29] Thamer, A., and S. Mohamed. "Characterization of undoped and doped CdS nano-thin films by ZnO for photocatalytic application." *Chalcogenide Letters* 20.12 (2023).

[30] Rodríguez, Iván R., et al. "Sputtering Deposition of ZnO Thin Films for Photocatalytic Hydrogen Production: Perspectives on Upscaling." *Nanofabrication* 9 (2024).

[31] Krysova, H., et al. "High-quality dense ZnO thin films: work function and photo/electrochemical properties." *Journal of Solid State Electrochemistry* (2024): 1-16.

[32] Tran, Manh Hoang, Thi My Huyen Nguyen, and Chung Wung Bark. "Toward Industrial Production of a High-Performance Self-Powered Ultraviolet Photodetector Using Nanoporous Al-Doped ZnO Thin Films." *ACS omega* 8.38 (2023): 35343-35350.

[33] Pirposhte, Minoo Alizadeh, et al. "ZnO Thin Films: Fabrication Routes, and Applications." *ZnO and Their Hybrid Nano-Structures: Potential Candidates for Diverse Applications* 146 (2023): 263-293.

[34] Inoue S. Chemistry of Strontium. In: Handbook of Stable Strontium. Plenum PRE. *Quebec, Canada*; 1981. p. 11–8.

[35] Gasik MI. Technology of Ferroalloys with Alkaline-Earth Metals. In: Handbook of Ferroalloys: Theory and Technology .*Twelfth Ed. Ukraine: Elsevier*; 2013. p. 471–94.

[36] Mojumdar, Pooja, RitushreeShaily, and Renuka Bokolia. "Structural properties of strontium bismuth niobate (SrBi2Nb2O9) ferroelectric ceramics." *Materials Today: Proceedings* 47 (2021): 4661-4665.

[37] Karil, Poornima, et al. "Effect of pressure on structural and elastic properties of strontium oxide." *AIP Conference Proceedings*. Vol. 2369. No. 1. AIP Publishing, 2021.

[38] Smith, Alastair George Hartley. Structural and defect properties of strontium titanate. Diss. *UCL (University College London)*, 2012.

[39] Aymar, Mireille, and Olivier Dulieu. "The electronic structure of the alkaline-earth-atom (Ca, Sr, Ba) hydride molecular ions." *Journal of Physics B: Atomic, Molecular and Optical Physics* 45.21 (2012): 215103.

[40] Rouviller, Axel, et al. "Structural, Electrical, and Optical Properties of Strontium–Vanadate Films Grown by Magnetron Sputtering." *ACS Applied Electronic Materials* 6.2 (2024): 1318-1329.

[41] Zulueta, Yohandys A., Minh Tho Nguyen, and My-Phuong Pham-Ho. "Strontium stannate as an alternative anode for Na-and K-Ion batteries: A theoretical study." *Journal of Physics and Chemistry of Solids* 162 (2022): 110505.

[42] Žužić, Andreja, et al. "The optical properties of strontium manganite thin films prepared by novel phototreatment technique." *Journal of alloys and compounds* 951 (2023): 169972.

[43] Marrucho, Isabel M. "OPTICAL AND SPECTROSCOPIC PROPERTIES." *Poly (Lactic Acid) Synthesis, Structures, Properties, Processing, Applications, and End of Life* (2022): 115-133.

[44] Li, Huafang, and Luqing Ma. "A comprehensive review on the role of strontium in biodegradable metals." *Journal of Materials Chemistry B* (2024).

[45] Battal, W., et al. "Strontium doping effect on characteristics of ultrasonically sprayed zinc oxide thin films." *Applied Physics A* 126 (2020): 1-10.

[46] Amudha, S., et al. "Enhanced mechanical and biocompatible properties of strontium ions doped mesoporous bioactive glass." *Composites Part B: Engineering* 196 (2020): 108099.

[47] Quade, Mandy, et al. "Strontium enhances BMP-2 mediated bone regeneration in a femoral murine bone defect model." *Journal of Biomedical Materials Research Part B: Applied Biomaterials* 108.1 (2020): 174-182.

[48] Ter-Zakaryan, A., and A. D. Zhukov. "Materials Horizons: From Nature to Nanomaterials." *Materials Horizons: From Nature to Nanomaterials.* 2021. 349-377.

[49] Wang, Ying, et al. "Ultrathin ferroelectric films: growth, characterization, physics and applications." *Materials* 7.9 (2014): 6377-6485.

[50] Sabino, Fernando P., and Anderson Janotti. "Dramatic enhancement of visible-light absorption in TiO2 by adding Bi." *ArXiv preprint arXiv*:2302.02461 (2023).

[51] Nemiwal, Meena, Tian C. Zhang, and Dinesh Kumar. "Recent progress in g-C3N4, TiO2 and ZnO based photocatalysts for dye degradation: Strategies to improve photocatalytic activity." *Science of the total environment* 767 (2021): 144896.

[52] Mazinani, Babak, et al. "Photocatalytic activity, surface area and phase modification of mesoporous SiO2–TiO2 prepared by a one-step hydrothermal procedure." *Ceramics International* 40.8 (2014): 11525-11532.

[53] Debroye, Elke, et al. "Facet-dependent photoreduction on single ZnO crystals." The journal of physical chemistry letters 8.2 (2017): 340-346.

[54] Selvaraj, Saravanan, et al. "Effect of Sr doping in ZnO microspheres for solar light-driven photodegradation of organic pollutants." *Journal of Materials Science: Materials in Electronics* (2022): 1-12.

[55] Mokrani, Nourelhouda, et al. "Boosting photocatalytic stability: hydrophilic Sr-doped ZnO thin films prepared via the SILAR method for enhanced performance over multiple cycles." *Physica Scripta* 99.9 (2024): 0959a4.

[56] Hussein, Falah Hassan. "Photochemical treatments of textile industries wastewater." *Advances in Treating Textile Effluent* (2011): 117-144.

[57] Zhu, Zhonghui, et al. "What Role Does the Incident Light Intensity Play in Photocatalytic Conversion of CO2: Attenuation or Intensification?." *ChemPhysChem* 23.14 (2022): e202100851.

[58] Enesca, Alexandru, and Luminita Isac. "The influence of light irradiation on the photocatalytic degradation of organic pollutants." *Materials* 13.11 (2020): 2494.

[59] Tseng, Dyi-Hwa, Lain-ChuenJuang, and Hsin-Hsu Huang. "Effect of oxygen and hydrogen peroxide on the photocatalytic degradation of monochlorobenzene in TiO2 aqueous suspension." *International Journal of Photoenergy* 2012.1 (2012): 328526.

[60] Guernelli, Moreno, et al. "pH Switchable Water Dispersed Photocatalytic Nanoparticles." *Chemistry–A European Journal* 28.34 (2022): e202200118.

[61] Sapińska, Dominika, et al. "Influence of pH on the kinetics and products of photocatalytic degradation of sulfonamides in aqueous solutions." *Toxics* 10.11 (2022): 655.

[62] Gusain, Rashi, Neeraj Kumar, and Suprakas Sinha Ray. "Factors influencing the photocatalytic activity of photocatalysts in wastewater treatment." *Photocatalysts in advanced oxidation processes for wastewater treatment* (2020): 229-270.

[63] Wang, Wen-Yu, and Young Ku. "Effect of solution pH on the adsorption and photocatalytic reaction behaviors of dyes using TiO2 and Nafion-coated TiO2." *Colloids and Surfaces A: Physicochemical and Engineering Aspects* 302.1-3 (2007): 261-268.

[64] Alkaim, A. F., et al. "Enhancing the photocatalytic activity of TiO 2 by pH control: a case study for the degradation of EDTA." *Catalysis Science & Technology* 3.12 (2013): 3216-3222.

[65] Sujatha, Gurudev, Subramaniam Shanthakumar, and FulviaChiampo. "UV light-irradiated photocatalytic degradation of coffee processing wastewater using TiO2 as a catalyst." *Environments* 7.6 (2020): 47.

[66] Garg, Seema, and Amrish Chandra. Photocatalysis for Environmental Remediation and Energy Production.Book, *Springer: Berlin, Germany*, 2023.

[67] Hassaan, Mohamed A., et al. "Principles of photocatalysts and their different applications: a review." *Topics in Current Chemistry* 381.6 (2023): 31.

[68] Coronado, Juan M., et al., eds. Design of advanced photocatalytic materials for energy and environmental applications.Book, Vol. 71. *London: Springer*, 2013.

[69] Jay, Lindelwa, Evans Chirwa, and Shepherd Masimba Tichapondwa. "The effect of dissolved oxygen on the UV/TiO2 photocatalytic degradation mechanism of phenol."*CHEMICAL ENGINEERING TRANSACTIONS76*(2019).

[70] Qi, Kezhen, et al. "Review on the improvement of the photocatalytic and antibacterial activities of ZnO." *Journal of Alloys and Compounds* 727 (2017): 792-820.

Chapter II:

Development and Characterization of Pure ZnO and ZnO/Sr Thin Films by SILAR Method

II.1. Introduction

The development of thin films with tailored properties has become a significant area of research due to their extensive applications in optoelectronics, photocatalysis, and environmental remediation. This chapter focuses on the synthesis and characterization of pure zinc oxide and Sr-doped ZnO thin films deposited on glass substrates using the Successive Ionic Layer Adsorption and Reaction (SILAR) method. Building upon the state-of-the-art advancements in the field, the originality of this work lies in examining the effect of strontium concentration and the role of various additives on the structural, morphological, and optical properties of ZnO thin films.

To achieve this, we present a detailed account of the experimental procedures, including the preparation of substrates and solutions, the deposition process via SILAR, and the parameters optimized to enhance film quality. Furthermore, the chapter discusses advanced characterization techniques, such as X-ray diffraction (XRD), scanning electron microscopy (SEM), atomic force microscopy (AFM), and UV-Vis spectroscopy, employed to evaluate the thin films. Special emphasis is placed on the photocatalytic performance of these films, particularly their potential in degrading organic pollutants and their wettability properties analyzed through water contact angle measurements. This chapter establishes the groundwork for understanding the innovations introduced in subsequent chapters, particularly in relation to the influence of doping and additives on ZnO thin films.

II.2. Development procedure

II.2.1. Materials Used

The table **II.1** lists the chemical compounds used in this thesis, along with their properties, which are critical for understanding their behavior and applications. The basic information provided includes their common names, abbreviations (especially in this thesis), chemical formulas, solubility in water at 20°C, boiling points, and the chapters in which these compounds were used.

Table II.1: materials and their specifications.

No	*name*	*Abbreviation*	*Chemical formula*	*Solubility in water g/L (20°)*	*Boiling point (°C)*	*chapter*
01	Zinc acetate dihydrate	ZAD	$C_4H_6O_4Zn.2H_2O$	430	Decomposes	3, 4, 5
02	Strontium nitrate anhydrous	Sr	$Sr(NO_3)_2$	660	645	3, 4, 5
03	Acetone	/	C_3H_6O	Miscible	56.08	3, 4, 5
04	Acetic acid	/	CH_3COOH	Miscible	118	3, 4, 5
05	Ammonia	/	NH_3 (aq)	Miscible	37.7	3, 4, 5
06	Methylene blue	MB	$C_{16}H_{18}ClN_3S$	Miscible	/	3, 4, 5
07	Rose bangal	RB	$C_{20}H_4C_{l4}I_4O_5$	Miscible	/	4
08	Ammoxiciline	AB	$C_{16}H_{19}N_3O_5S$	/	/	5
09	Ethanolamine	EA	C_2H_7NO	Miscible	170	5
10	Polyethylene glycol	PEG	$C_{2n}H_{4n+2}O_{n+1}$	Miscible	/	5
11	Ethylene glycol	EG	$C_2H_6O_2$	Miscible	197.3	5
12	2 butyne-1,4-diol	BD	$C_4H_6O_2$	3740	238	5
13	Sodium dedecylsulphate	SDS	$C_{12}H_{25}NaO_4S$	/	206	5
14	Ethylenediaminetetra acetic acid	EDTA	$C_{10}H_{16}N_2O_8$	1	/	5
15	Hydrogen peroxide	/	H_2O_2	Miscible	150.2	4
16	Sodium hydroxide	SODA	NaOH	1000	1.388	4,5
17	Hydrochloric acid	/	HCl	720	-85.05	4
18	Deionized water	/	H_2O	/	100	3, 4, 5

II.2.2. Preparation of substrates

This work, ZnO films were deposited on glass substrates using the SILAR technique. Glass substrates (dimensions: 76.2 mm × 25.4 mm × 1 mm) were made of clear glass with unground edges. The glass substrate was cleaned first with distilled water and then with dilute acetic acid solution (CH_3COOH: H_2O, 1:10, v/v), for 10 minutes each in an ultrasonic bath up to 50°, then rinsed with acetone (C_3H_6O) and distilled water and finally dried with a stream of air.

II.2.3. Preparation of solutions

Preparation of an undoped ZnO and Sr-Doped ZnO solutions:

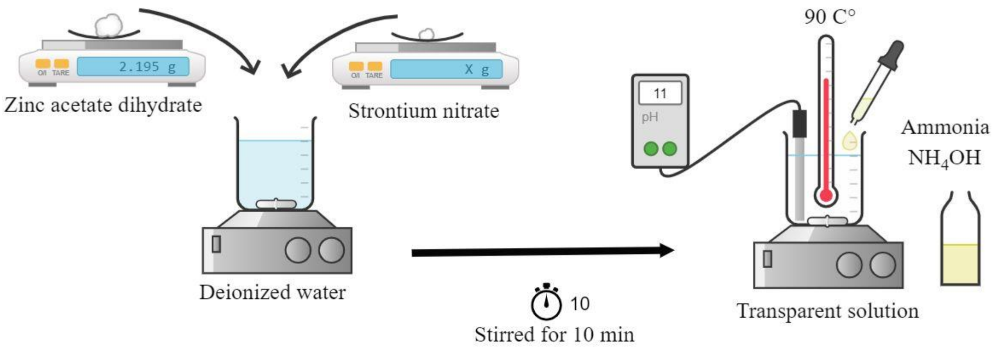

Scheme II.1. Synthesis procedure for preparation of an undoped ZnO solution and Sr-doped ZnO.

For Sr-doped ZnO, the preparation involves adding a strontium precursor to the zinc precursor solution. Strontium doping introduces Sr^{2+} ions, which substitute for Zn^{2+} in the ZnO lattice during the film growth process.

II.2.4. Preparation Steps

II.2.4. 1.Dissolution of Precursors

A measured amount of zinc acetate dihydrate (2.195 g) is dissolved in 100 ml of deionized water under stirring. Strontium nitrate (X g, where X depends on the desired Sr concentration) is added to the same solution. Sr^{2+} ions mix with Zn^{2+} ions in the solution (**Scheme II.1)**.

II.2.4. 2.Stirring and heating

The solution was stirred at 90°C for 10 minutes to ensure complete dissolution and homogenization, resulting in a transparent, homogeneous solution.

The chemical reactions below describe the synthesis process for undoped ZnO [24]:

$$Zn(CH_3COO)_2\,.2H_2O \rightarrow Zn^{2+} + 2CH_3COO^- + 2H_2O \tag{01}$$

$$NH_4OH \rightarrow NH_4^+ + OH^- \tag{02}$$

$$Zn^{2+} + 2OH^- \rightarrow Zn(OH)_2 \tag{03}$$

II.2.5. Important considerations for solutions

II.2.5.1. Concentration of Precursors

The concentration of zinc and strontium precursors determines the activation ratio. For strontium-doped zinc oxide, the mass ratio of Sr^{2+} to Zn^{2+} can vary depending on the level of activation required.

Chapter 3 we used 5 samples with different concentrations of strontium 0, 1, 3, 5 and 7 wt.%.

For chapter 4 we used higher concentrations of strontium than 0, 20, 40, 60 and 80 wt.%.

For the last chapter we chose the sample with the highest yield which was sample 5 and added some different chemicals to it to improve its properties.

All percentages are by mass, an electronic scale (4 numbers) was used to weigh the amount of zinc and strontium. A graduated cylinder was also used to measure distilled water to produce all solutions.

II.2.5.2. pH Control

Maintaining an appropriate pH (around 10~11) is crucial for stabilizing the cations and preventing unwanted precipitation of hydroxides.

Ammonia acts as a ligand, stabilizing Zn^{2+} ions in solution and preventing their premature precipitation as $Zn(OH)_2$. The use of ammonia is critical for forming thin films with good homogeneity and adhesion.

II.2.5.3. Temperature and Mixing

Stirring at elevated temperatures (90°C) ensures the precursors dissolve fully, forming a stable and transparent solution.

II.3. Thin films by SILAR method

The Successive Ionic Layer Adsorption and Reaction (SILAR) method, first introduced by Ristov et al. in 1985, is a relatively new and less explored thin film deposition technique. The term "SILAR" was coined by Nicolau in the same year and further elaborated in subsequent studies by Nicolau and collaborators, focusing on the deposition of ZnS, CdZnS, and CdS thin films [1]. This method has proven effective for depositing thin films of a wide range of chalcogenides, including binary compounds from groups I–VI, II–VI, III–VI, V–VI, and VIII–VI, as well as ternary chalcogenides such as I–III–VI, II–II–VI, II–III–VI, II–VI–VI, and II–V–VI systems, along with composite films.

II.3.1. Deposition process by SILAR using dip-coating

The synthesis of pure ZnO and Sr-doped ZnO thin films was carried out using the dip-coating technique (HOLMARC, Model No. HO-TH-02B).

The SILAR technique, short for Successive Ionic Layer Adsorption and Reaction, is a widely used method for producing thin films, particularly in the field of nanotechnology and materials science. It is a versatile, cost-effective and scalable approach for the deposition of thin films of different materials on different substrates. This technique was utilized throughout this thesis.

II.3.2. Key Advantages of SILAR with Dip-Coating

The Successive Ionic Layer Adsorption and Reaction (SILAR) method with dip-coating technique offers a combination of simplicity, cost-effectiveness, and scalability, making it a highly versatile technique for thin film deposition. Its straightforward process involves sequential immersion of a substrate into cationic and anionic precursor solutions, enabling deposition without the need for expensive equipment or high-vacuum environments. This characteristic significantly reduces operational costs and supports large-scale production. The method operates effectively at ambient or moderately elevated temperatures, making it suitable for use with heat sensitive substrates, such as polymers, that cannot withstand high-temperature processing. The SILAR dip-coating technique also allows precise control over film thickness and composition by adjusting the number of deposition cycles or modifying precursor concentrations. This precision is crucial for tailoring thin film properties for specific applications. These advantages collectively establish the SILAR dip-coating method as a robust and adaptable tool for fabricating high-quality thin films in diverse fields such as optoelectronics, energy conversion, and environmental remediation.

II.3.3. Principle of the method

The scheme **II.2** illustrates the SILAR synthesis process for the preparation of Sr-doped ZnO thin films. The process consists of multiple steps, collectively forming one SILAR cycle, which is iteratively repeated to achieve the desired thin film thickness**.**

The cycle begins with a clean glass substrate, which ensures that no contaminants interfere with the uniform deposition of the thin film. Proper substrate cleaning is critical to achieving high-quality thin films.

The clean substrate is immersed into a cationic solution containing metal ions Zn^{2+} and Sr^{2+}. This solution is typically heated to 90°C to enhance ion adsorption onto the substrate surface. The immersion lasts for 30 seconds, during which the ions adsorb onto the substrate.

The substrate is then transferred to hot distilled water (also heated to 90°C) for another 30 seconds. This step removes excess, loosely bound ions and prevents unwanted side reactions or agglomeration during subsequent steps.

The substrate is rinsed in distilled water (room temperature) to wash off unreacted precursors and by products, ensuring that only the thin film layer remains on the surface.

To ensure robust and reliable results, the rinsing procedure was repeated 30 times for each sample. Each experiment was conducted in triplicate, and each analysis was repeated twice to confirm reproducibility. This rigorous approach, combined with the application of appropriate statistical analyses, provided strong evidence for the validity of our findings.

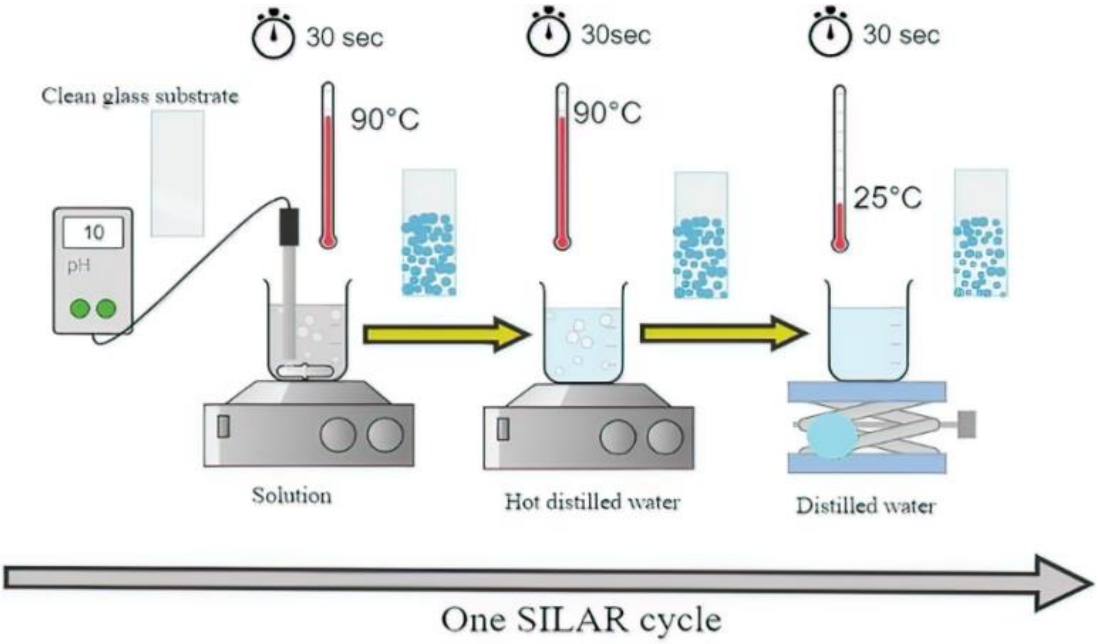

Scheme II.2. Synthesis procedure for Sr-doped ZnO thin films using the SILAR technique.

II.3.4. Reaction mechanism

The deposition of Sr-doped ZnO thin films via the Successive Ionic Layer Adsorption and Reaction method involves a stepwise chemical reaction mechanism. Here's an explanation of the mechanism during each stage of a SILAR cycle:

II.3.4.1. Cationic Solution (Zn^{2+} and Sr^{2+} adsorption)

The clean substrate is immersed in an aqueous solution containing zinc ions (Zn^{2+}) and strontium ions (Sr^{2+}), typically prepared from precursors such as zinc acetate ($Zn(CH_3COO)_2.2H_2O$) and strontium nitrate ($Sr(NO_3)_2$).

On immersion, the metal cations adsorb onto the substrate surface through ionic interaction. This adsorption is facilitated by the pH and temperature of the solution, which control the availability of ions.

$$\text{substrate} + \text{Zn}^{+2} + \text{Sr}^{+2} \rightarrow \text{substrate} - (\text{Zn}^{2+}, \text{Sr}^{+2}) \qquad (04)$$

The Sr^{2+} ions are partially incorporated into the Zn^{2+} adsorption sites, initiating doping.

II.3.4.2. Hydroxide Precipitation Reaction

The substrate is immersed in a solution containing hydroxide ions (OH^-), typically from ammonium hydroxide (NH_4OH).

The adsorbed Zn^{2+} and Sr^{2+} react with OH^- to form zinc hydroxide ($Zn(OH)_2$) and strontium hydroxide ($Sr(OH)_2$) as precipitates on the substrate.

$$\text{Zn}^{+2} + 2OH^- \rightarrow Zn(OH)_2 \qquad (05)$$

$$\text{Sr}^{+2} + 2OH^- \rightarrow \text{Sr(OH)}_2 \qquad (06)$$

II.3.4.3. Rinsing with Hot Distilled Water

The substrate is rinsed in hot distilled water (90°) to remove loosely bound ions and impurities.

This step ensures that only firmly adsorbed Zn^{2+} and Sr^{2+} remain on the substrate.

II.3.4.4. Rinsing (Room-Temperature Distilled Water)

The substrate is rinsed with distilled water at room temperature (25°C) for 30 seconds to remove unreacted hydroxide ions and other soluble by products, leaving behind a layer of hydroxides.

II.3.4.5. Thermal Decomposition (Optional)

After several SILAR cycles, the substrate is typically annealed at high temperatures (450°C) to convert the hydroxides into oxides and allow Sr^{2+} ions to substitute Zn^{2+} ions in the ZnO crystal lattice.

$$Zn(OH)_2 \rightarrow \Delta\, ZnO + H_2O \quad (07)$$

$$Sr(OH)_2 \rightarrow \Delta\, SrO + H_2O \quad (08)$$

The Sr^{2+} ions substitute Zn^{2+} ions in the ZnO lattice, forming Sr-doped ZnO thin films.

$$ZnO\ lattice + Sr^{+2} \rightarrow Zn_{1-x}Sr_xO \quad (09)$$

The resulting Sr-doped ZnO thin film has the general formula $Zn_{1-x}Sr_xO$, where x represents the doping concentration of Sr.

II.3.5. Number of Immersion Cycles

In the Successive Ionic Layer Adsorption and Reaction method, the number of immersion cycles critically determines the thickness, crystallinity, and overall quality of the deposited thin films [2]. Each immersion cycle corresponds to a single sequence of adsorption, rinsing, reaction, and final rinsing, which collectively adds a thin layer of material to the substrate. By increasing the number of cycles, the thickness of the thin film can be systematically controlled, making the SILAR method highly versatile for applications requiring precise film thickness. However, an excessive number of cycles may lead to non-uniform films or structural defects due to agglomeration or uneven growth. Conversely, too few cycles may result in incomplete coverage of the substrate. Optimizing the number of immersion cycles is essential to achieve the desired film properties, such as uniformity, transparency, or dopant concentration, depending on the application. Typically, the number of cycles is selected based on the specific material system, precursor concentration, and intended application, ensuring a balance between growth rate and film quality. For this reason, we conducted several experiments and set the number of cycles at 30.

II.3.6. Advantages of the SILAR process

There are many deposition techniques to produce thin layers of ZnO and ZnO/Sr but we have chosen in our work the SILAR technique for following reasons [3,4,5]:

1. A wide range of precursors can be used; however, the compound must be soluble in a solvent to facilitate the atomization of the solution.
2. The technique enables the deposition of a wide range of materials.
3. This method is particularly effective for the deposition of conductive oxides.
4. The underlying principles of the technique always remain the same.
5. This methodology is characterized by its simplicity and adaptability.
6. The technique facilitates the direct growth and concurrent deposition of doped and multilayered materials.
7. It is a reproducible process that is relatively brief in duration.
8. The approach mitigates material wastage post-reaction due to the absence of precipitate formation.
9. It is capable of depositing films on substrates that exhibit lower mechanical robustness.

II.3.7. Disadvantages of the SILAR process

- Achieving uniform and defect-free films can be challenging, especially on substrates with complex geometries.
- The layer-by-layer nature of the process makes it slower compared to other deposition methods like chemical vapor deposition (CVD).
- Residual precursor or by products may remain on the substrate if rinsing steps are not carefully optimized.
- Slight variations in precursor concentration, immersion time, or temperature can affect the film quality, leading to reproducibility issues.
- The process is sensitive to the reactivity and stability of the precursor solutions, which may limit the range of materials that can be deposited [6].

II.3.8. Applications of SILAR

The Successive Ionic Layer Adsorption and Reaction (SILAR) method is a simple and cost-effective technique widely used for fabricating thin films and nanostructures. Its primary application is in developing materials for photovoltaic, such as semiconductor films for solar cells [7], where precise control over film thickness and composition is essential for optimizing energy conversion efficiency. SILAR is also employed in photocatalysis to create nanostructured materials capable of breaking down pollutants under sunlight or artificial light (purification of water from organic pollutants such as colourants (methylene blue)) [8]. Additionally, it finds use in sensors [9], particularly gas and humidity sensors, where its ability to produce uniform and highly adherent films enhances sensor sensitivity and durability. Other applications include thermoelectric materials, supercapacitors, and optoelectronic devices. The method's versatility, scalability, and ability to deposit films on substrates of various shapes and sizes make it a valuable tool in modern material science and engineering.

II.4. Drying and reheating

An important parameter of interest in SILAR deposition concerns the characteristics of the thermal treatment carried out after deposition. This phenomenon is obviously not unique to SILAR, as annealing is usually carried out after the deposition process is complete. The results of high temperature annealing are therefore generally comparable to those obtained with samples produced by alternative wet chemical methods. The process of thermal annealing is primarily carried out to decompose and remove organic impurities and to facilitate crystallization and grain growth within the deposited layers, which is often accompanied by an improvement in surface roughness [10]. The films were annealed at 450°C for approximately 1.5 hours, with the temperature ramped at 5 °C per minute.

II.5. Analysis of film thickness: gravimetric method

The gravimetric method is a simple and precise way to analyze the thickness of a thin film by measuring the mass difference of a substrate before and after the deposition process, requiring minimal specialized equipment. Offers direct measurements without the need for complicated instrumentation. The film thickness can be determined using the following procedure and formula.

II.5.1. Substrate Preparation

Clean and dry the substrate thoroughly to remove contaminants as mentioned above (**II.2.1.)**.Measure and record the initial mass of the substrate ($m_{initial}$) using a highly sensitive analytical balance (microgram-level precision is ideal).

Deposit the thin film onto the substrate using SILAR method. Ensure uniformity in the deposition to avoid inaccuracies in thickness estimation.

II.5.2. Final Mass Measurement

After deposition, leave the film to dry and then put it in the oven for an hour and a half, then measure the final mass of the substrate with the deposited film (m_{final}).The thickness of the film can be calculated using [11]:

$$t = \frac{m_{film}}{A.\rho} \qquad (10)$$

where t is thickness of the film (nm), A is area of the substrate where the film is deposited (cm^2), In this case, the thin film is formed on both sides of the substrate and the area is calculated on both sides with the same dimensions. ρis the density of the deposited material (g/cm^3), obtained from literature , XRD data(fiche ASTM). m_{film} is the mass of deposited film (g).It is calculated in the following way:

$$m_{film} = m_{final} - m_{initial} \qquad (11)$$

II.6. Contact angle

The water contact angles (WCA) were determined using an improvised method. In this approach, a mobile camera is set up so that it is directed at a white light source. The sample holder is located in the centre at a constant distance of 7 cm and is aligned at an approximate angle of 1.5° to the camera. For each experiment, a 10 µl drop of water is carefully positioned on the sample using a micropipette (SCILOGEX-iso 9001/13485). The zoom function of the mobile camera is calibrated to ensure the clarity of the images obtained. The device is coated in dark grey to prevent the occurrence of light reflections. Finally, the images obtained are transferred to a computer to analyse the water contact angle using the IC Measure software. Each sample was subjected to five separate tests at room temperature. The contact angle is given by the following law [12].

$$\vartheta = \frac{\vartheta_1 + \vartheta_2}{2} \qquad (12)$$

where ϑ is the average angles of ϑ_1 and ϑ_2 (°), ϑ_1 and ϑ_2 (°) are the angles on the left and the right side, respectively.

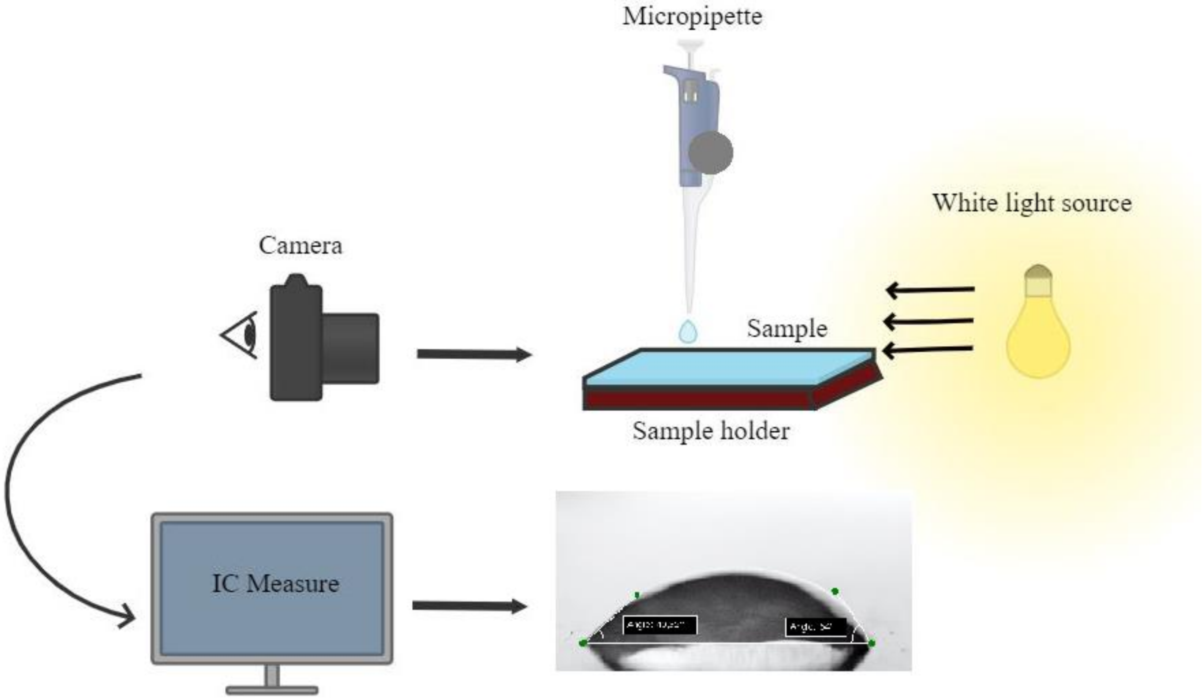

Scheme II.4. Procedure for water droplet contact angle measurements.

Scheme **II.4** illustrates a setup for measuring water contact angles on thin films. This type of measurement evaluates the wettability of the thin film surface and provides insights into its hydrophobicity or hydrophilicity.

II.6.1. Contact Angle Analysis

1. *Hydrophilic Surface:* A contact angle < 90° indicates the surface attracts water, which is typical of polar or rough surfaces.
2. *Hydrophobic Surface:* A contact angle > 90° shows the surface repels water, suggesting non-polar or smooth properties.
3. *Superhydrophobic Surface:* A contact angle > 150° signifies extremely water-repellent behavior.

II.6.2.The contact angle reflects the surface energy of the thin film

The contact angle is a key indicator of surface energy in thin films, especially in photocatalytic systems. Photocatalytic thin films often composed of semiconductors like TiO_2 or ZnO, exhibit surface energy changes due to their interaction with light. These changes influence the contact angle by modulating the film's hydrophilicity or hydrophobicity, which is critical for enhancing photocatalytic activity. When irradiated with light, the generation of photoinduced charge carriers (electrons and holes) can alter the surface chemistry, such as the dissociation of water molecules or the degradation of organic contaminants. This results in an increase in surface energy, typically reducing the contact angle and promoting water spreading. Such behavior enhances the self-cleaning, antifouling, and degradation efficiency of photocatalytic surfaces. Therefore, monitoring and controlling the contact angle provides a valuable approach to optimizing the performance of photocatalytic thin films in environmental and industrial applications.

II.7. Characterization techniques

II.7.1. X-ray diffraction (XRD)

X-ray diffraction enables a complete crystallographic examination of thin films over their entire thickness. The recorded diffractograms not only provide information about the crystalline architecture of the phases manifested in the layer, but also provide important information about the orientation of the grains, their dimensions, their imperfections and their confined state. In this study, we used the Mini Flex 600with CuKa radiation (λ = 1.541A°). The measurement range was $20° \leq 2\theta \leq 80°$ at a rate of 0.03 s^{-1}. The analyses were carried out in the PTLA laboratory of the research laboratories of the University of Biskra.

II.7.2. Scanning electron microscopy (SEM)

The structural properties of the films were analyses using a Bruker Nano Gmbh (XFlash Detector 610M) scanning electron microscope (SEM). The analyses were carried out in the PTLA laboratory of the research laboratories of the University of Biskra. The samples do not require special preparation. However, a primary metallization procedure was used, in which a thin (10 nm) layer of silver is applied to the surfaces of the samples prepared with SILAR, especially if the intention is to observe isolated samples (on glass).

II.7.3. Energy dispersive spectroscopy (EDS)

The chemical composition of the deposited films was evaluated by X-ray microanalysis, in particular by energy dispersive X-ray spectroscopy (EDS), in conjunction with a Bruker Nano Gmbh (XFlash Detector 610M) scanning electron microscope (SEM). The area analyzed by EDS corresponds to the dimensions of the area visualized by the SEM, generally between 1 and 100 μm^2. The accuracy of EDS spectral analysis is estimated at around 1%. This method facilitates both the identification and quantification of the chemical elements present in a given sample. The analyses were carried out in the PTLA laboratory of the research laboratories of the University of Biskra.

II.7.4. Mechanical profilometer

This instrument was used to accurately assess the surface properties of our samples. The mechanical interferometer (KLA-Tencor P-7) allows the quantification of roughness, step heights and three-dimensional visualization of components. A mechanical profilometer is an advanced instrument for quantitatively assessing the surface profile of a sample by physically traversing a tiny diamond-tipped stylus. This device produces a topographical representation of the surface, revealing features such as roughness, waviness, steps and various other irregularities. It is an indispensable tool in quality assurance, scientific research and industrial production to assess the integrity and functionality of surfaces. The analyses were carried out in the PTLA laboratory of the research laboratories of the University of Biskra.

II.7.5. Atomic force microscopy (AFM)

Atomic Force Microscopy (AFM) is a powerful and versatile imaging technique widely used in nanoscience and materials research. It operates by scanning a sharp tip, mounted on a flexible cantilever, across the surface of a sample to generate high-resolution topographical maps at the nanometer scale. The tip interacts with the sample through forces such as van der Waals, electrostatic, or mechanical interactions, which are detected and translated into precise measurements of surface features. The 3D, 2D surface topography and surface roughness were analyzed by Atomic Force Microscopy (BRUKER) of the CRAPC Biskra

II.7.6. Ultraviolet-Visible spectroscopy

Ultraviolet-Visible (UV-Vis) spectroscopy is a widely used analytical technique for studying the absorption and transmission of light in the ultraviolet (200–400 nm) and visible (400–700 nm) regions of the electromagnetic spectrum. This technique is based on the principle that molecules absorb light at specific wavelengths, causing electronic transitions between molecular energy levels. UV-Vis spectroscopy measures the intensity of light before and after passing through a sample, generating an absorption spectrum that reveals the sample's composition, concentration, and chemical structure. It is a versatile tool employed in a variety of fields, including chemistry, biochemistry, materials science, and environmental science. UV-Vis spectroscopy is particularly useful for analyzing conjugated systems, chromophores, and transition metal complexes, as well as for monitoring reaction kinetics. The optical transmission spectra of the ZnO thin films were analyzed using a UV-Vis JASCO V-770 spectrophotometer within a wavelength range of 200 nm – 1200 nm. The analyses were carried out in the PTLA laboratory of the research laboratories of the University of Biskra.

II.8. Band gap

The Tauc plot method is a graphical technique used to estimate the optical band gap of a material. It involves analyzing the material's absorbance or absorption coefficient (α) as a function of photon energy ($h\nu$). First, the absorption coefficient is calculated from the UV-Vis spectroscopy data of the material. Than the Tauc relation is applied [13]:

$$(\alpha h\nu)^n = A(h\nu - Eg) \qquad (13)$$

where A is a constant, Eg is the band gap, $h\nu$ is the photon energy, and $n$depends on the type of electronic transition (e.g., n=2 for indirect transitions, n=1/2 for direct transitions). A plot of $(\alpha h\nu)^n$ against $h\nu$ is created and the linear part of the curve is extrapolated to the x axis ($h\nu$), where $(\alpha h\nu)^n$=0. The x-intercept of this line gives the band gap energy Eg. This method is often used for semiconductors and optical materials.

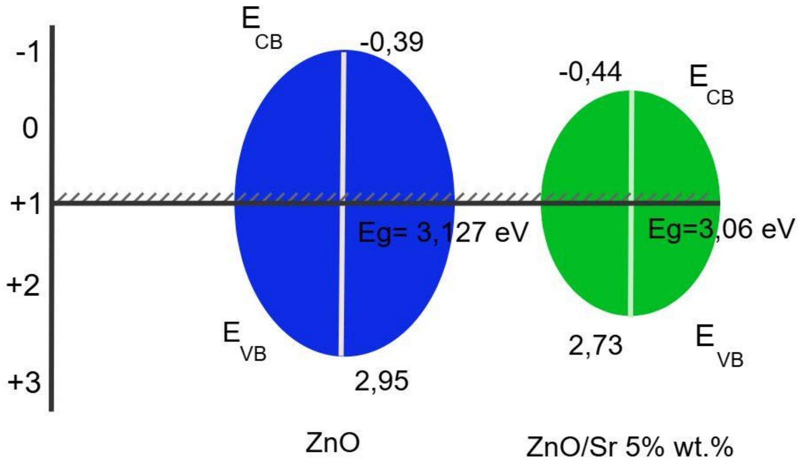

Scheme II.3. Energy bandgap of pure ZnO and Sr-doped ZnO thin films.

The provided scheme **II.3** compares the energy band structure of pure ZnO and Sr-doped ZnO with 5%. For pure ZnO, the conduction band minimum (E_{CB}) is at -0.39 eV, and the valence band maximum (E_{VB}) is at 2.95 eV, resulting in a band gap (Eg) of 3.127 eV. When Sr doping is introduced, the E_{CB} shifts to -0.44 eV, and the E_{VB} lowers to 2.73 eV, reducing the band gap to 3.06 eV. This reduction in the band gap suggests that Sr doping introduces localized states or alters the electronic structure of ZnO, enabling enhanced light absorption, especially in the visible spectrum.

The band gap narrowing effect observed with Sr doping is supported by studies that highlight the role of dopants in modifying the electronic properties of ZnO. As an alkaline earth metal, Sr influences the crystal structure and electron density, altering the energy levels. According to research, doping ZnO with elements like Sr enhances its optoelectronic properties, making it suitable for applications in photocatalysis, solar cells, and UV light detection.

II.9. Photocatalytic

Photocatalysis is a promising and sustainable approach to addressing environmental pollution. It leverages the ability of photocatalytic materials to harness light energy, typically from sunlight or artificial sources, to drive chemical reactions that degrade pollutants into less harmful or inert substances. This technology has gained significant attention due to its potential for treating a wide range of contaminants, including organic dyes, pharmaceuticals, pesticides, and industrial wastes, without generating harmful by-products. **Scheme II.5** shows the experimental method used in this thesis.

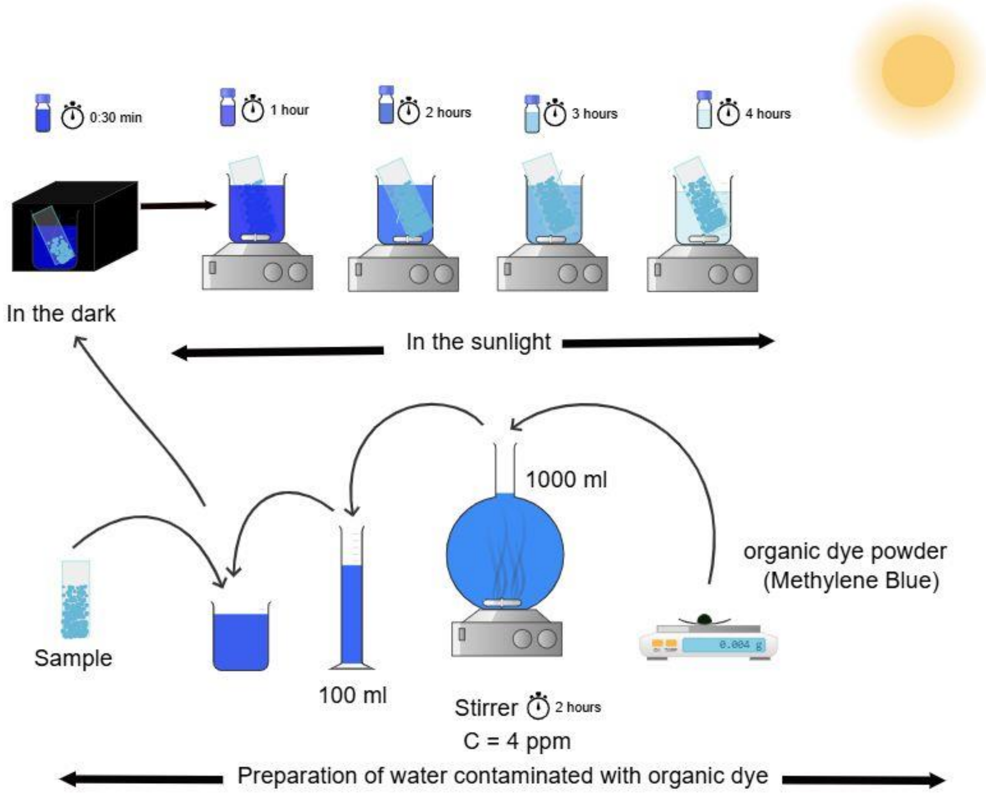

Scheme II.5. Decomposition of methylene blue under to sunlight.

II.9.1. Chapter 3

Photocatalytic tests under sunlight were conducted on January 8th, 10th, and 11th, 2023, between 11 a.m. and 3 p.m., in Biskra, Algeria, using methylene blue (MB) dye as a model pollutant. The results demonstrated that MB solutions degraded effectively under sunlight irradiation using both pure ZnO and Sr-doped ZnO thin films as photocatalysts. Thin film photocatalysts (25 cm^2) were immersed in 100 mL of an MB solution at a concentration of 4 ppm and a neutral pH (7). The experiments were performed under sunlight with a radiation intensity of approximately 0.135 W/cm^2. Prior to irradiation, the thin films were allowed to interact with the MB solution in the dark for 30 minutes to establish adsorption-desorption equilibrium. During the experiments, the MB solution was stirred at 250 rpm to ensure uniform mixing.

II.9.2. Chapter 4

The photocatalytic activity of the dyes methylene blue (MB) and rose bengal (RB) was evaluated under sunlight on November 12, 2023, based on the prevailing weather conditions in Biskra, Algeria. For the experiment, 4 ppm of the photocatalyst was dispersed in 1000 mL of the MB dye solution (concentration 0.004 g/L) and magnetically stirred. Individual samples of 100 mL were prepared and aliquots were taken every 60 minutes to monitor degradation. Before the solutions were exposed to sunlight, they were kept in the dark for 30 minutes to ensure adsorption-desorption equilibrium. In addition, the degradation of RB dye at a concentration of 3 ppm (0.003 g/L) was studied under identical optimal conditions to evaluate its influence on the degradation rate.

To increase the efficiency of methylene blue (MB) degradation and to investigate the effects of pH on photocatalytic performance, hole scavenger and pH adjustment tools were used. The experiment took place on November 15, 2023 in Biskra, Algeria. A solution of 0.004 g MB was prepared in 1000 mL of double distilled water and certain amounts of SODA (1 g NaOH), H_2O_2 (1.5855 mL) and HCl (2 mL) were added to adjust the pH and add scavengers. Each sample was then prepared by mixing 100 mL of the MB solution with the selected additives under magnetic stirring until complete dissolution. The photocatalytic degradation of MB in the presence of these scavengers was tested using films with 40% active composition selected for their superior performance in photocatalytic applications.

II.9.3.Chapter 5

Sr-doped ZnO (5 wt.%) thin films were used as photocatalytic agents for the degradation of methylene blue (MB) solutions under natural solar irradiation. The photocatalyst samples were immersed in 100 ml of a 4 ppm MB solution in a beaker. To replicate a solar collector system, the beaker was manually moved so that it followed the path of the sun throughout the duration of the experiments. Prior to irradiation, the photocatalyst and MB solution were stored in a dark environment for 30 minutes to facilitate the establishment of adsorption equilibrium. Thereafter, the irradiation experiments were performed from 10:00 a.m. to 3:00 p.m., with the MB solution has stirredat a speed of 250 revolutions per minute.

A solution of Amoxicillin at a concentration of 10 mg/L (10 ppm) was prepared in advance using double-distilled water. The solution was stirred for 1 hour to ensure homogeneity, and 1 g of SODA was added to adjust the pH to 7, enhancing the solubility of the antibiotic. A thin film, measuring 50 mm in length and 25.4 mm in width, was placed in a beaker containing 50 mL of the antibiotic solution for further experimentation. The photocatalytic oxidation process was initiated when light radiation interacted with the thin-film photocatalyst immersed in the pollutant-laden solution. This experiment was conducted on January 14, 2024, under the prevailing weather conditions in Biskra, Algeria. Samples of the treated solution were collected from the reactor every hour, and the antibiotic concentration was measured using a UV-Vis spectrophotometer. Control experiments were conducted under light irradiation without the photocatalyst to evaluate its impact on the process. Additionally, the absorption properties of the thin films were evaluated in the dark for 30 minutes to establish a baseline for adsorption behavior.

II.9.4. Calculate the photocatalytic decomposition efficiency

Prepare a solution of the dye (MB, RB, AB) of known concentration (e.g., 4 mg/L, 10 mg/L). Measure the initial absorbance (A_0) of the dye solution using a UV-Vis spectrophotometer at the characteristic wavelength of dye (MB around 663 nm, RB around 546 nm and AB around 287 nm). Expose the dye solution to sunlight in the presence of ZnO or Sr-doped Zno thin films for a specific duration (X hours) as shown in the scheme **II.6**. Stir the solution during the exposure to ensure uniform interaction between dye molecules and the catalyst (thin film). After the exposure, measure the final absorbance (A_t) of the dye solution at the same wavelength.

The change in dye concentration was tracked using a UV-Vis spectrophotometer, and the photocatalytic efficiency (η) was calculated using the following equation [14]:

$$\eta = \left(\frac{A_0 - A_t}{A_0}\right) \times 100\% \qquad (14)$$

where A_0 and A_t represent the absorbance of dye solution at t=0 and at time t, respectively.

Scheme II.6. Experimental setup for methylene blue photocatalysis.

II.10. Kinetic

The kinetics of the photocatalytic degradation of methylene blue (MB) can be described using pseudo-first-order kinetics, especially when the concentration of the catalyst is significantly higher than that of the substrate. The rate of the reaction can be expressed by the equation [15]:

$$ln\frac{C_0}{C_t} = k \,.\, t \qquad (15)$$

where C_0 is the initial concentration of MB, C_t is the concentration at time t, and k is the rate constant. To calculate the kinetics, one would typically conduct a series of experiments measuring the absorbance of the MB solution at various time (1 hour) intervals using UV-Vis spectroscopy, which allows for determination of the concentration of MB. The absorbance can be converted to concentration using Beer-Lambert's law. By plotting ($\ln\frac{C_0}{C_t}$) against time (t), a straight line should emerge if the reaction follows pseudo-first-order kinetics, and the slope of this line will yield the rate constant k. The values of k can then be used to compare the efficiency of different catalysts or reaction conditions, leading to insights into the mechanistic pathways and overall effectiveness of the photocatalytic process.

II.11. Langmuir isotherm model

The Langmuir isotherm model is used to describe the adsorption of a solute on a homogeneous solid surface. It is based on the hypothesis that adsorption occurs at specific sites, with a monolayer (a single adsorption layer) without interaction between the adsorbed molecules.

In adsorption studies, Ce is the equilibrium concentration of the adsorbate in the solution after the adsorption process has reached equilibrium. It represents the amount of the adsorbate that remains in the solution and is typically measured experimentally every hour. q_e represents the amount of adsorbate adsorbed per unit mass of adsorbent at equilibrium (every hour). It is a key parameter that quantifies how much of the adsorbate (e.g., a pollutant, dye, or gas) has been captured by the adsorbent material at equilibrium. Formula for q_e [16]:

$$q_e = \frac{(C_0 - C_e)\,V}{m} \tag{16}$$

where q_e is the equilibrium adsorption capacity (mg/g). C_0 is the initial concentration of the adsorbate in the solution (mg/L) and C_e is the equilibrium concentration of the adsorbate in the solution (mg/L).V is the volume of the solution (L). m is the mass of the adsorbent used (g).

The Langmuir equation can be expressed as follows[17]:

$$q_e = \frac{q_{max} K_L C_e}{1 + K_L C_e} \tag{17}$$

where q_e is the quantity of solute adsorbed per unit mass of adsorbent (mg/g). q_{max} is the maximum adsorption capacity at surface saturation (mg/g) and K_L is the langmuir constant, linked to adsorption affinity (L/mg).C_e is the concentration of solute at equilibrium (mg/L).

To fit the experimental data to the model, the equation is often transformed into a linear form [17]:

$$\frac{C_e}{q_e} = \frac{1}{q_{max}} \cdot C_e + \frac{1}{K_L q_{max}} \tag{18}$$

By tracing C_e/q_e depending on C_e, a line is obtained, of which:

The intercept (y-axis) is equal to $1/(K_L.q_{max})$ and the slope is $1/q_{max}$.

II.12.The specific surface area of methylene blue

The specific surface area (S_{MB}) represents the total surface area available for adsorption per unit mass of a material. The formula used here calculates the specific surface area based on the monolayer adsorption of methylene blue (MB) molecules on the surface of the material [18].

$$S_{MB} = \frac{q_m . a_{MB} . N_A . 10^{-20}}{M} \tag{19}$$

where S_{MB} is the specific surface area, in $10^{-3}Km^{-2}.Kg^{-1}$ this unit represents square kilometers of surface area per kilogram of material: $1Km^2 = 10^6m^2$, $10^{-3}Km^2 = 1m^2$,so $10^{-3}km^2kg^{-1}$ essentially means m^2kg^{-1}. q_m is the amount of methylene blue adsorbed at the monolayer (mg of MB per gram of adsorbent, $mg.g^{-1}$). a_{MB} is the surface area occupied by one molecule of methylene blue (197.2 $A^{\circ 2}$).N_A is the Avogadro's number ($6.02 \times 10^{23} mol^{-1}$).M is the molecular weight of methylene blue (373.9 g mol^{-1}).10^{-20}: A conversion factor from $Å^2$ to km^2.Each molecule of methylene blue occupies a_{MB}=197.2 $A^{\circ 2}$, which needs to be converted to km^2.1 $A^{\circ 2}$=$10^{-20}km^2$, so $a_{MB} \times 10^{-20}$ gives the area in km^2.

II.13. Conclusion

This chapter has outlined the experimental methodologies employed for the synthesis and characterization of pure and strontium-doped ZnO thin films prepared via the SILAR technique. Key findings include the critical role of strontium doping in modifying the structural, optical, and morphological properties of ZnO thin films, as well as the importance of controlling precursor concentrations, solution pH, and deposition cycles for achieving high-quality films. The use of advanced characterization tools, such as XRD, SEM, AFM, and UV-Vis spectroscopy, provided comprehensive insights into the films' crystallinity, surface topology, and optical properties.

Additionally, the photocatalytic performance and surface wettability of the thin films were investigated, highlighting their potential applications in environmental remediation and other advanced technologies. The integration of photocatalytic activity and hydrophilic properties opens avenues for self-cleaning surfaces and efficient degradation of organic pollutants. By laying a strong experimental and theoretical foundation, this chapter sets the stage for further exploration of the enhanced properties of ZnO thin films achieved through doping and additive modifications, which are discussed in subsequent chapters.

References of chapter II

[1] Pathan, H. M., and C. D. Lokhande. "Deposition of metal chalcogenide thin films by successive ionic layer adsorption and reaction (SILAR) method." *Bulletin of Materials Science* 27 (2004): 85-111.

[2] Chaudhari, K. B., et al. "Chemical synthesis and characterization of CdSe thin films deposited by SILAR technique for optoelectronic applications." *Journal of Science: Advanced Materials and Devices* 1.4 (2016): 476-481.

[3] Suryawanshi, Rushikesh R., et al. "Successive ionic layer adsorption and reaction (SILAR) method for metal oxide nanostructures." *Solution Methods for Metal Oxide Nanostructures.Chapter* 10. Elsevier, 2023. 175-196.

[4] Pedanekar, R. S., S. K. Shaikh, and K. Y. Rajpure. "Thin film photocatalysis for environmental remediation: A status review." *Current Applied Physics* 20.8 (2020): 931-952.

[5] Ratnayake, Samantha Prabath, et al. "SILAR deposition of metal oxide nanostructured films." *Small* 17.49 (2021): 2101666.

[6] Nimalan, T., and M. Begam. "Physical and chemical methods: a review on the analysis of deposition parameters of thin film preparation methods." *Int. J. Thin. Fil. Sci. Tec* 13.1 (2024): 59-66.

[7] Chauhan, Asha, A. K. Shrivastav, and Anjali Oudhia. "Synthesis and characterization of ambient-processed FTO/ZnO/CsPbBr2Cl/C perovskite solar cell deposited by SILAR method." *Optical Materials* 130 (2022): 112575.

[8] Sathya, M., et al. "Synthesis and characterization of cadmium doped on ZnO thin films prepared by SILAR method for photocatalytic degradation properties of MB under UV irradiation." *The European Physical Journal Plus* 138.1 (2023): 1-12.

[9] Patil, Vithoba L., et al. "Fabrication of nanostructured ZnO thin films based NO2 gas sensor via SILAR technique." *Sensors and Actuators B: Chemical* 239 (2017): 1185-1193.

[10] Montaño, Beatriz, et al. "In-depth study of the effect of annealing temperature on the structural, chemical, and optical properties of MAPI thin films prepared by a one-step deposition method." *Journal of Materials Science: Materials in Electronics* 34.12 (2023): 1016.

[11] Shaikh, A. A., M. R. Waikar, and R. G. Sonkawade. "Effect of different precursors on electrochemical properties of manganese oxide thin films prepared by SILAR method." *Synthetic Metals* 247 (2019): 1-9.

[12] Althamthami, Mohammed, et al. "Effect of different Cu: Co film concentrations on photocatalytic reactions of ethanol, MB, AMX, and Cr (VI): A study of film properties & effects of photooxidation." *Journal of Environmental Chemical Engineering* 11.6 (2023): 111247.

[13] Mehra, Sonali, et al. "Development of visible light-driven SrTiO3 photocatalysts for the degradation of organic pollutants for waste-water treatment: Contrasting behavior of MB & MO dyes." *Optical Materials* 136 (2023): 113344.

[14] Temam, Elhachmi Guettaf, et al. "Photocatalytic activity of Al/Ni doped TiO2 films synthesized by sol-gel method: Dependence on thickness and crystal growth of photocatalysts." *Surfaces and Interfaces* 31 (2022): 102077.

[15] Wang, Lili, et al. "Constructing recyclable photocatalytic BiOBr/Ag nanowires/cotton fabric for efficient dye degradation under visible light." *Arabian Journal of Chemistry* 16.4 (2023): 104624.

[16] Ezzati, Rohollah. "A new insight into the surface adsorption in the solution phase: A modification of the Langmuir isotherm." *Water Environment Research* 96.4 (2024): e11019.

[17] Itodo, A. U., H. U. Itodo, and M. K. Gafar. "Estimation of specific surface area using Langmuir isotherm method." *Journal of Applied Sciences and Environmental Management* 14.4 (2010).

[18] Itodo, A. U., et al. "Application of methylene blue and iodine adsorption in the measurement of specific surface area by four acid and salt treated activated carbons." *New York science journal* 3.5 (2010): 25-33.

Chapter III:

Enhancing Photocatalytic Stability of Hydrophilic Sr-Doped ZnO Thin Films Via SILAR Method

This chapter is based on: Mokrani Nourelhouda, et al. "Boosting photocatalytic stability: hydrophilic Sr-doped ZnO thin films prepared via the SILAR method for enhanced performance over multiple cycles." *Physica Scripta* 99.9 (2024): 0959a4.

III.1. Introduction

Environmental degradation due to organic contaminants in wastewater has become an increasingly pressing issue in recent years [1]. Photocatalysis has emerged as a sustainable and efficient method for degrading dyes with semiconductor photocatalysts [2,3]. Numerous studies have focused on semiconductor materials such as TiO_2, ZnO, and nanocomposites to degrade methylene blue under various light sources, including UV, visible, and solar radiation [4,5]. Findings from these studies indicate that degradation rates can reach up to 96% within a short irradiation period, highlighting photocatalysis as an environmentally friendly and efficient method for wastewater treatment, providing a promising solution to the challenges posed by organic pollutants in aquatic systems.

Semiconductor photocatalysis, particularly utilizing thin film photocatalysts, is a highly adaptable technology with a wide range of applications, including anti-fogging, energy saving, deodorization, sterilization, self-cleaning, photodiodes, air purification, and wastewater treatment [6,7]. The generation of reactive oxygen species under light irradiation plays a pivotal role in breaking down organic pollutants, demonstrating the potential for their complete mineralization [8,9]. Among semiconductor materials, zinc oxide stands out due to its promising properties, with extensive efforts aimed at broadening its light absorption range into the visible spectrum. This is achieved by coupling ZnO with carbon-based materials or transition/rare earth metals, through doping or surface decoration, to enhance its photocatalytic activity [10]. Recent studies have also explored indirect excitation by transferring energy from host materials to rare earth ions, opening up new possibilities for efficiently activating these ions and boosting photocatalytic performance [11,12]. These developments underline the continuous progress in optimizing semiconductor photocatalysis for diverse environmental and industrial applications.

The impact of doping metals such as Cr, Sr, and Ag on the properties of ZnO thin films has been extensively studied [3,10,13]. The variation in electronic structures between rare earth and non-rare earth metals plays a significant role in shaping the photocatalytic performance of ZnO thin films. Rare earth metals, including Samarium, Gadolinium, Europium, Cerium, Neodymium, and Dysprosium, have been found to enhance the optical, magnetic, and photocatalytic properties of ZnO nanomaterials when used as dopants [14]. Moreover, the incorporation of metallic and non-metallic dopants into ZnO structures has demonstrated substantial improvements in their stability and reusability, resulting in exceptional photocatalytic efficiency for degrading a wide range of organic pollutants [15].

Doping ZnO thin films with strontium (Sr) improves visible light absorption by altering the band gap values and crystalline structure. The addition of Sr to the ZnO matrix causes a shift in the band gap, reflecting an increase in n-type carrier concentration [16]. This shift enhances the material's ability to absorb visible light, making it responsive to a wider range of wavelengths [17]. Additionally, Sr-doped ZnO nanoparticles demonstrate improved photocatalytic activity under visible light, with the efficiency of the photocatalyst increasing as Sr concentration rises, up to an optimal level [18]. The lattice defects introduced due to the ionic radius difference between Sr and Zn ions play a key role in boosting the material's photocatalytic performance, enabling more effective absorption and utilization of visible light for catalytic processes [19].

The SILAR method offers a cost-effective approach for synthesizing Sr-doped ZnO thin films, which has demonstrated significant potential in enhancing the photocatalytic properties of ZnO [20]. Although various dopants have been studied for ZnO, the specific influence of strontium doping on the photocatalytic performance and wettability of ZnO thin films remains underexplored. This study investigated the structural, optical, wettability, and photocatalytic properties of ZnO films with varying concentrations of strontium. The results showed that Sr-doped ZnO thin films, particularly those with 5 wt.% Sr, exhibited enhanced photocatalytic activity, achieving an impressive 94.82% degradation of methylene blue under sunlight. Additionally, these films demonstrated excellent stability and reusability over three cycles, emphasizing their potential for environmental applications, especially in water treatment and pollutant degradation.

III.2. Results and discussion

III.2.1.Structural properties

Figure **III.1.a** presents the XRD patterns of pure ZnO and Sr-doped ZnO films. Three prominent reflections, (100), (002), and (101), correspond to the hexagonal wurtzite structure [21,22]. Additional lower-intensity reflection peaks, (102), (110), (103), (200), (112), and (201), are observed at 46.61°, 56.66°, 62.89°, 66.49°, 68.07°, and 69.12°, respectively [23], which aligns with findings reported by Chauhan et al. [24]. The diffraction peak intensity diminishes with increasing Sr concentration. The presence of sharp and numerous diffraction peaks confirms the polycrystalline nature of the films.

The peak intensity at 31.86°, corresponding to the (100) plane, decreases when ZnO is doped with Sr, due to the larger ionic radius of Sr^{2+} (1.18 Å) compared to Zn^{2+} (0.74 Å) (Fig. III.1.c). No peaks corresponding to strontium oxide were detected across the entire doping range, indicating that the doped films maintain a pure ZnO phase [25]. The Sr^{2+} ion may not fully substitute into the ZnO crystal lattice. The shift of Sr-doped ZnO thin films towards a (100) texture orientation, instead of the typical (101) orientation, can be explained by the larger ionic radius of Sr^{2+}, which causes lattice distortion and alters crystallographic growth preferences. The incorporation of Sr^{2+} ions into the ZnO lattice increases the lattice parameters, affecting growth kinetics and energy minimization processes, thereby favoring the (100) orientation.

The XRD patterns indicate that the substitution of Sr into the ZnO lattice causes a shift in diffraction peaks due to the larger ionic radius of Sr^{2+} (1.18 Å) compared to Zn^{2+} (0.74 Å). This results in lattice distortions and promotes preferential growth along the (100) plane, consistent with observed changes in crystallographic orientations. Similar effects have been reported in studies of various materials, such as SrS alloys, Ba-Sr-Zn-Sb compounds, Sr-Mg-Sn-Zr-O ceramics, and Zn-Sn co-substituted strontium ferrite, where doping alters structural, electronic, mechanical, and optical properties, influencing lattice parameters, band gaps, and magnetic behaviors [26,27]. Furthermore, synthesis conditions, including the SILAR method and annealing temperature, play a critical role in determining the final texture of thin films, facilitating nucleation and growth along the (100) plane. This aligns with studies on dopant-induced lattice distortions that influence the preferred orientation in ZnO thin films. These findings underscore the importance of dopants and synthesis parameters in tailoring the structural properties of ZnO thin films for various applications [12,28,29]. The crystallite size for the (100) plane in Sr-doped ZnO thin films was calculated using the Debye-Scherrer formula [30]:

$$D = \frac{k\,\lambda}{\beta cos\theta} \tag{01}$$

In this calculation, β represents the full width at half maximum (FWHM) of the diffraction peak, corrected for instrumental factors, while λ = 1.5406 Å corresponds to the wavelength of the X-ray source, and k is the shape factor, typically assumed to be around 0.9. For the (100) Miller planes, the crystallite size of pure ZnO was 43.7 nm, while Sr-doped ZnO at 1, 3, 5, and 7 wt.% concentrations exhibited crystallite sizes of 55.4°, 36.2°, 55.4°, and 55.4° nm, respectively.

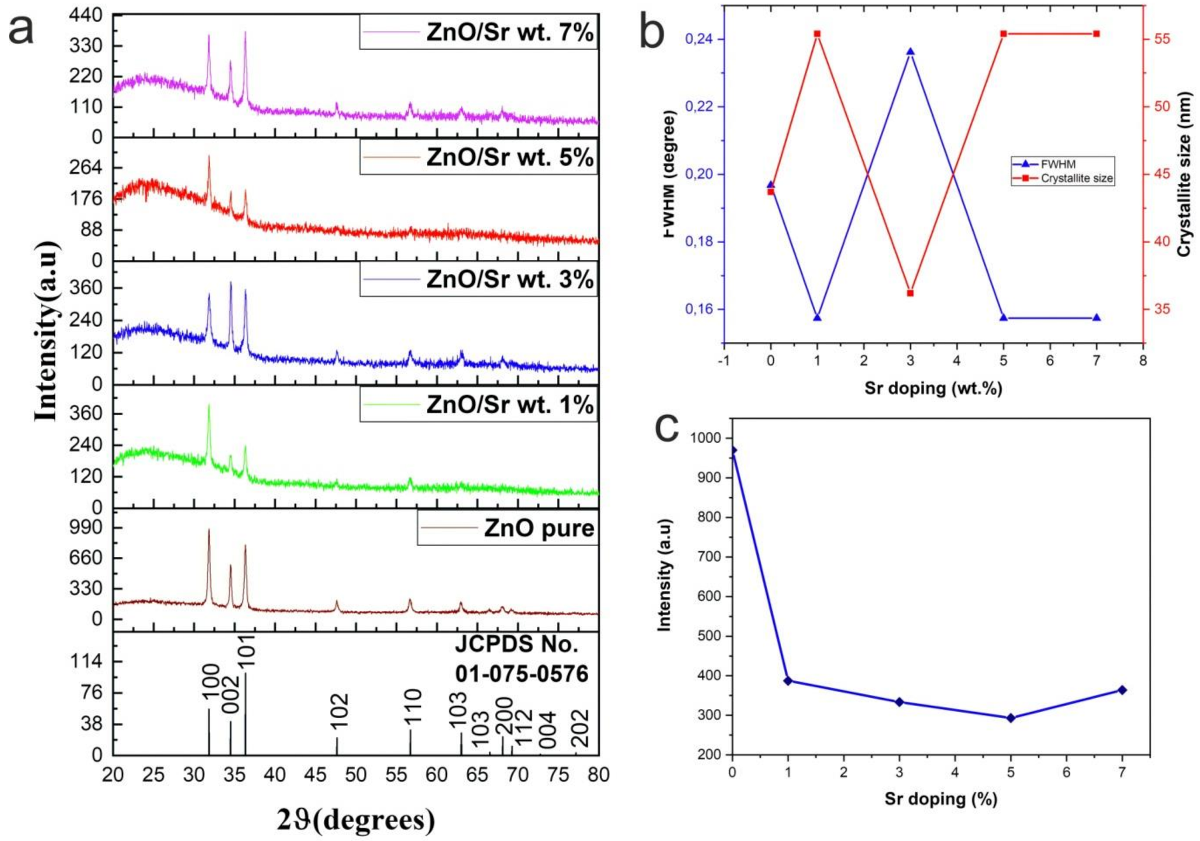

Figure III.1.(a) XRD patterns of pure and Sr-doped ZnO thin films. (**b**) FWHM of the (100) peaks and corresponding crystallite sizes. (**c**) Intensity variations of the preferred (100) peak with different Sr concentrations.

The number of crystallites (N) was determined through the use of the following equation [31]:

$$N = \frac{t}{D^3} \tag{02}$$

In this context, t represents the thickness of the film, and D denotes the size of the crystallite. Table **III.1** presents the measured values for crystallite size. Additionally, it was observed that the crystallite size increases as the concentration of Sr rises. This is attributed to a change in the nucleation process, which is influenced by the stress induced by the greater presence of Sr^{2+} in the ZnO lattice, leading to the merging of islands and the formation of larger crystallites when Sr is doped.

Table III.1. The estimated values of crystallites size, 2theta (deg), FWHM, and number of crystallites for ZnO and Sr/ZnO thin films:

Samples	*2theta(deg)*	*FWHM*	*Crystallites size (nm)*	*Number of crystallites($\times 10^{12} m^{-2}$)*
ZnO pure	31.8671	0.1968	43.7	0.8562
ZnO/Sr 1%	31.8545	0.1574	55.4	8.3281
ZnO/Sr 3%	31.8281	0.2362	36.2	1.4086
ZnO/Sr 5%	31.8543	0.1574	55.4	3.4374
ZnO/Sr 7%	31.8167	0.1574	55.4	1.4016

Figure **III.1.b** illustrates the full width at half maximum (FWHM) of the (100) plane alongside the crystallite size (D) of Sr-doped ZnO thin films. It was observed that as the Sr concentration increased from 0 wt% to 7 wt%, the maximum peak width (FWHM) decreased while the crystallite size increased from 43.7 to 55.4 nm. The return to the same larger size at 5 wt% and 7 wt% reflects that the system has reached a stable dopant incorporation threshold, where no additional stainless steel significantly affects the lattice. However, there were different findings when the FWHM increased and the crystallite size dropped to 36.2 nm. The crystallite size initially grew with up to 3% Sr doping, which was linked to lattice strain and the larger ionic radius of Sr^{2+}. After this point, the strain and defects hindered further growth, leading to smaller crystallites at higher doping concentrations. This non-linear response is due to the intricate interactions between dopant levels, lattice deformation, and the kinetics of crystallite development [15,32].

III.2.2. Wettability test

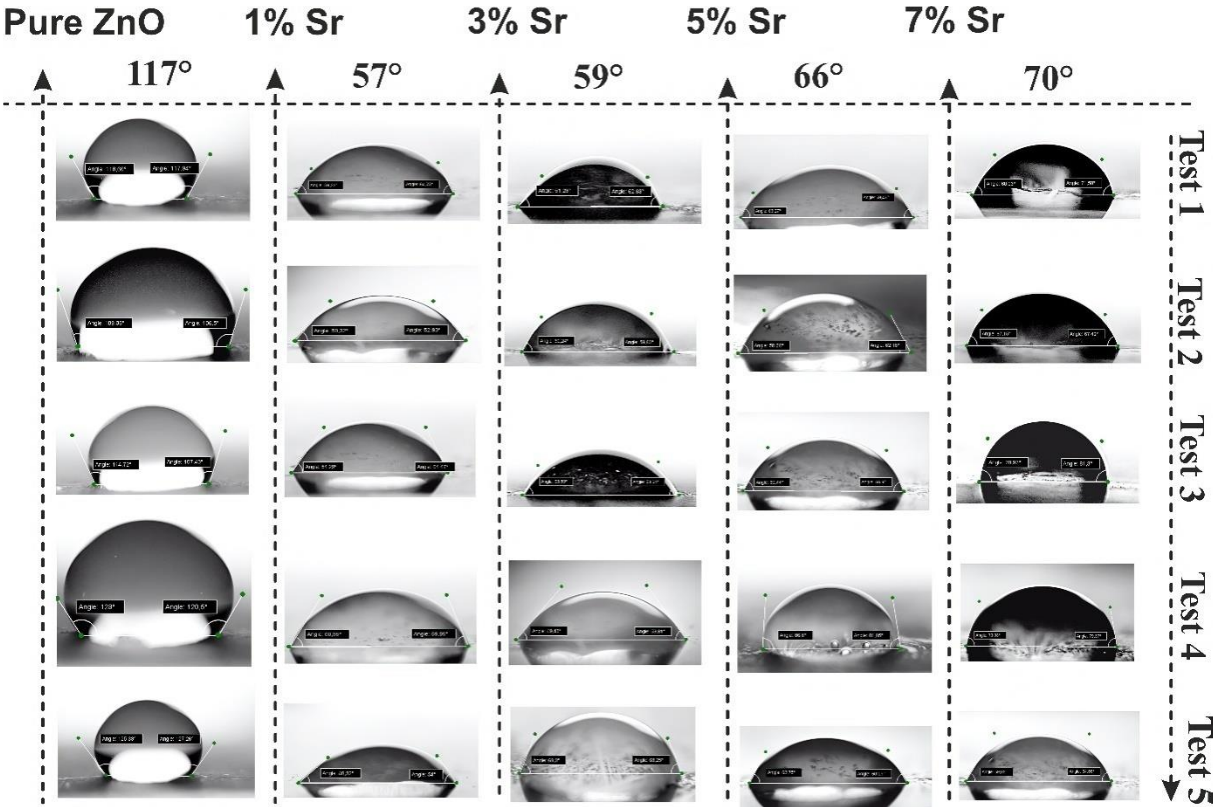

Figure III.2. Water contact angle measurements of Sr-doped ZnO thin films.

Figure **III.2** illustrates that the contact angle measurements of water on all Sr-doped ZnO thin films indicate hydrophilic surfaces. The contact angles in this study ranged from approximately 57.10° to 117.02°. The results in the table demonstrate the interplay between surface roughness, contact angle, and film thickness for thin films of zinc doped with varying concentrations of strontium. At pure ZnO, the films exhibit high roughness (Rq = 151 nm, Ra = 101 nm) and a high contact angle (117.02°), indicating a hydrophobic surface. As the strontium concentration increases to 1 wt.%, roughness rises slightly (Rq = 180 nm, Ra = 119 nm), but the contact angle significantly decreases to 57.10°, suggesting a transition toward hydrophilic behavior. At 5 wt.% Sr, a dramatic drop in roughness (Rq = 34.2 nm, Ra = 25.4 nm) is observed, paired with an increase in the contact angle (66.13°), suggesting that smoother surfaces in this range may enhance hydrophobicity. As the Sr doping concentration increases, the wettability of the film's surface improves. Enhanced hydrophilicity is critical for maximizing photocatalytic performance. Sr doping in ZnO thin films has a significant effect on surface roughness and water contact angles, both of which influence wettability [33]. At lower to moderate Sr concentrations, the increased roughness enhances hydrophilicity, leading to a noticeable decrease in contact angles. However, at higher Sr concentrations, additional roughening may slightly raise contact angles due to changes in surface morphology and the creation of new surface features [34,35]. These variations in surface roughness caused by Sr doping are linked to changes in water contact angles, emphasizing the importance of surface texture and wettability modifications. Enhanced roughness at certain doping levels results in lower contact angles, making the surface more hydrophilic, which is beneficial for applications like photocatalysis that require high wettability [23,36].The results indicate that the relationship between roughness and contact angle is influenced by the specific strontium concentration, with factors such as film morphology and thickness playing significant roles. The data suggest that while roughness can influence wettability, other parameters, including doping effects and structural changes, are critical in determining the contact angle behavior.

Table III.2. The estimated values of the root mean square (Rq), average roughness (Ra), contact angle (ϑ°), and film thickness for ZnO and Sr/ZnO thin films:

Sr Concentration (wt. %)	***Root Mean Square Rq (nm)***	***Average Roughness (Ra) (nm)***	***contact angle (ϑ°)***	***Film thickness(nm)***
0	151	101	117.02	116.97
1	180	119	57.10	145.59
3	140	108	59.51	395.07
5	34.2	25.4	66.13	239.51
7	201	119	70.30	584.47

III.2.3. 3D surface topography test

The 3D surface topography analysis was employed to examine the surface texture of the Sr-doped ZnO thin films prepared by SILAR method. Figure **III.3** presents the 3D surface topography of Sr-doped ZnO thin films on a glass substrate at various Sr concentrations. All the thin film samples exhibited a polycrystalline structure with an increase in roughness. It is well-established that the roughness of a sample also affects its wettability and the contact angle of droplets on the films. A similar pattern was observed in the study by Kirik and Șahin [37].

In image (a), the low strontium concentration shows distinct peaks, indicating enhanced crystallinity and localized growth features. In image (b), with a slight increase in strontium content, the morphology appears more uniform, suggesting a stabilization effect but reduced topographical variation. As the concentration rises to 5 wt. % in image (c), there’s a notable increase in roughness, with more pronounced features, reflecting variations in crystal growth dynamics. However, at 7 wt. % in image (d), the surface exhibits tapering peaks and increased flat areas, which may indicate a threshold where excessive doping leads to phase separation or altered growth mechanisms.

Doping ZnO thin films with strontium oxide and then calcining them at 450 °C resulted in an increase in roughness, ranging from 151 to 201 nm, depending on the Sr concentration in the samples (1, 3, 5, and 7 wt.%). The incorporation of rare earth oxide crystallites significantly increased the films' roughness [38]. Tables **III.1** and **III.2** provide the thickness and crystallite size data for the Sr/ZnO thin films with varying Sr concentrations. The thickness of the films increased from 116.97 to 584.47 nm. Raghavendra et al. [39] found that as Sr concentration in ZnO thin films increased, the projected cluster size also grew. The reduced thickness of the 5% Sr-doped ZnO sample is attributed to the larger ionic radius of Sr^{2+}, which leads to an increase in crystallite size and a decrease in surface roughness. This combination results in a denser packing of the material, producing thinner films. The incorporation of larger Sr^{2+} ions promotes crystallite coalescence and smoothens the film surface, contributing to the reduction in thickness.

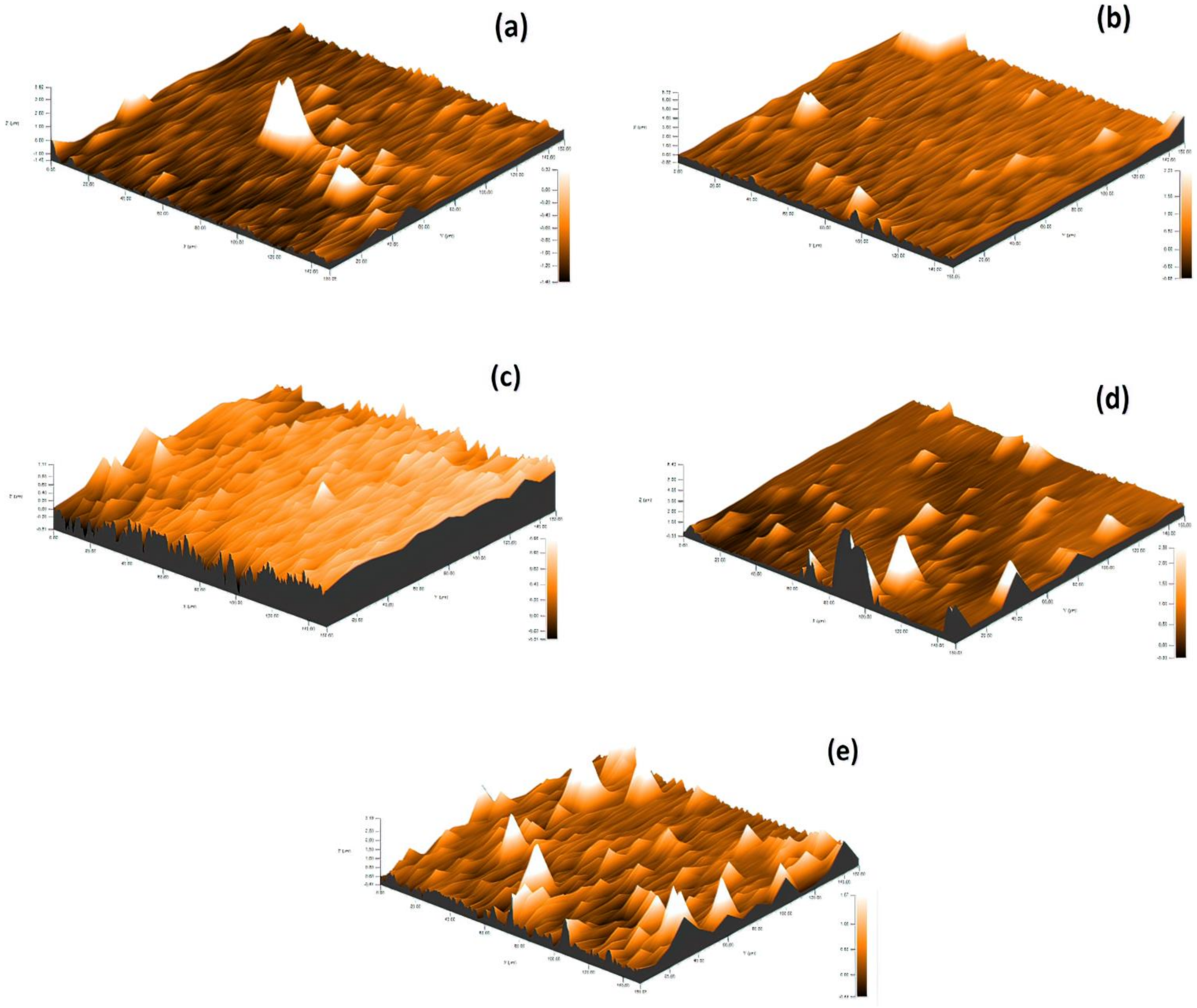

Figure III.3. 3D surface topography images of Sr-doped ZnO thin films at different concentrations (1, 3, 5, and 7 wt. %) and pure ZnO respectively (**a**), (**b**), (**c**), (**d**), and (**e**).

III.2.4. Surface morphology

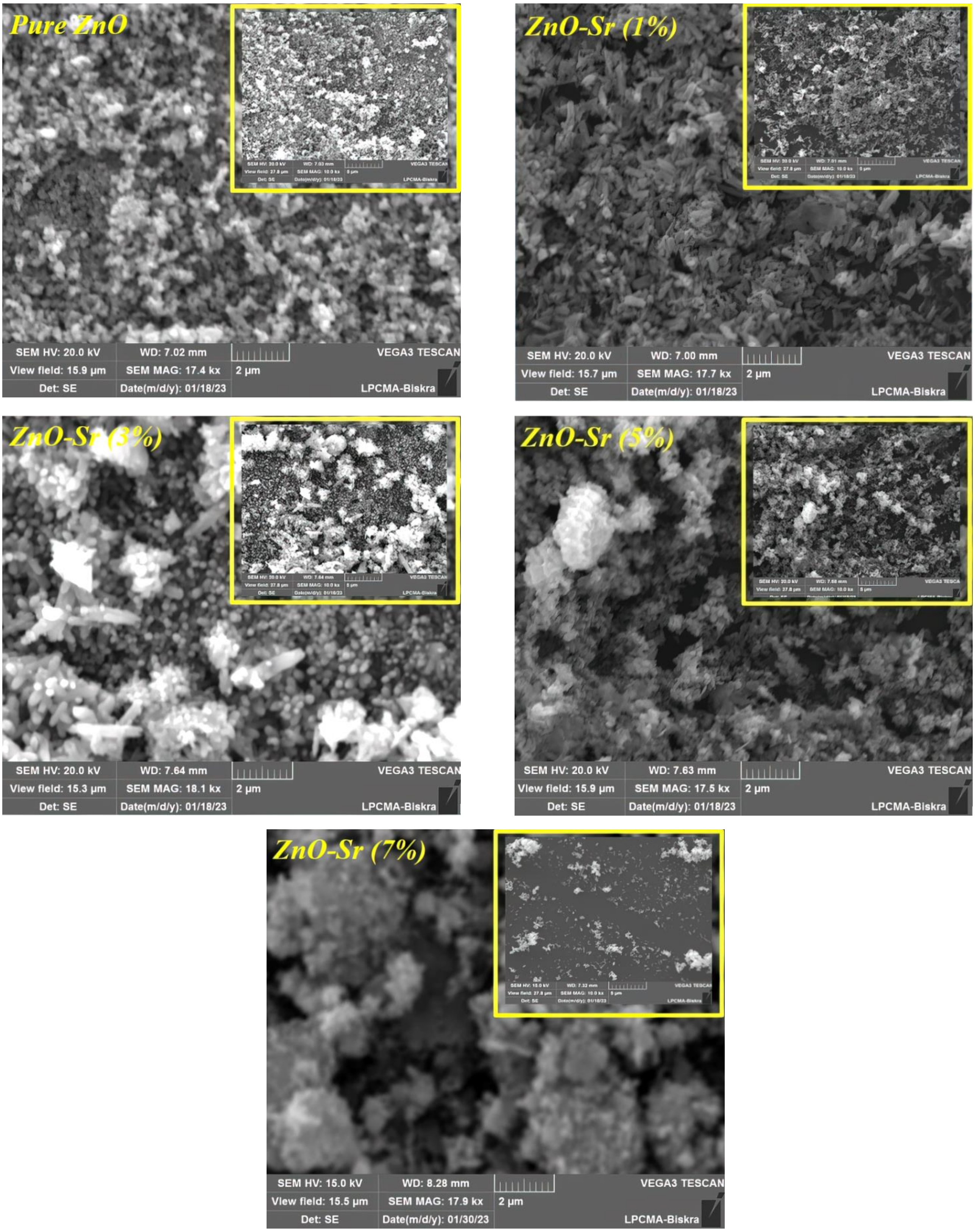

Figure III.4. SEM images of Sr-doped ZnO thin films at different concentrations (1, 3, 5, and 7 wt. %) and pure ZnO.

Figure **III.4** displays the SEM images of Sr-doped ZnO thin films, revealing changes in surface morphology with increasing Sr doping concentrations. Pure ZnO exhibits mixed, granular particles, a morphology also reported by Battal et al. [40]. In the Sr-doped ZnO (1 wt.%) sample, smaller rod-like grains are randomly distributed across the surface, exhibiting a porous structure. At 3 wt.% Sr doping, the rod grains become larger than those in the previous sample, suggesting that the doping induces coalescence of grains. With 5 wt.% doping, the morphology shows significant changes, with the formation of smoother regions and a reduction in visible porosity, consistent with the decrease in surface roughness observed in the data. Finally, at 7 wt.% Sr, the surface displays a more heterogeneous structure with large agglomerates and a rougher texture, correlating with the higher roughness values measured.

The morphological changes illustrate the effects of strontium doping on zinc oxide thin films, which can significantly influence their optical, electrical and wettability properties. The identified patterns indicate that strontium doping alters the growth dynamics of zinc oxide crystals, leading to discrepancies in grain size, distribution and surface roughness at different concentrations. This structural change is decisive for the observed changes in the contact angle and layer thickness.

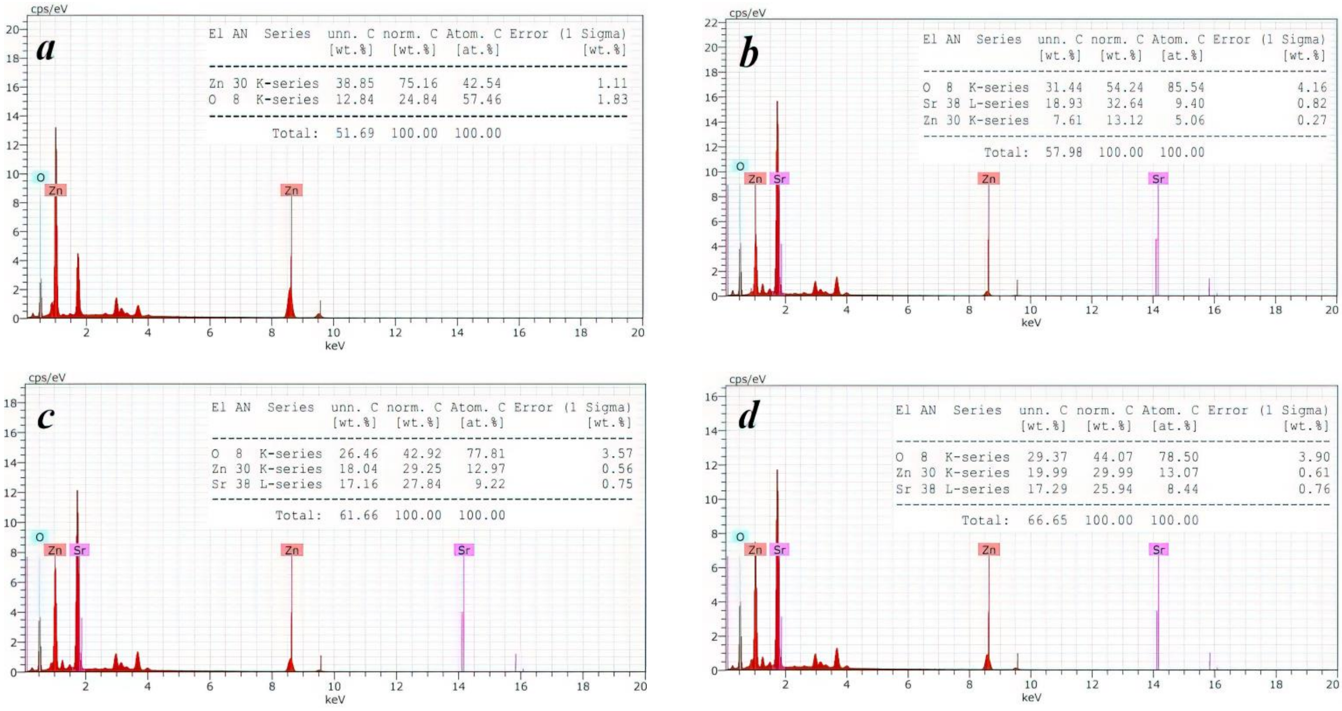

```
El AN  Series   unn. C norm. C Atom. C Error (1 Sigma)
                [wt.%]  [wt.%]  [at.%]          [wt.%]
------------------------------------------------------
Zn 30 K-series  38.85   75.16   42.54             1.11
O  8  K-series  12.84   24.84   57.46             1.83
------------------------------------------------------
        Total:  51.69  100.00  100.00
```

```
El AN  Series   unn. C norm. C Atom. C Error (1 Sigma)
                [wt.%]  [wt.%]  [at.%]          [wt.%]
------------------------------------------------------
O  8  K-series  31.44   54.24   85.54             4.16
Sr 38 L-series  18.93   32.64    9.40             0.82
Zn 30 K-series   7.61   13.12    5.06             0.27
------------------------------------------------------
        Total:  57.98  100.00  100.00
```

```
El AN  Series   unn. C norm. C Atom. C Error (1 Sigma)
                [wt.%]  [wt.%]  [at.%]          [wt.%]
------------------------------------------------------
O  8  K-series  26.46   42.92   77.81             3.57
Zn 30 K-series  18.04   29.25   12.97             0.56
Sr 38 L-series  17.16   27.84    9.22             0.75
------------------------------------------------------
        Total:  61.66  100.00  100.00
```

```
El AN  Series   unn. C norm. C Atom. C Error (1 Sigma)
                [wt.%]  [wt.%]  [at.%]          [wt.%]
------------------------------------------------------
O  8  K-series  29.37   44.07   78.50             3.90
Zn 30 K-series  19.99   29.99   13.07             0.61
Sr 38 L-series  17.29   25.94    8.44             0.76
------------------------------------------------------
        Total:  66.65  100.00  100.00
```

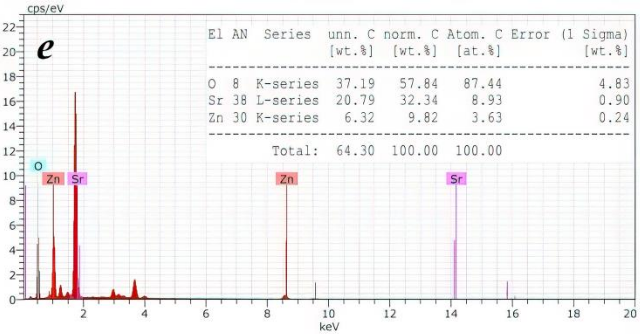

```
El AN  Series   unn. C norm. C Atom. C Error (1 Sigma)
                [wt.%]  [wt.%]  [at.%]          [wt.%]
------------------------------------------------------
O  8  K-series  37.19   57.84   87.44             4.83
Sr 38 L-series  20.79   32.34    8.93             0.90
Zn 30 K-series   6.32    9.82    3.63             0.24
------------------------------------------------------
        Total:  64.30  100.00  100.00
```

Figure III.5. EDS spectrum of Sr-doped ZnO thin films at (**a**) Pure ZnO, (**b**) 1, (**c**) 3, (**d**) 5, and (**e**) 7 wt.%.

The EDS spectra in Figure **III.5** provide a detailed chemical analysis of pure ZnO and Sr-doped ZnO thin films with strontium concentrations of 1, 3, 5, and 7 wt.%. For pure ZnO (a), the spectrum primarily shows strong peaks for zinc (Zn) and oxygen (O), confirming the composition of the undoped ZnO. With the introduction of 1 wt.% Sr (b), a small peak corresponding to strontium appears, indicating successful incorporation of Sr into the ZnO matrix, while Zn and O remain dominant. When the strontium concentration increases to 3 wt% (c) and 5 wt% (d), the amount of strontium increases proportionally, confirming the increased presence of strontium in the film. At 7 wt% strontium (e), the amount of strontium becomes clearer in the quantum ratio table, confirming the validity of stepwise activation. The consistent presence of zinc and oxygen peaks in all samples indicates that the basic ZnO structure is preserved despite the incorporation of strontium. In contrast, Figures III.5.(b-e) confirm that the Sr-doped ZnO samples consist exclusively of Zn, O, and Sr, with no impurities detected, affirming the purity of the synthesized thin films.

III.2.5. Optical properties

The impact of Sr concentration on the optical properties of ZnO thin films was investigated. Figure **III.6** presents the optical transmittance spectra of the films as a function of Sr concentration within the wavelength range of 200–1200 nm. The pure ZnO film has an average visible transmittance of 20%, whereas the transmittance of Sr-doped samples increases across the entire visible spectrum.

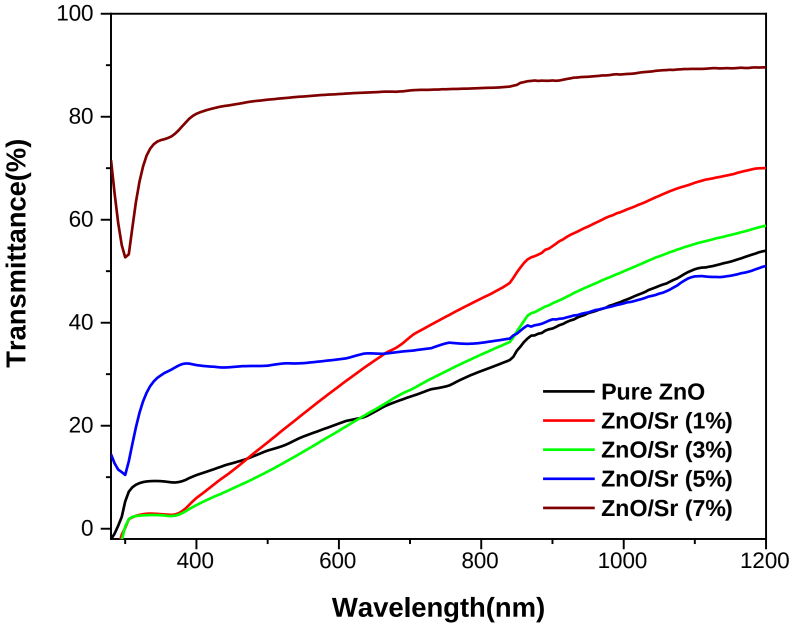

Figure III.6. UV-Vis absorption spectra of ZnO and Sr-doped ZnO thin films.

The transmittance spectra of thin ZnO slices doped with different concentrations of Sr, prepared via the SILAR method, reveal a systematic decrease in transmittance with increasing Sr content. Pure ZnO exhibits transmittance across the visible and near-infrared (NIR) regions, indicative of its high optical clarity and low defect density. As Sr doping increases, the transmittance diminishes, particularly for 1%, 3% and 5% Sr concentrations. This reduction can be attributed to the introduction of lattice distortions and defect states caused by the substitution of Sr for Zn, as Sr has a larger ionic radius. These defects act as scattering centers and increase light absorption through sub-band-gap transitions. Furthermore, higher Sr doping concentrations may induce a redshift in the optical absorption edge due to band gap narrowing, further decreasing transmittance in the visible range. Among the coated films, the ZnO film doped with 7 wt.% Sr exhibits the highest optical transmittance. The enhanced transmittance observed after metal doping may result from increased photon scattering caused by crystal defects, as noted in previous research [41]. These changes highlight the impact of Sr doping on the optical properties of ZnO, showing a trade-off between transmittance and potential functional enhancements, such as photocatalytic activity, at higher doping levels.

The optical bandgap (Eg) of the deposited thin films was calculated using the Tauc formula [42]:

$$(\alpha hv) = A(hv - Eg)^n \tag{03}$$

Where hv represents the photon energy, A is a constant independent of energy, and n depends on the type of semiconductor, with n=1/2 for indirect bandgaps and n=2 for direct bandgaps. The reported optical bandgap values were 3.18 eV for the pure ZnO film and 3.12, 3.06, 3.16, and 3.02 eV for Sr-doped ZnO thin films synthesized at 1, 3, 5, and 7 wt.%, respectively. Studies by Vijayan et al. [21], Ouhaibi et al. [43], and Ali et al. [44] have shown that the bandgap energy values increase slightly with higher Sr concentrations. For doping levels well below the critical Mott density, the optical bandgap shift can be attributed to the Burstein-Moss effect, bandgap broadening, and narrowing due to electron-electron and electron-impurity scattering. Sr-doped ZnO thin films exhibited wider bandgaps compared to pure ZnO. This widening and the associated blue shift caused by doping make Sr-doped ZnO nanoparticles highly suitable for various engineering applications, including their use in optoelectronics as UV-absorbing layers and UV-shielding devices.

The bandgap reduction observed at 5 wt.% Sr doping in Sr-doped ZnO thin films correlates with the largest crystallite size and the smallest film thickness at this doping level. A larger crystallite size enhances photocatalytic properties by increasing the generation of electron-hole pairs, which contributes to the bandgap reduction. This reduction is significant for improving photocatalytic efficiency, as it promotes the formation of oxygen vacancies that further enhance the material's photocatalytic performance [45,46].

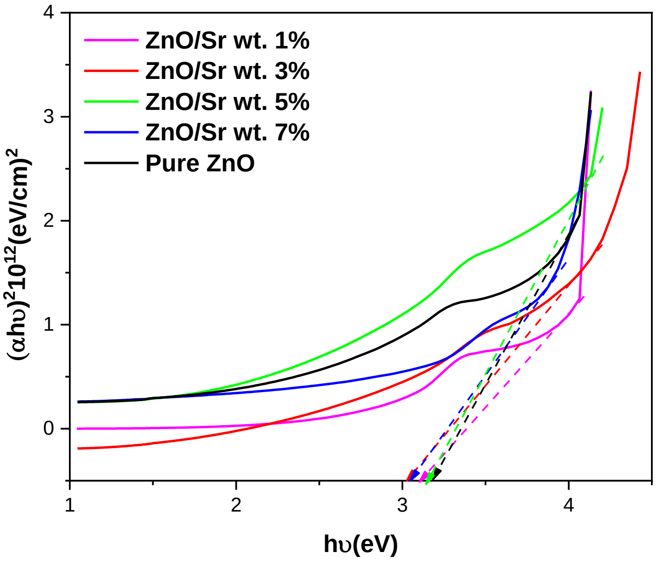

Figure III.7. Tauc plots for determining the optical band gap of the films.

III.2.6. Photocatalytic test

Figure **III.8.c**(1, 2, 3, 4, and 5) displays the absorption spectra of MB dye degraded under visible light irradiation for 4 hours at a pH of 7 using the pure ZnO and Sr-doped ZnO thin films. The results show that the characteristic peak intensities of MB dye decrease as the irradiation time increases. According to Table **III.3**, the η value for pure ZnO after 4 hours is 73.74%. Additionally, the intensity of the MB absorption peak at 663 nm diminishes with prolonged irradiation time. The photocatalytic activity against MB dye improved significantly to 94.82% with the incorporation of 5 wt.% Sr doping (**Fig III.9a**) [47].

Table III.3. Photocatalytic degradation efficiency, band gap (Eg), and pseudo-first-order rate constant (k) for ZnO and Sr/ZnO thin films:

Samples	***Efficiency ‘η’ (%) Cycle 1***	***Efficiency ‘η’ (%) Cycle 2***	***Efficiency ‘η’ (%) Cycle 3***	***Band gap (Eg) (eV)***	***K (hr^{-1})***	***R^2***
Pure ZnO	73.74	-	-	3.18	0.316	0.961
ZnO/Sr 1%	82.17	-	-	3.12	0.441	0.986
ZnO/Sr 3%	81.92	-	-	3.06	0.405	0.967
ZnO/Sr 5%	94.82	94.61	93.48	3.16	0.742	0.987
ZnO/Sr 7%	63.63	-	-	3.02	0.266	0.954

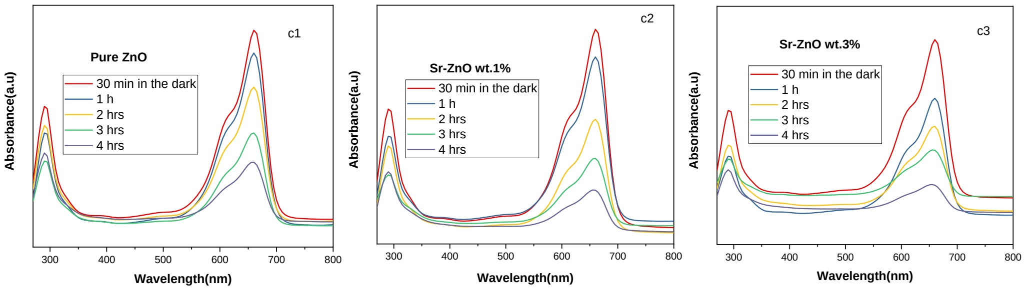

Figure III.8.c (**1**, **2**, **3**, **4**, and **5**) the absorbance of MB for all films.

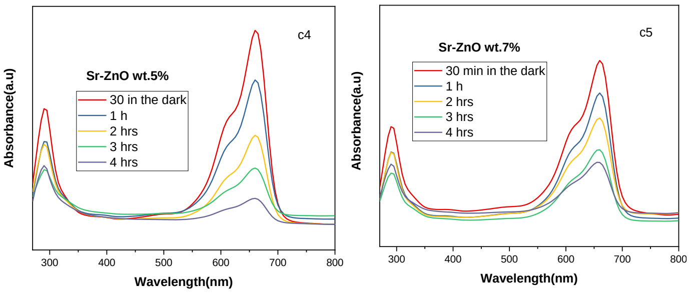

Figure III.8.c (**1**, **2**, **3**, **4**, and **5**) the absorbance of MB for all films.

Photogenerated charges are independently transported to the catalytic surfaces. Electrons combine with oxygen molecules to form superoxide anions ($O_2^{\bullet -}$), while light-induced holes (*h*+) lead to the generation of hydroxyl radicals ($OH^\bullet$). In the solution, electrons and holes interact to produce highly oxidizing species, including hydroxyl ($OH^\bullet$) and hydroperoxyl radicals. The resulting degradation products are described by the following equations [48]:

$$e_{CB}^{-} + Sr^{2+} \rightarrow Sr^{(2-1)+} \tag{04}$$

$$O_2 + Sr^{(2-1)+} \rightarrow O_2^{\bullet -} + Sr^{2+} \tag{05}$$

$$ZnO + h_{VB} + OH^{-} \rightarrow ZnO + OH^{\bullet} \tag{06}$$

$$OH^{\bullet} \rightarrow degradation\ products + CO_2 + H_2O \tag{07}$$

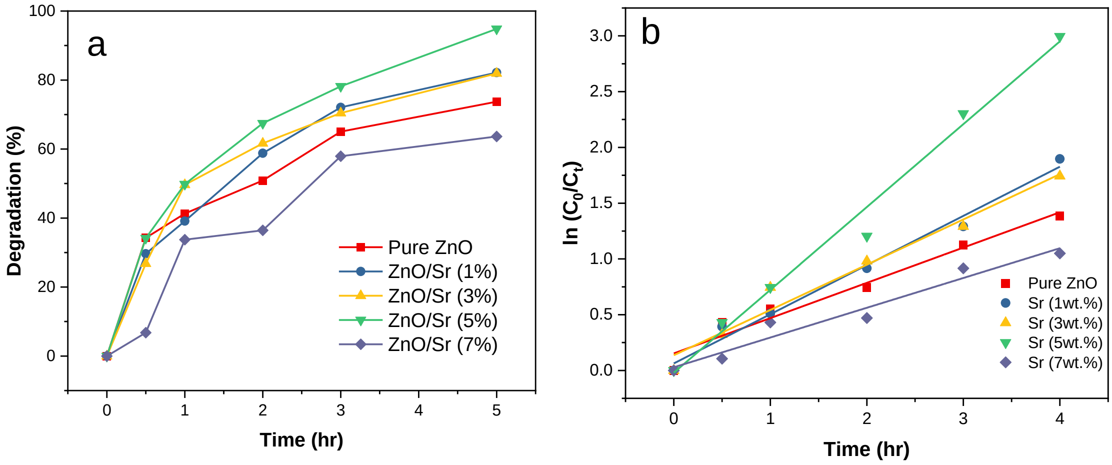

Figure III.9.(**a**) Photodegradation of MB under visible light irradiation for pure ZnO and Sr-doped ZnO, (**b**) kinetics of samples for the degradation of MB under visible light irradiation.

The figure **III.9b** illustrates the chemical reaction kinetics of methylene blue photocatalysis using thin films of zinc oxide doped with varying concentrations of strontium (1, 3, 5, and 7 wt.%) prepared via the SILAR method. The photocatalytic degradation kinetics of ZnO and Sr-doped ZnO were analyzed using the pseudo-first-order kinetic model described by Langmuir–Hinshelwood, expressed as follows [49]:

$$k = \frac{\ln(C_0/C_t)}{t} \qquad (08)$$

where, C_0 represents the initial concentration, C_t is the concentration at time t, and k denotes the pseudo-first-order rate constant. Notably, the slope of the lines increases with increasing strontium doping concentration, indicating a faster degradation rate. This enhancement in photocatalytic activity is likely attributed to the improved charge separation and reduced electron-hole recombination in the presence of strontium dopants, which act as electron traps, facilitating the transfer of photogenerated electrons to the surface of the catalyst for the reduction of oxygen to superoxide radicals. Table **III.3** provides the estimated parameters, including the pseudo-first-order rate constant K and the R^2 values. The proposed model demonstrated strong compatibility, with a high coefficient of determination (R^2>0.95). The K values for the ZnO and Sr-doped ZnO thin films (1, 3, 5, and 7 wt.%) were 0.316, 0.441, 0.405, 0.742, and 0.266 h^{-1} , respectively. The reduction in the bandgap to 3.02 eV at a 5 wt.% doping level is attributed to the largest crystallite size and thinnest film thickness at this concentration. This lower bandgap improves photocatalytic efficiency by promoting the generation of electron-hole pairs and enhancing visible light absorption [49,50]. Furthermore, the reduced bandgap increases oxygen vacancies, which aids in charge separation and minimizes recombination rates, thereby enhancing photocatalytic performance [51]. As a result, the 5 wt.% Sr-doped ZnO sample exhibits the highest photocatalytic efficiency, achieving an impressive 94.82% degradation rate of methylene blue under visible light irradiation. This demonstrates the importance of optimal doping levels in enhancing the photocatalytic properties of ZnO-based materials (**Fig III.9a**).

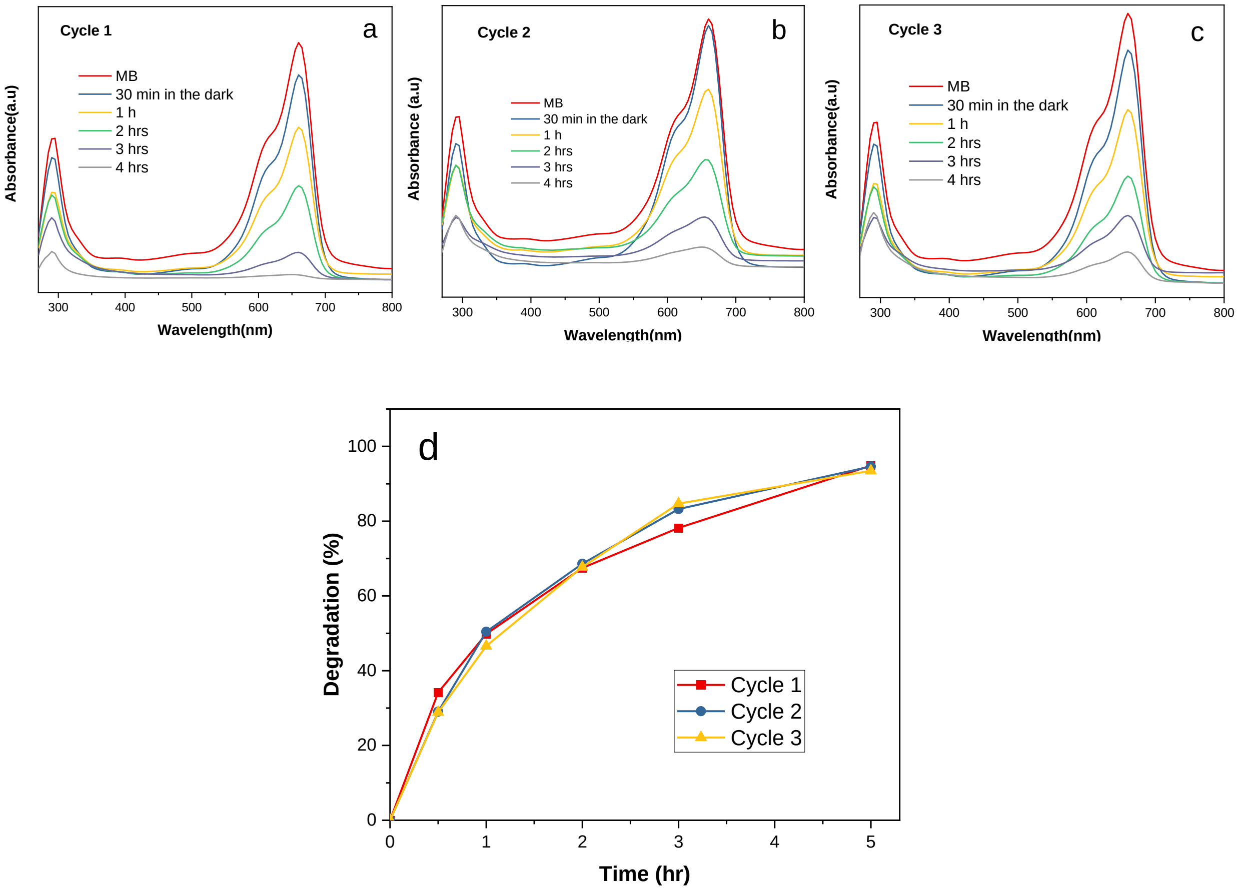

Figure III.10. The recyclability of the 5wt. % Sr for degradation of MB in (**a**) 1st cycle, (**b**) 2nd cycle, (**c**) 3rd cycle, and (**d**) the recycling efficiency of the 5 wt. % Sr.

In addition to photocatalytic activity, recyclability is a vital factor for the commercial applicability of photocatalysts [52]. The 5 wt.% Sr thin film was recycled three times under similar reaction conditions (**Fig III.10a-c**). Figure **III.10d** illustrates that after recycling, the photocatalytic efficiency for MB degradation of the 5 wt.% Sr films remains stable, with about 99% of the initial photocatalytic efficiency retained (**Fig III.9a**). In the first cycle, a rapid increase in degradation efficiency is observed, reaching over 90% within 4 hours, indicating strong photocatalytic activity. The second and third cycles show similar trends with marginal reductions in efficiency, suggesting excellent stability and recyclability of the material. The slight decrease in degradation efficiency in subsequent cycles may be due to minor surface fouling or the accumulation of reaction by products that partially block active sites. However, the material retains a high recycling efficiency, highlighting its potential for repeated use in wastewater treatment applications. The consistent performance underscores the stability of the Sr-doped ZnO structure and its suitability as a robust photocatalyst.

Table III.4. Comparison of the photocatalytic efficiency of Sr/ZnO thin film for MB degradation with literature studies:

Catalyst	***Dye***	***Fabrication method***	***Removal Efficiency (%)***	***Reaction Time (min)***	***Light Source***	***Ref***
ZnO	Methylene blue	SILAR	90.91	240	Sunlight	[43]
Ag/ZnO	Methylene blue	Spray pyrolysis	83	180	UV	[52]
Ni/ZnO	Rhodamine B	Spray pyrolysis	60.24	90	UV	[53]
Ba/ZnO	Rhodamine B	Sol-gel	82%	50	UV	[54]
Cd/ZnO	Methylene blue	SILAR	82.5	180	UV	[48]
Mg/ZnO	Methylene blue	Sol-gel	70	300	UV	[55]
Sr/ZnO	Methylene blue	SILAR	94.82	240	sunlight	Current study

A comparison of the efficiency of various catalysts in degrading methylene blue (MB) and other dyes highlights the influence of different fabrication methods, irradiation sources, and reaction times on photocatalytic performance (**Table III.4**) [43, 48, 52,55]. For example, Ba/ZnO synthesized using the sol-gel method achieved 82% degradation of Rhodamine B in 50 minutes under UV light [54], while Ni/ZnO prepared by spray pyrolysis showed a 60.24% degradation efficiency for Rhodamine B in 90 minutes under UV light [53]. In contrast, Sr-doped ZnO demonstrated superior performance with 94.82% degradation of methylene blue over 240 minutes under sunlight irradiation. The enhanced efficiency of Sr-doped ZnO is attributed to its increased surface area, more active sites, and improved charge separation, reduced recombination of electron-hole pairs, and lower band gap, which enables better visible light absorption for enhanced photocatalytic activity. These results highlight the importance of fabrication methods and doping in improving the photocatalytic properties of ZnO-based materials and suggest that optimizing these factors can significantly enhance dye degradation efficiency.

III.3. Conclusion

In this chapter, pure ZnO and Sr-doped ZnO thin films were synthesized using the SILAR method and thoroughly characterized to understand their structural, optical, wettability, and photocatalytic properties. The results demonstrated that doping ZnO with Sr led to significant improvements in material properties, particularly in enhancing photocatalytic efficiency and stability. The X-ray diffraction (XRD) analysis revealed that all films retained a polycrystalline hexagonal wurtzite structure. The incorporation of Sr ions, due to their larger ionic radius compared to Zn^{2+}, induced lattice distortions and promoted preferential growth along the (100) crystallographic plane. These structural modifications were critical in improving the material's optical and photocatalytic performance.

The surface morphology of the films, studied using SEM and 3D surface topography, showed significant changes with varying Sr concentrations. The addition of Sr enhanced the surface roughness and altered the grain structure, contributing to improved hydrophilicity. Water contact angle measurements confirmed that Sr doping reduced the contact angle from a hydrophobic 117.02° for pure ZnO to as low as 57.10° for 1 wt.% Sr-doped ZnO. These results underscore the role of Sr in optimizing surface properties to facilitate applications requiring high wettability, such as photocatalysis.

The optical analysis revealed a systematic narrowing of the bandgap with increasing Sr concentration, from 3.18 eV for pure ZnO to 3.02 eV for the 5 wt.% Sr-doped ZnO. This bandgap reduction enhanced the absorption of visible light, improving the material’s photocatalytic efficiency under sunlight. The 5 wt.% Sr-doped ZnO thin film achieved the highest photocatalytic degradation efficiency, breaking down 94.82% of methylene blue (MB) dye within four hours. Furthermore, the recyclability tests showed that the photocatalytic activity remained stable over three consecutive cycles, with minimal loss in efficiency, demonstrating excellent durability and reusability.

The findings highlight the transformative effect of Sr doping on ZnO thin films, enabling them to address environmental challenges such as water pollution through efficient and sustainable photocatalytic processes. The optimized doping level of 5 wt.% Sr emerged as the most effective concentration, balancing structural, optical, and catalytic properties. These results not only advance the understanding of Sr-doped ZnO materials but also emphasize their potential for real-world applications, including wastewater treatment, pollutant degradation, and other photocatalysis-based environmental solutions.

References of chapter III

[1] Borges, M. E., et al. "Photocatalytic Removal of Water Emerging Pollutants in an Optimized Packed Bed Photoreactor Using Solar Light." *Catalysts* 13.6 (2023): 1023.

[2] Ghaffar, Sadia, et al. "Improved photocatalytic and antioxidant activity of olive fruit extract-mediated ZnO nanoparticles." *Antioxidants* 12.6 (2023): 1201.

[3] Modi, Shreya, et al. "Photocatalytic degradation of methylene blue dye from wastewater by using doped zinc oxide nanoparticles." *water* 15.12 (2023): 2275.

[4] Ranjbari, Alireza, et al. "Effect of oxygen vacancy modification of ZnO on photocatalytic degradation of methyl orange: A kinetic study." *Catalysis Today* 427 (2024): 114413.

[5] Daher, Elie A., et al. "Design of a new ZnO photocatalytic Fenton-like system for enhancing the removal of methylene blue at neutral pH." *Ceramics International* 50.12 (2024): 20843-20850.

[6] Ghosh, Amrita, and Anup Mondal. "Fabrication of stable, efficient and recyclable p-CuO/n-ZnO thin film heterojunction for visible light driven photocatalytic degradation of organic dyes." *Materials Letters* 164 (2016): 221-224.

[7] Malekkiani, Mitra, et al. "Facile fabrication of ternary MWCNTs/ZnO/Chitosan nanocomposite for enhanced photocatalytic degradation of methylene blue and antibacterial activity." *Scientific Reports* 12.1 (2022): 5927.

[8] Temam, Elhachmi Guettaf, et al. "Photocatalytic activity of Al/Ni doped TiO2 films synthesized by sol-gel method: Dependence on thickness and crystal growth of photocatalysts." *Surfaces and Interfaces* 31 (2022): 102077.

[9] Mekkaoui, Amer, et al. "A new study on the effect of pure anatase TiO2 film thickness on gentian violet photodegradation under sunlight: considering the effect of hole scavengers." *Trends in Sciences* 20.1 (2023): 3766-3766.

[10] Yilmaz, Mehmet, NurtacCanpolat, and SakirAydoğan. "Surface plasmon resonance effects of Ag@ ZnO core–shell nanostructure in UV and visible light for photodiode applications." *Journal of the American Ceramic Society* 107.5 (2024): 3390-3402.

[11] Yılmaz, Mehmet, et al. "Photodiode behavior and capacitive performance of ZnO nanoflakes synthesized by electrochemical deposition." *Journal of Physics D: Applied Physics* 56.49 (2023): 495109.

[12] Sithole, J., et al. "Simonkolleite nano-platelets: synthesis and temperature effect on hydrogen gas sensing properties." *Applied surface science* 258.20 (2012): 7839-7843.

[13] Althamthami, Mohammed, et al. "Improved photocatalytic activity under the sunlight of high transparent hydrophilic Bi-doped TiO2 thin-films." *Journal of Photochemistry and Photobiology A: Chemistry* 443 (2023): 114818.

[14] Althamthami, Mohammed, et al. "Influence of hole-scavenger and different withdrawn speeds on photocatalytic activity of Co3O4 thin films under sunlight irradiation." *Ceramics International* 48.21 (2022): 31570-31578.

[15] Yousefi, Ramin, et al. "Enhanced visible-light photocatalytic activity of strontium-doped zinc oxide nanoparticles." *Materials Science in semiconductor processing* 32 (2015): 152-159.

[16] Althamthami, Mohammed, et al. "Effect of different Cu: Co film concentrations on photocatalytic reactions of ethanol, MB, AMX, and Cr (VI): A study of film properties & effects of photooxidation." *Journal of Environmental Chemical Engineering* 11.6 (2023): 111247.

[17] Tursucu, A., et al. "Investigation the performance of Cr-doped ZnO nanocrystalline thin film in photodiode applications." *Jom* 74.3 (2022): 777-786.

[18] Kumar, D. Ranjith, YuvarajHaldorai, and RT Rajendra Kumar. "Rare Earth Metals Doped ZnO Nanomaterials: Synthesis, Photocatalytic, and Magnetic Properties." *Rare Earth: A tribute to the late Mr. Rare Earth, Professor Karl Gschneidner* 164 (2024): 279-297.

[19] AlMohamadi, Hamad, et al. "Photocatalytic activity of metal-and non-metal-anchored ZnO and TiO2 nanocatalysts for advanced photocatalysis: comparative study." *Catalysts* 14.7 (2024): 420.

[20] Vijayan, T. A., et al. "Comparative investigation on nanocrystal structure, optical, and electrical properties of ZnO and Sr-doped ZnO thin films using chemical bath deposition method." *Journal of Materials Science* 43.6 (2008): 1776-1782.

[21] Raj, K. Pradeev, et al. "Structural, optical, photoluminescence and photocatalytic assessment of Sr-doped ZnO nanoparticles." *Materials Chemistry and Physics* 183 (2016): 24-36.

[22] Mansouri, I., et al. "Effect of Sr-doping toward the optoelectrical ZnO properties." *Inorganic Chemistry Communications* 162 (2024): 112236.

[23] Ouhaibi, A., et al. "The effect of strontium doping on structural and morphological properties of ZnO nanofilms synthesized by ultrasonic spray pyrolysis method." *Journal of Science: Advanced Materials and Devices* 3.1 (2018): 29-36.

[24] Chauhan, Asha, A. K. Shrivastav, and Anjali Oudhia. "Synthesis and characterization of ambient-processed FTO/ZnO/CsPbBr2Cl/C perovskite solar cell deposited by SILAR method." *Optical Materials* 130 (2022): 112575.

[25] Akshata, G., and Santhosha Acharya. "Synthesis and characterization of undoped and strontium doped ZnO thin films." *Materials Today: Proceedings* 55 (2022): 109-112.

[26] Serradj, Fares, et al. "Unveiling the impact of Cd and Zn substitutions on the structural, mechanical, electronic, and optical properties of SrS: a first principles analysis." *Physica B: Condensed Matter* 689 (2024): 416204.

[27] Hamidani, Ali, BadisBennecer, and Kamel Zanat. "Effect of Sr substitution on the structural, electronic and thermoelectric properties of the Zintl-phase compound BaZn 2 Sb 2." *Physica Scripta* 98.6 (2023): 065910.

[28] Anas, Muhammad, et al. "Influence of Zirconium (Zr4+) Substitution on the Crystal Structure and Optical and Dielectric Properties of Sr0. 8Mg0. 2 (Sn1–x Zr x) O3 Ceramics." *ACS omega* 8.37 (2023): 33794-33801.

[29] Verma, Swati, et al. "Study of Zn-Zr dopant induced phase changes in strontium hexaferrite using Rietveld refinement and their physical properties." *Materials Today: Proceedings* (2023).

[30] Kaviyarasu, K., et al. "Well-aligned graphene oxide nanosheets decorated with zinc oxide nanocrystals for high performance photocatalytic application." *International Journal of Nanoscience* 14.03 (2015): 1550007.

[31] Sathyamoorthy, R., and J. Dheepa. "Structural characterization of thermally evaporated Bi2Te3 thin films." *Journal of Physics and Chemistry of Solids* 68.1 (2007): 111-117.

[32] Thema, F. T., et al. "Green synthesis of ZnO nanoparticles via Agathosmabetulina natural extract." *Materials Letters* 161 (2015): 124-127.

[33] Saadi, Boutheina, SaâdRahmane, and Elhachmi Guettaf Temam. "Structural, optical and electrical properties of spray deposited indium-doped Cr2O3 thin films." *Journal of Optics* 53.1 (2024): 582-589.

[34] Raghavendra, P. V., J. S. Bhat, and N. G. Deshpande. "Enhancement of photoluminescence in Sr doped ZnO thin films prepared by spray pyrolysis." *Materials Science in Semiconductor Processing* 68 (2017): 262-269.

[35] Welegergs, G. G., et al. "Spectrally selective single layered Ag@ CuOnanocermet coatings for photothermal application: green synthesis method." *Optical Materials* 135 (2023): 113247.

[36] Ngom, B. D., et al. "Structural and optical properties of nano-structured tungsten-doped ZnO thin films grown by pulsed laser deposition." *Applied Surface Science* 255.7 (2009): 4153-4158.

[37] Maaza, Malik, et al. "Induced structural damages by He+ irradiation in conducting transparent indium–tin oxide thin films." *Solar energy materials and solar cells* 90.1 (2006): 111-119.

[38] Manikandan, A., et al. "Rare earth element (REE) lanthanum doped zinc oxide (La: ZnO) nanomaterials: synthesis structural optical and antibacterial studies." *Journal of Alloys and Compounds* 723 (2017): 1155-1161.

[39] Soltanian, Asma, et al. "Correlation between the optical and microstructural characteristics and surface wettability transition of In2O3: Sn/ZnO nanostructured bilayer system for self-cleaning application." *Physica Scripta* 98.7 (2023): 075912.

[40] Kirik, Nurdan Selin, and BünyaminŞahin. "Characteristics modification of ZnO/CuO composite films by doping rare-earth element Dy for real-time hydration level monitoring." *Micro and Nanostructures* 167 (2022): 207290.

[41] Tański, Tomasz, et al. "Hydrophilic ZnO thin films doped with ytterbium and europium oxide." *Scientific Reports* 12.1 (2022): 11329.

[42] Battal, W., et al. "Strontium doping effect on characteristics of ultrasonically sprayed zinc oxide thin films." *Applied Physics A* 126 (2020): 1-10.

[43] Santhamoorthy, Aishwarya, et al. "SILAR-deposited nanostructured ZnO thin films: effect of deposition cycles on surface properties." *Bulletin of Materials Science* 44.3 (2021): 188.

[44] Ali, Shah Raj, et al. "Effect of Strontium Doping on the Band Gap of CeO _ 2 CeO 2 Nanoparticles Synthesized Using Facile Co-precipitation." *Arabian Journal for Science and Engineering* 44 (2019): 6295-6302.

[45] Maaza, Malek, et al. "Peculiar size effects in nanoscaled systems." *Nano-Horizons: Journal of Nanosciences and Nanotechnologies* 1 (2022): 36-pages.

[46] Ravichandran, K., et al. "Intermediate electron trap levels generation and enhanced carrier concentration in ZnO by strontium and molybdenum co-doping: an effective approach for dye degradation." *Journal of Materials Science: Materials in Electronics* 34.1 (2023): 5.

[47] Sanakousar, F. M., et al. "Recent progress on visible-light-driven metal and non-metal doped ZnO nanostructures for photocatalytic degradation of organic pollutants." *Materials science in semiconductor processing* 140 (2022): 106390.

[48] Sathya, M., et al. "Synthesis and characterization of cadmium doped on ZnO thin films prepared by SILAR method for photocatalytic degradation properties of MB under UV irradiation." *The European Physical Journal Plus* 138.1 (2023): 1-12.

[49] Ismail, E., M. Kenfouch, and M. Dhlamini. "Green biosynthesis of rhodium nanoparticles via Aspalathus linearis natural extract." *J Nanomater Mol Nanotechnol* of 7 (2017): 2.

[50] Sajjad, Shamaila, et al. "Fe3O4 nanorods r-GO sheets nanocomposite visible photo catalyst." *Materials Research Express* 6.6 (2019): 065013.

[51] Mehra, Sonali, et al. "Development of visible light-driven SrTiO3 photocatalysts for the degradation of organic pollutants for waste-water treatment: Contrasting behavior of MB & MO dyes." *Optical Materials* 136 (2023): 113344.

[52] Sutanto, Heri, et al. "Ag doped ZnO thin films synthesized by spray coating technique for methylene blue photodegradation under UV irradiation." *International Journal of Chemical Engineering* 2016.1 (2016): 6195326.

[53] Sellam, Manel, et al. "Degradation of rhodamine B dye under visible and solar light on zinc oxide and nickel-doped zinc oxide thin films." *Optical Materials* 151 (2024): 115316.

[54] Shirdel, Behnaz, and Mohammad A. Behnajady. "Sol-gel synthesis of Ba-doped ZnO nanoparticles with enhanced photocatalytic activity in degrading Rhodamine B under UV-A irradiation." *Optik* 147 (2017): 143-150.

[55] Islam, Muhammad R., and Muhammad G. Azam. "Enhanced photocatalytic activity of Mg-doped ZnO thin films prepared by sol–gel method." *Surface Engineering* 37.6 (2021): 775-783.

Chapter IV:

Impact of High Strontium Concentrations on the Structure of Zinc Thin Films and Their Application in Degrading Methylene Blue and Rose Bengal

This chapter is based on: Mokrani Nourelhouda, et al. "Enhancing water purification with light-activated strontium-doped ZnO thin films." *Advances in Natural Sciences: Nanoscience and Nanotechnology* 16.1 (2025): 015012.

IV.1. Introduction

Water pollution has become a widespread issue, largely driven by industrial advancement and societal growth [1,2]. Achieving a clean and sustainable environment remains a critical global goal [3,4]. In response, researchers are actively pursuing eco-friendly strategies to remediate contaminated air, water, and soil [5]. However, many existing methods for dye removal face significant challenges, such as incomplete contaminant elimination, complex processes, high operational costs, and the potential for secondary pollution [6,7]. Semiconductors present a promising alternative due to their efficiency, affordability, and non-toxic nature, particularly in photocatalysis a process that harnesses light to drive chemical reactions [7,8].

Zinc Oxide (ZnO) has recently gained recognition as a highly versatile material, with applications spanning solar cells [9], varistors [10], gas sensors [11], biomedicine [12], photodiodes [13], electrochemical sensors [14], and UV photodetectors [15]. ZnO is also an effective photocatalyst for purifying air and water, as well as for surface cleaning applications [15,16]. Its widespread appeal stems from its high photosensitivity, environmental compatibility, stability, affordability, excellent photocatalytic efficiency, and ability to harness abundant solar radiation, along with its exceptional physical and chemical properties [17].

A key area of research focuses on enhancing ZnO's ability to absorb visible light, a critical factor in improving its photocatalytic performance [18]. Doping ZnO with elements such as carbonaceous materials and rare earth metals extends its light absorption range, enhancing its photocatalytic properties [19,20]. These doping studies are considered essential for deepening the understanding of ZnO thin films' physical properties and accelerating their industrial applications [21].

Additionally, noble metal nanoparticles can modify the optical properties of semiconductors via surface plasmon resonance, expanding their absorption spectrum from the UV into the visible light range [22]. Coupled oxide systems (COS) have also demonstrated potential by reducing electron-hole recombination, thereby increasing photocatalytic activity [11]. Among rare earth metals, strontium (Sr) has been studied as a promising dopant for ZnO, as it can enhance properties critical to applications such as photocatalysis [23,24], gas sensing [25], love wave filters [19], and photovoltaics [23].

Photocatalysis is widely recognized as one of the most advanced techniques for mitigating rust formation, garnering significant attention for its sustainable approach to addressing critical challenges such as water splitting, photochemical degradation of waste products, and the purification of gaseous pollutants [26]. The substantial volume of scientific publications—exceeding a thousand annually—dedicated to photocatalysis and oxide/semiconductor materials highlights the importance of this research domain [27,28].

In particular, there is considerable interest in ZnO-Sr composites for enhancing photocatalytic performance. Sr-doped ZnO offers a cost-effective alternative to expensive Indium Tin Oxide (ITO) thin films, benefiting from zinc's abundance, low cost, and comparable optical and electrical properties. Moreover, Sr-doped ZnO coatings demonstrate exceptional transparency and low resistivity [29].

Ongoing research continues to explore the potential of doping ZnO with various elements to expand its functional properties [30]. For example, Akshata et al. reported that Sr-doped ZnO thin films exhibited improved light transmittance and a reduced band gap compared to pure ZnO, further underscoring its potential for practical applications [29].

Recent studies on transition metal-doped ZnO (TM-doped ZnO) have primarily utilized chemical solution methods, including sol-gel [31], spray pyrolysis [32], chemical bath deposition [33], and successive ionic layer adsorption and reaction (SILAR) techniques. Among these, SILAR technology stands out as a particularly appealing method for producing thin films due to its cost-effectiveness, straightforward deposition protocols, enhanced formulation control, and environmentally friendly nature [34]. These advantages make SILAR a compelling choice for the large-scale fabrication of ZnO thin films [35].

This research demonstrates the successful synthesis of Sr-coupled ZnO thin films using the SILAR technique, highlighting its simplicity, affordability, and effectiveness. A novel aspect of this study is the production of thin films with high concentrations of strontium doping. The photocatalytic efficiency of these films will be evaluated through the degradation of methylene blue (MB) and rose bengal (RB) under natural sunlight. Furthermore, the study will investigate the degradation of methylene blue in the presence of hole scavengers and varying solution acidity to assess the films' effectiveness under different conditions.

IV.2. Results and discussion

IV.2.1. XRD analysis

The X-ray diffraction (XRD) patterns of pure ZnO and Sr-coupled ZnO heterostructures with varying weight ratios of nanocrystalline ZnO to Sr are illustrated in Figure **IV.1a**. The diffraction peaks of the pure ZnO sample align with the standard reference pattern for wurtzite ZnO (JCPDS No. 01-075-0576). Similarly, the hybrid samples exhibit identical diffraction peaks at 2θ values of 31.8°, 34.3°, 36.3°, 47.6°, 56.6°, 62.9°, 67.9°, and 69.1°, corresponding to the (100), (002), (101), (102), (110), (103), (103), and (200) lattice planes of wurtzite ZnO, respectively. Notably, regardless of the Sr doping concentration, the coupled films display diffraction peaks that are consistent with those of pure ZnO.

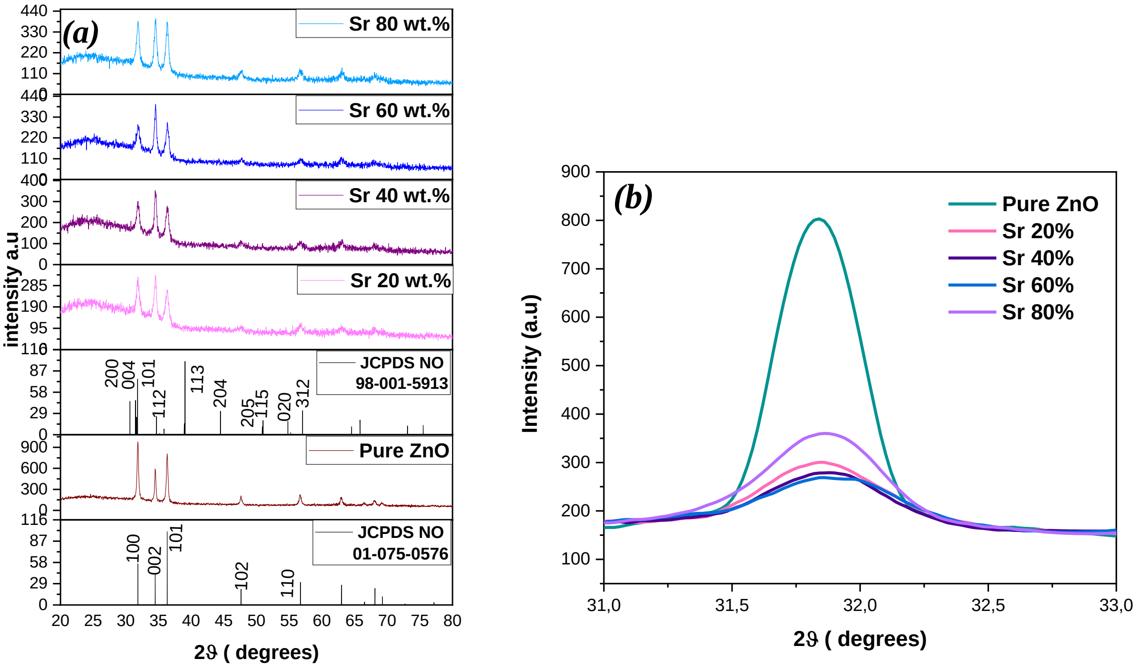

Figure IV.1. (**a**) XRD patterns of deposited thin films; (**b**) Enlarged view of Sr concentration-dependent shift in the position of peaks due to (100) plane along 2ϑ axis.

The XRD patterns of all Sr-coupled ZnO samples revealed distinct peaks that were slightly shifted toward lower angles compared to the undoped ZnO sample. Despite varying coupling concentrations, the coupled films exhibited peaks similar to those of pure ZnO. The ZnO film exhibited preferential crystallographic growth along the (100) plane. However, this preferential orientation changed in all the Sr-coupled samples [36]. The incorporation of Sr impurities introduced a prominent reflection at 2θ = 34.54°, corresponding to the (112) plane of $SrZnO_2$ (PDF, 98–001–5913). Sr-coupled films demonstrated a preferential crystal orientation along the (112) plane, consistent with previous studies [37,38]. Additionally, the intensity of the diffraction peaks decreased following Sr coupling, with a notable reduction in the intensity of the (100) peak, as depicted in Figure **IV.1b**. Similar findings have been reported by Rajan et al. [29]. The crystallite size (D) was calculated using the Scherrer equation [39,40]:

$$Crystallite\ size\ D = \frac{0.9\lambda}{\beta cos\vartheta} \qquad (01)$$

where, λ represents the wavelength of the X-ray radiation used (CuKα1), β denotes the full width at half maximum (FWHM) of the diffraction peak, and ϑ is the diffraction angle. The dislocation density (d) for the most prominent ZnO peak, corresponding to the (100) plane, can be calculated using the following relation [41]:

$$\delta = \frac{1}{D^2} \qquad (02)$$

The lattice parameters "c" and "a" corresponding to the most intense peak of ZnO (100) are determined as follows:

$$\mathrm{c} = \frac{\lambda}{Sin\ \vartheta} \qquad (03)$$

$$\mathrm{a} = \frac{\lambda}{\sqrt{3}Sin\vartheta} \qquad (04)$$

The lattice parameters a and c are fundamental structural constants that define the dimensions of a crystal's unit cell in the hexagonal wurtzite structure of ZnO. These parameters are directly related to the atomic arrangement and bonding within the crystal lattice. The parameter c corresponds to the height of the unit cell along the crystallographic c-axis. Similarly, the parameter a defines the in-plane dimensions perpendicular to the c-axis. These lattice parameters provide insights into the crystal structure, degree of strain, and the effects of coupling or other modifications on the material.

Table IV.1. The estimated values of crystallites size, hkl, 2theta, FWHM, number of crystallites, lattice parameters and dislocation density for ZnO and Sr-coupled ZnO thin films.

		Pure ZnO	*Sr 20%*	*Sr40%*	*Sr 60%*	*Sr 80%*
2theta(deg)		31.86	31.89	31.81	31.80	31.89
hkl		100	100	100	100	100
FWHM		0.196	0.346	0.189	0.130	0.149
Crystallites size (nm)		43.7	23.9	43.7	63.5	55.5
Number of crystallites ($\times 10^{12} m^{-2}$)		2.512	38.145	5.084	1.325	1.983
Lattice parameters(A°)	***a=b***	3.242	3.34	3.35	3.34	3.34
	c	5.176	5.83	5.84	5.83	5.83
Dislocation density($\times 10^{-3}$ nm) δ		0.52	1.7	0.52	0.24	0.32

The values are presented in Table **IV.1**, revealing that the crystallite size ranges between 23.9 and 63.5 nm. The highest texture coefficient is observed for the (100) diffraction plane of the pure ZnO phase, consistent with findings reported by Al Hassan et al. [35] and Al Farsi et al. [17]. The broadening of diffraction peaks serves as an indicator for estimating the crystallite size within the material. A comparison of peak widths between the doped and pure ZnO samples indicates that strontium coupling at higher concentrations (60% and 80%) result in smaller crystallite sizes compared to pure ZnO or samples with lower coupling levels (20% and 40%). This observation suggests that Sr coupling influences the crystalline structure. As shown in Table **IV.1**, the preferential growth orientation of the heterostructure films is along the (100) plane for both ZnO and Sr-coupled ZnO. The incorporation of Sr introduces lattice strain into the ZnO crystal, likely due to the ionic size disparity between Zn and Sr, which impact the preferred orientation of crystallites.

A slight shift in the diffraction peaks to higher angles was observed following the incorporation of strontium, as reflected in the changes in lattice parameters (**Fig IV.1b**). As the concentration of strontium increases, the diffraction peaks shift progressively toward lower diffraction angles, which can be attributed to the substitution of Sr^{2+} ions (ionic radius: 118 pm) in place of Zn^{2+} ions (ionic radius: 74 pm). This substitution results in noticeable lattice distortion within the Sr-ZnO lattice, primarily due to the elongation of SrZn-O bonds

[42]. The introduction of strontium doping alters the lattice parameters of ZnO, which is directly related to the disparity in ionic radius between Sr^{2+} and Zn^{2+}. It was observed that the lattice parameters of Sr-coupled ZnO were slightly larger than those of undoped ZnO. This variation in lattice parameters contributes to intra-grain coupling within the metal oxide, promoting stronger interactions between the composite metal oxides and playing a vital role in enhancing the photocatalytic activity of the synthesized materials.

IV.2.2. SEM analysis

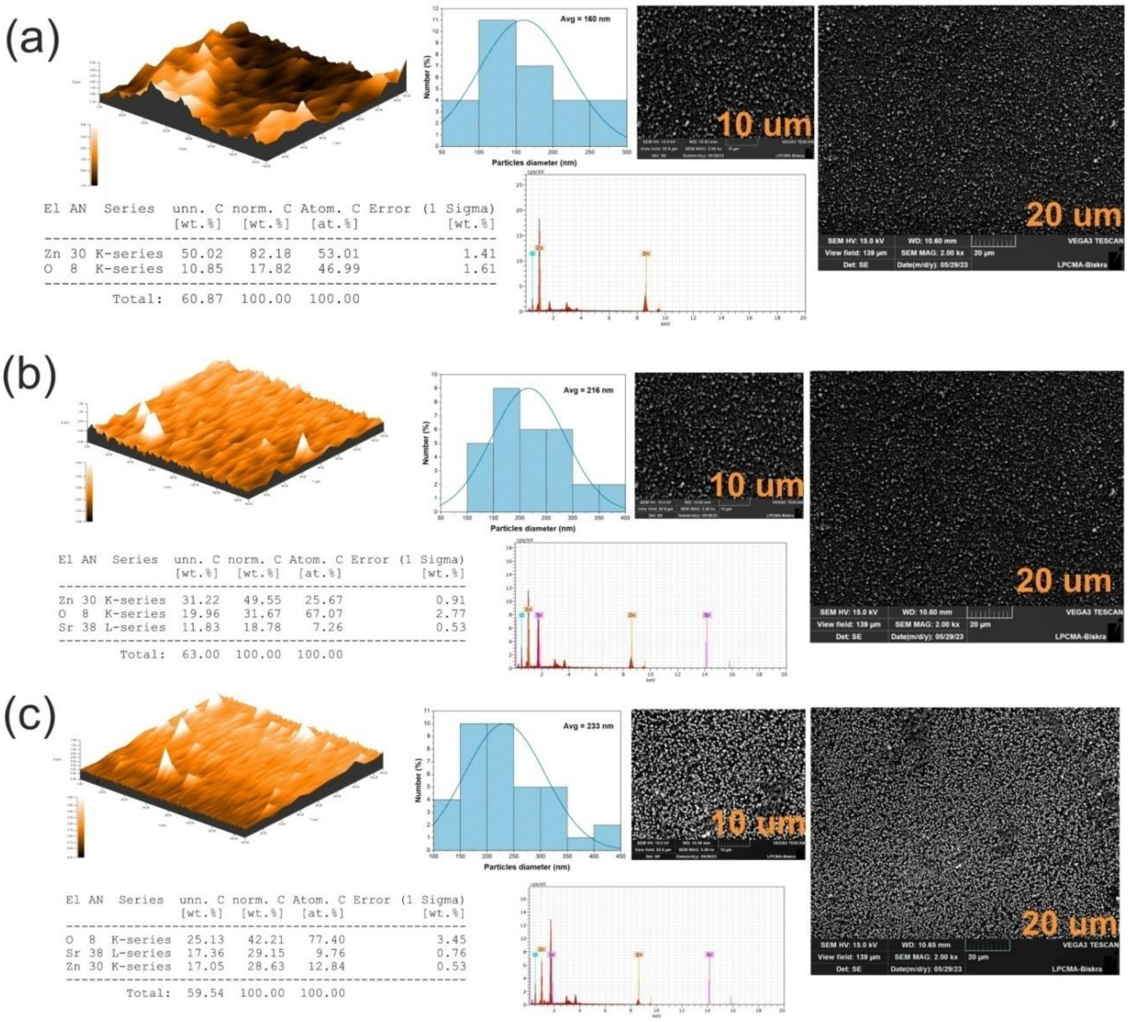

```
El AN  Series   unn. C norm. C Atom. C Error (1 Sigma)
                [wt.%]  [wt.%]  [at.%]           [wt.%]
-------------------------------------------------------
Zn 30 K-series  50.02   82.18   53.01              1.41
O  8  K-series  10.85   17.82   46.99              1.61
-------------------------------------------------------
        Total:  60.87  100.00  100.00
```

```
El AN  Series   unn. C norm. C Atom. C Error (1 Sigma)
                [wt.%]  [wt.%]  [at.%]           [wt.%]
-------------------------------------------------------
Zn 30 K-series  31.22   49.55   25.67              0.91
O  8  K-series  19.96   31.67   67.07              2.77
Sr 38 L-series  11.83   18.78    7.26              0.53
-------------------------------------------------------
        Total:  63.00  100.00  100.00
```

```
El AN  Series   unn. C norm. C Atom. C Error (1 Sigma)
                [wt.%]  [wt.%]  [at.%]           [wt.%]
-------------------------------------------------------
O  8  K-series  25.13   42.21   77.40              3.45
Sr 38 L-series  17.36   29.15    9.76              0.76
Zn 30 K-series  17.05   28.63   12.84              0.53
-------------------------------------------------------
        Total:  59.54  100.00  100.00
```

Figure IV.2. 3D surface topography images, EDS spectrum, SEM, and particles diametre of pure ZnO and Sr-coupled ZnO composite films deposited on glass substrates for different concentrations of (0, 20, 40, 60, and 80 wt. %) respectively (**a**), (**b**), (**c**), (**d**), and (**e**).

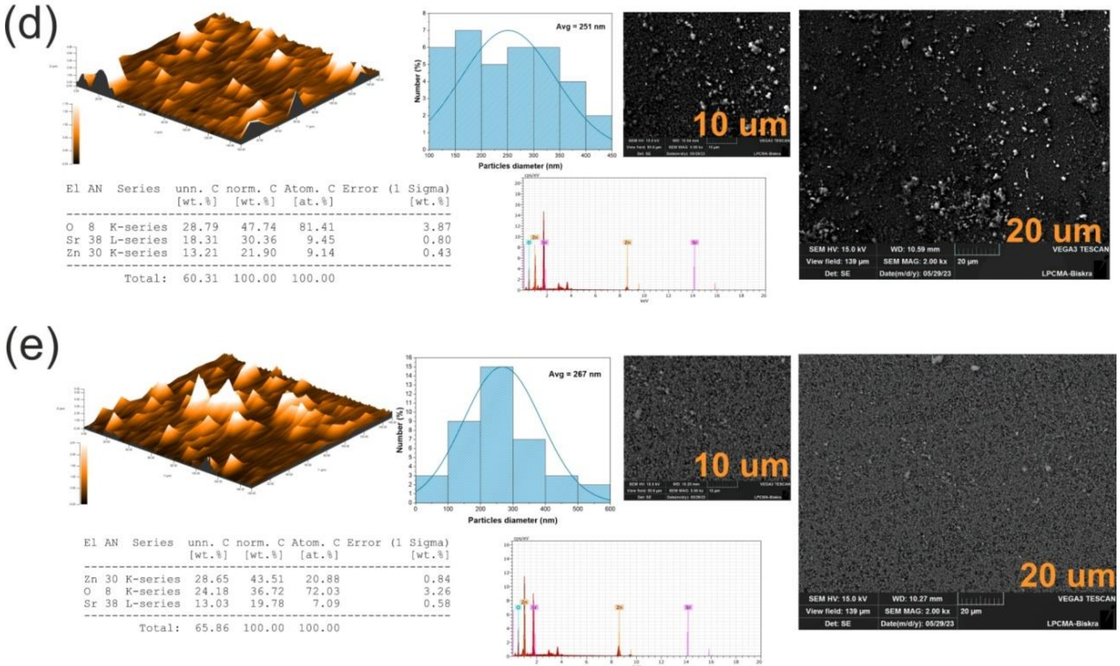

```
El AN  Series  unn. C norm. C Atom. C Error (1 Sigma)
               [wt.%]  [wt.%]  [at.%]           [wt.%]
-----------------------------------------------------
O   8  K-series  28.79   47.74   81.41             3.87
Sr 38  L-series  18.31   30.36    9.45             0.80
Zn 30  K-series  13.21   21.90    9.14             0.43
-----------------------------------------------------
        Total:   60.31  100.00  100.00
```

```
El AN  Series  unn. C norm. C Atom. C Error (1 Sigma)
               [wt.%]  [wt.%]  [at.%]           [wt.%]
-----------------------------------------------------
Zn 30  K-series  28.65   43.51   20.88             0.84
O   8  K-series  24.18   36.72   72.03             3.26
Sr 38  L-series  13.03   19.78    7.09             0.58
-----------------------------------------------------
        Total:   65.86  100.00  100.00
```

Figure IV.2. 3D surface topography images, EDS spectrum, SEM, and particles diametre of pure ZnO and Sr-coupled ZnO composite films deposited on glass substrates for different concentrations of (0, 20, 40, 60, and 80 wt. %) respectively (**a**), (**b**), (**c**), (**d**), and (**e**).

Scanning electron microscopy (SEM) was utilized to analyze the surface characteristics and morphology of the synthesized samples, providing insights into the growth mechanism, particle shape, and dimensions, as these factors significantly influence catalytic performance. The SEM micrographs presented in figure **IV.2** illustrate the microstructure of the composite materials. All thin films demonstrate a high density with uniform grain distribution across the substrate, free from any visible cracks [43,44]. In the absence of Sr^{2+} ions, the ZnO surface exhibits a smooth morphology, with well-aligned, densely packed hexagonal nanorods. In contrast, the Sr-coupled ZnO thin films feature small spherical structures and clusters of varying sizes and shapes [35]. As shown in figure **IV.2**, increasing the Sr concentration results in larger particle sizes, reaching up to 267 nm for sample E (Sr 80%) (**Fig IV.2e**). Additionally, samples (d, e) reveal the formation of a core-shell structure [45]. Pure ZnO films (**Fig IV.2a**), on the other hand, display smaller particle sizes, measuring approximately 160 nm. The observed increase in particle size with higher Sr concentrations can be attributed to the effect of Sr coupling on ZnO grain growth.

It is well known that grain sizes measured by SEM are typically larger than crystallite sizes determined from XRD analysis. This difference arises because grains represent aggregates of crystals oriented in the same direction [46]. Unlike SEM, which provides a distribution of nanoparticle diameters, XRD measures the average size of crystalline domains within the sample. This average does not necessarily correspond to the actual nanoparticle size, as it does not account for size distributions or variations in particle types [47]. Theoretically, the average crystallite size could reflect two distinct sample types with uniform sizes or result from a wide distribution of particle sizes. If the sample contains amorphous material, it is unlikely that all particles are single crystals. Consequently, the measured crystallite size would likely be biased toward smaller values compared to the nanoparticle diameters [48].

The EDS spectra and corresponding tables presented in Figure **IV.2** provide a detailed analysis of the elemental composition of the pure ZnO and Sr-coupled ZnO thin films at varying strontium concentrations (0, 20, 40, 60, and 80 wt.%). These results confirm the successful incorporation of Sr into the ZnO matrix. For the pure ZnO sample (a), the EDS data predominantly reveal the presence of zinc and oxygen, with no evidence of strontium. As the Sr concentration increases (b to e), the spectra display progressively higher Sr peaks, accompanied by a reduction in the relative Zn and O signals, indicating a systematic doping process.

The quantitative analysis in the tables highlights the weight and atomic percentages of Zn, O, and Sr. The increasing Sr content corresponds to the expected enhancement in Sr weight percentage across the samples. Notably, the composition ratios align with the nominal doping levels, showcasing the uniformity and precision of the fabrication process.

IV.2.3. Surface Roughness

Table IV.2. 3D surface topography analysis: surface roughness (R_a, R_q) and surface shape (R_{sk}, R_{ku}), Contact angle (ϑ°), and Film thickness parameters for Sr-coupled ZnO thin films.

	Sr Concentration (wt. %)				
Parameters	***0%***	***20%***	***40%***	***60%***	***80%***
R_a (nm)	168	71	49.5	115	107
R_q (nm)	216	86.9	67.8	160	148
R_{sk}	4.69	0.0265	-1.10	1.26	1.36
R_{ku}	3.20	2.62	7.12	6.23	6.68
Contact angle(ϑ°)	119.45	135.91	129.02	137.90	139.18
Film thickness(nm)	209.69	520.75	424.33	339.46	339.10

Table **IV.2** presents the Ra and Rq values, which represent the average roughness and root mean square roughness, respectively. The results show a notable decrease in both Ra and Rq values with strontium coupling levels of up to 40%, indicating that the ZnO films become smoother as Sr is incorporated at these concentrations. However, at higher doping levels of 60% and 80%, the roughness values increase again, suggesting that there is an optimal Sr concentration (40%) for achieving the smoothest surface morphology.

Additionally, the surface slope (R_{sk}) values provide insights into the spatial distribution of surface features. A positive R_{sk} value indicates a surface dominated by peaks, while a negative value suggests a prevalence of valleys. The pure ZnO film exhibits the highest positive R_{sk} value, signifying a surface with more peaks. Interestingly, the ZnO film coupled with 40% Sr displays a negative R_{sk} value, indicating a shift in surface morphology characterized by an increased presence of valleys. The R_{sk} values for other coupling concentrations follow different trends, highlighting the effect of Sr coupling on the topography of ZnO films.

The film thickness exhibits an unusual trend of decreasing as the strontium concentration increases [49]. This behavior can be attributed to several factors, including variations in the deposition rate during the growth process due to Sr incorporation. The inclusion of larger Sr cations in place of Zn cations can result in the formation of vacancies or distortions within the crystal lattice, thereby affecting the film's density. Furthermore, studies indicate that the deposition method employed (SILAR) encounters certain limitations at higher Sr concentrations. These challenges include difficulties in achieving uniform precursor adsorption or the initiation of uncontrolled nucleation processes, both of which arise from changes in surface chemistry caused by Sr coupling. Understanding and addressing these factors is essential for optimizing the deposition process to produce films with the desired properties for photocatalytic applications. Incorporating Sr has been identified as an effective strategy to enhance surface chemistry.

IV.2.4. Contact angle measurement

As illustrated in Figure **IV.4**, the contact angle of the thin film surfaces was measured using the droplet method to evaluate their wettability. A water droplet with a volume of approximately 10 µL was dispensed slowly onto the thin film surface using a micropipette (SCILOGEX, ISO 9001/13485). After allowing the droplet to stabilize on the surface for about seven seconds, an image of the droplet was captured from a precise horizontal angle. The captured images were then processed using IC Measure software to determine the contact angles. Each contact angle was measured three times at different surface locations, and the final value was obtained by calculating the arithmetic mean of these measurements.

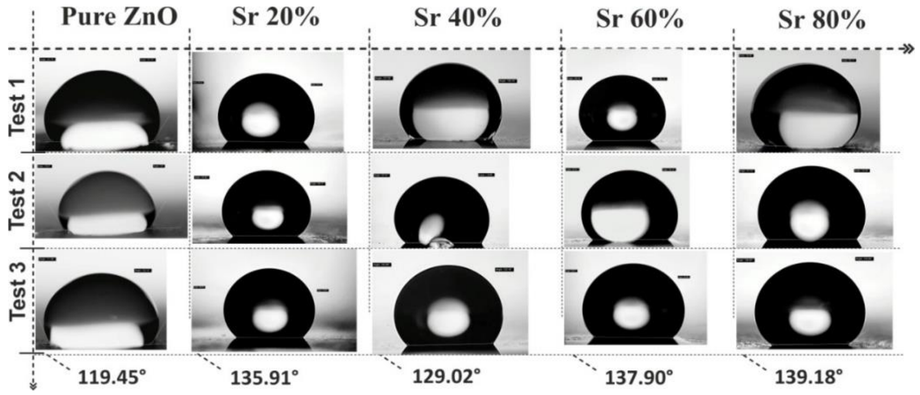

Figure IV.3. Contact angle measurement images of Sr-coupled ZnO thin films at 3 different test sites.

The contact angle measurements presented in Figure **IV.3** reveal the effect of varying strontium (Sr) concentrations on the wettability of Sr-coupled ZnO thin films. The angles were measured at three test sites for each sample, with Sr concentrations ranging from 0% (pure ZnO) to 80%. An increasing Sr coupling concentration consistently raises the contact angles, reflecting reduced wettability and enhanced hydrophobicity. The pure ZnO thin film exhibits a contact angle of 119.45°, suggesting moderate hydrophilicity. As the Sr concentration increases to 20%, the contact angle rises to 135.91°, and further increases to 129.02° for 40%, 137.90° for 60%, and 139.18° for 80% Sr coupling. It was observed that the contact angle of the samples increased with the rising strontium concentration, reaching a maximum of 139.18°, indicating that all the films exhibit hydrophobic properties. This behavior is attributed to the increase in surface roughness, as confirmed by the 3D surface topography data presented in table **IV.2.** However, the sample with 40% strontium displayed distinct results, deviating from this trend. This gradual increase in contact angle highlights the role of Sr in modifying the surface energy of the thin films, leading to reduced interaction between the water droplet and the surface. These findings suggest that Sr coupling in ZnO thin films can be a promising approach for tailoring surface wettability for applications requiring hydrophobic or water-repellent surfaces.

IV.2.5. Optical properties

The optical properties of the prepared thin films were analyzed using UV–vis spectroscopy. Figure **IV.4a** shows the optical absorption spectra of pure ZnO and Sr-coupled ZnO thin films within the 280–1200 nm wavelength range. The results indicate that the transmittance of all films decreases at shorter wavelengths, signifying higher light absorption; a common trait of semiconductors. Among the samples, the pure ZnO film exhibits the highest transmittance across the entire range. However, as the Sr content increases, the transmittance progressively decreases [50].

Strontium doping introduces lattice defects in ZnO, acting as light-scattering centers. The thin film containing 20 wt% strontium exhibits the lowest transmittance across the entire wavelength range. Additionally, as the Sr content increases, the intrinsic absorption edge shifts toward longer wavelengths. This observation aligns well with the findings from XRD analysis. For all samples, the lattice structure is predominantly attributed to ZnO, with SrO peaks becoming progressively weaker and eventually disappearing in the ZnO thin films [8].

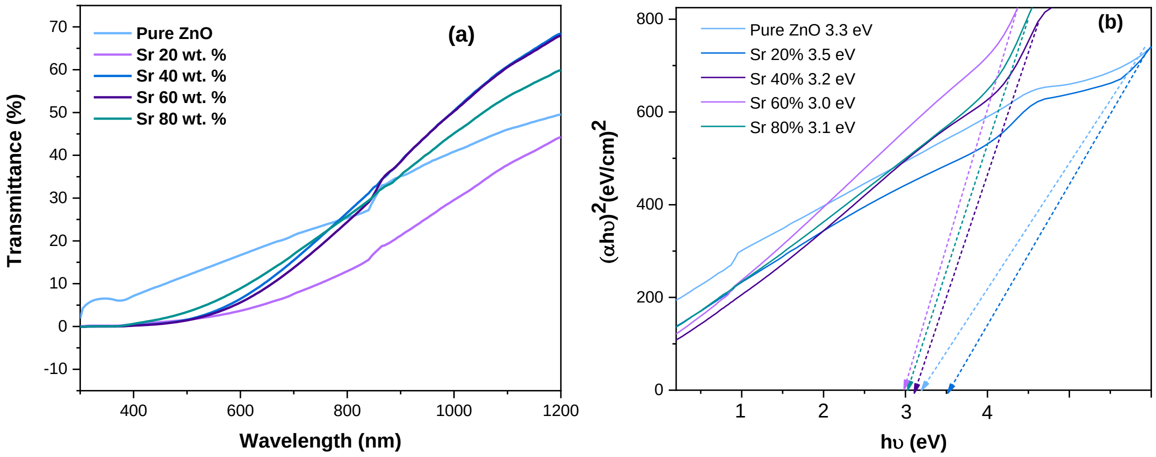

Figure IV.4. (**a**) UV–vis optical transmittance spectra of the deposited samples; (**b**) determination of the band gap of pure ZnO and Sr-coupled ZnO films.

The energy bandgap of the prepared films was determined by extrapolating the linear region of the $(\alpha h\nu)^2$ versus (hν) plot, as illustrated in Figure **IV.4b**. The relationship between the absorption coefficient (α) and photon energy (hν) was analyzed using the Tauc equation [51]:

$$(\alpha h\nu)^n = A\left(h\nu - E_g\right) \tag{05}$$

where, α is the absorption coefficient, hν is the photon energy, *Eg* is the energy bandgap, *A*is the optical constant, and n is the exponent term having different values such as ½, 2, and 3/2 corresponding to direct, indirect, and forbidden transitions, respectively. In this study, n=2 was used, as all the films exhibit a direct transmission slope. The bandgap was estimated by extrapolating the linear region of the $(\alpha h\nu)^2$ versus $h\nu$ plot. This linear extension intersects the x-axis (photon energy) where $(\alpha h\nu)^2$=0, as shown in Figure **IV.4a**. The bandgap values obtained from the Tauc plot for pure ZnO and Sr-coupled ZnO thin films (20, 40, 60, and 80 wt.%) were 3.3, 3.5, 3.2, 3., and 3. 1 eV, respectively.

The bandgap is generally influenced by factors such as crystallite size, charge carrier concentration, and lattice stress. The observed reduction in the optical bandgap of Sr-coupled ZnO thin films can be attributed to the sp-d spin exchange interaction between conduction band electrons and the localized d electrons of Sr ions incorporated into the Zn^{2+} matrix. Additionally, s-d and p-d exchange interactions introduce a negative correction to the conduction band energy levels and a positive adjustment to the valence band levels, leading to a reduction in the bandgap [52]. Furthermore, increasing the strontium concentration in the ZnO lattice reduces the concentration of free electrons while increasing the hole concentration. This shift causes the Fermi level to move to a lower energy state, providing a plausible explanation for the bandgap reduction with higher Sr content [53].

IV.2.6. Photocatalysis process (organic dyes (MB, RB) degradation test)

Table IV.3. Change in temperature, wind, humidity, and solar radiation per hour in the MB degradation test (Biskra, Algeria) on12 November 2023:

Time (hr)	*1*	*2*	*3*	*4*	*5*	*6*
Wind speed (Km/h)	4	4	6	9	9	4
Temperature (C°)	16	17	18	20	24	26
Humidity (%)	51	51	52	52	43	38
Radiation amount (ultraviolet index)	1.41	1.58	2.52	2.72	3.10	3.64

Based on Table **IV.3** and assuming the photocatalyst is active in the UV range, as is common for many photocatalysts, the weather conditions in Biskra, Algeria, on November 12, 2023, could significantly influence the photocatalytic degradation of methylene blue and rose bengal. Solar radiation, indicated by the ultraviolet index (UVI), plays a crucial role in activating the photocatalyst [37]. The table shows a consistent increase in UVI throughout the day, peaking at 3.64 after 6 hours. A higher UVI provides more photons to activate the photocatalyst, potentially accelerating the degradation of the dyes. While temperature does not directly inhibit the process, substantial increases in temperature can affect the reaction kinetics. However, a moderate temperature increase (from 16°C to 20°C) may slightly enhance the reaction rate by promoting faster molecular interactions.

Moderate wind speeds, such as the 9 km/h observed in this case, can improve mass transfer by facilitating the contact of organic dye molecules (MB, RB) with the catalyst surface, potentially speeding up the degradation process. According to Table **IV.3**, humidity decreases slightly throughout the day, from 52% to 38%. While high humidity can sometimes form a water layer on the catalyst surface, which may block light penetration and reduce photon availability to the catalyst, the small reduction in humidity observed here is unlikely to have a significant negative effect.

IV.2.6.1.The fundamental mechanism photocatalysis

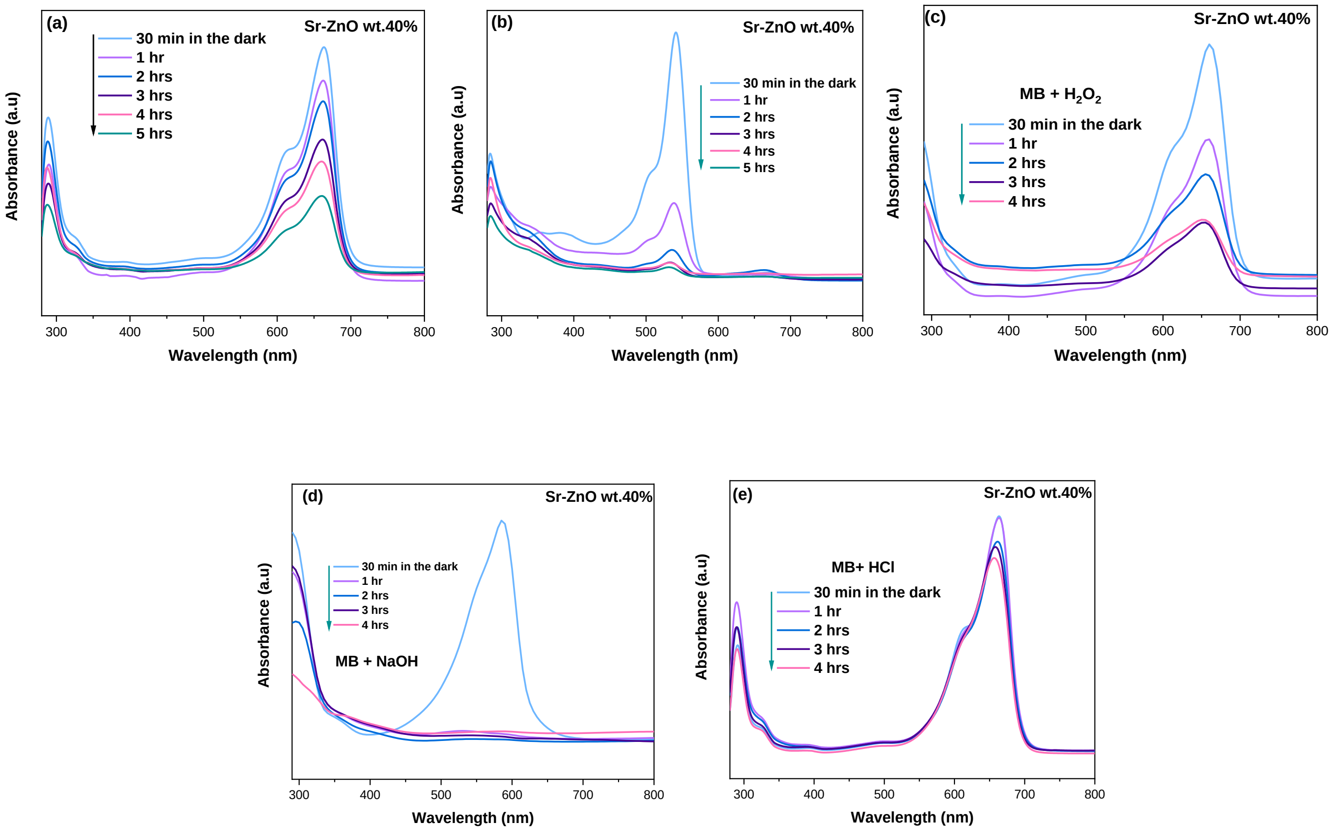

Figure IV.5. The degradation of MB of the 40% Sr **(a)**, The degradation of RB of the 40% Sr **(b)**, The degradation of MB + H_2O_2 of the 40% Sr **(c)**, The degradation of MB + NaOH of the 40% Sr **(d)**, and The degradation of MB + HCl of the 40% Sr **(e)**.

The catalytic mechanism of ZnO and Sr-coupled ZnO, as proposed by Radhi et al. [27] and Rajan et al. [29], has been extensively documented in previous scientific studies. When ultraviolet (UV) light with energy equal to or greater than the bandgap energy of ZnO is applied, photoexcited electrons are promoted from the valence band to the conduction band, leaving vacancies in the valence band and generating electron–hole pairs. These pairs drive redox reactions that ultimately produce hydroxyl radicals. The electron–hole pairs can migrate to the surface of ZnO, where the holes (h^+) react with hydroxide ions or water molecules to form hydroxyl radicals, while the electrons (e^-) interact with molecular oxygen to generate superoxide radicals. The resulting radicals contribute to the synthesis of additional hydroxyl radicals.

The generation of reactive oxygen species (ROS), such as superoxide radicals and hydroxyl radicals, is critical for effective waste degradation, as these species serve as potent oxidizing agents [54, 55]. The incorporation of strontium (Sr) as a dopant enhances the photocatalytic process by acting as an electron scavenger. Sr traps the excited electrons, reducing the likelihood of recombination with photogenerated holes and thereby extending the lifetime of these excited charge carriers. This prolonged lifetime allows more effective interaction between the photogenerated carriers and water molecules, facilitating the formation of highly reactive oxidizing species such as superoxide ions ($O_2^{-\bullet}$) and hydrogen peroxide (H_2O_2). These species, which are non-selective and highly reactive, can cleave organic bonds and effectively decompose various pollutants [56, 57]. The underlying redox reactions involved in this photocatalytic process under UV irradiation are summarized in the following equations [39]:

$$Sr - ZnO + light(h\nu) \rightarrow e^-(CB) + h^+(VB) \tag{06}$$

$$e^- + O_2(adsorbed) \rightarrow O_2^{-\bullet} \tag{07}$$

$$h^+ + H_2O \rightarrow OH^\bullet \tag{08}$$

Superoxide and hydroxyl radicals subsequently interact with the pollutant methylene blue, resulting in the breakdown of the dye and the formation of various degradation byproducts.

$$(O_2^{-\bullet}, OH^\bullet) + organic\ dyes\ (MB, RB) \rightarrow degradation\ products \tag{09}$$

This synergistic interaction enhances the accumulation of electrons on the ZnO surface and increases the concentration of holes on the Sr/ZnO surface. Collectively, these effects significantly improve the photocatalytic efficiency in the degradation of methylene blue (MB) or rose bangal (RB).

The results indicate that Sr doping plays a significant role in the photocatalytic degradation of organic dyes such as methylene blue (MB) and rose bangal (RB). While certain coupling levels, such as 40% Sr, enhance photocatalytic efficiency, others, including 20% and 60% Sr, may reduce it compared to pure ZnO. These findings highlight the importance of determining the optimal doping concentration to maximize efficiency for specific photocatalytic applications.

The impact of indirect band gap energies on photocatalysis was empirically demonstrated, revealing that a decrease in band gap values (from 3.5 eV to 3.0 eV) corresponds to a proportional enhancement in photocatalytic efficiency (from 87.62% to 94.67%). The band gap is a critical factor, as a smaller band gap allows for the absorption of a broader spectrum of sunlight, thereby increasing photocatalytic activity. However, excessive doping can introduce defects that impair charge separation and promote recombination, ultimately reducing the overall efficiency.

Table IV.4. The photocatalytic degradation efficiency of (MB, RB, hole-scavenger Sr 40%) and band gap (Eg) for pure ZnO and Sr-coupled ZnO thin films:

Samples	***Efficiency ‘η’ (%) MB***	***Efficiency ‘η’ (%) (MB)***			***Efficiency ‘η’ (%) RB***	***Band gap (Eg) (eV)***
		+ NaOH	*+ H_2O_2*	*+ HCl*		
Pure ZnO	73.73	-	-	-	87.62	3.3
Sr 20%	59.04	-	-	-	86.09	3.5
Sr 40%	89.62	97.60	91.47	38,08	94.67	3.2
Sr 60%	53.69	-	-	-	73.21	3.0
Sr 80%	47.89	-	-	-	79.99	3. 1

Table **IV.4** demonstrates that Sr doping enhances the photocatalytic degradation efficiency of ZnO thin films for both methylene blue (MB) and rose bangal (RB) dyes. This improvement is primarily attributed to the reduced band gap of Sr-coupled films, allowing them to absorb a broader spectrum of light and generate more electron-hole pairs to drive the degradation reactions. The optimal coupling concentration appears to be approximately 40% Sr, at which point the degradation efficiencies for both MB and RB reach their maximum. In contrast, higher Sr concentrations (60% and 80%) further reduce the band gap but result in decreased degradation efficiency. This indicates the existence of an optimal balance between band gap reduction and other factors influencing photocatalytic performance, such as structural properties, particle size, and film thickness [58].

The photocatalytic efficiency improved to 97.60% with NaOH and 91.47% with H_2O_2 additions. This enhancement is attributed to the generation of hydroxyl radicals ($OH^{\cdot}$), which result from the reaction of NaOH with methylene blue, thereby promoting its decomposition [59]. Similarly, hydrogen peroxide (H_2O_2) produces hydroxyl radicals that facilitate the degradation of MB. In contrast, the efficiency significantly decreased to 38.08% upon the addition of hydrochloric acid (HCl). This decline is likely due to the presence of H^+ ions from HCl, which compete with MB for adsorption sites on the ZnO surface, thereby hindering MB degradation. According to the literature [39,40], Sr-coupled ZnO thin films with 40% Sr demonstrate excellent photocatalytic activity for the degradation of organic pollutants such as MB and rose bangal (RB). Furthermore, the addition of NaOH or H_2O_2 further enhances MB degradation efficiency. The performance of Sr-coupled ZnO thin films in degrading MB and RB is comparable to, or even surpasses, the efficiency of leading heterogeneous catalysts reported in recent studies, as summarized in Table **IV.5**.

Table IV.5. Compare the degradation efficiency of the current work with other reported works.

S.No	***Materials***	***Methods***	***Organic dyes***	***Efficiency 'η' (%)***	***Ref.***
1	Sb-ZnO/ MoS2	Tape casting method	MB	78	[58]
2	ZnO	Sol-gel	RhB	54.7	[59]
3	Mn/ZnO	Sol-gel	MB	32.6	[60]
4	ZnO	spray pyrolysis	4-NP	94	[61]
5	CdS/ZnO	SILAR	MB	91	[62]
6	N/ZnO	Solvent-free mechanochemical method	MB	94	[63]
7	Cu/ ZnO	SILAR	Orange G	52	[64]
8	ZnS/PbS	spin-coating	MO	68.8	[65]
9	Sr/ZnO	SILAR	MB	89.62	present work
10	Sr/ZnO	SILAR	RB	94.67	present work

A comparative analysis of the organic dye degradation efficiencies across various studies highlights the diverse methodologies and their corresponding performances. Notably, the efficiency of Sb-ZnO/MoS2 for degrading methylene blue achieved 78% using a tape casting method, while ZnO synthesized via sol-gel demonstrated a lower efficiency of 54.7% for rhodamine B (RhB). The Mn/ZnO system also fell short with an efficiency of 32.6% for MB. Conversely, the spray pyrolysis approach for pure ZnO reported the highest efficiency at 94% for 4-nitrophenol (4-NP). CdS/ZnO achieved a notable efficiency of 91% for MB via SILAR, while an N/ZnO composite utilizing a solvent free mechano-chemical method presented a remarkable efficiency of 94% for MB. The efficiencies of Cu/ZnO for Orange G (52%) and ZnS/PbS for methylene orange (MO) (68.8%) were notably lower. Moreover, the present work on Sr/ZnO via SILAR exhibited an efficiency of 89.62% for MB, matching closely with the 94.67% efficiency for rose bangal via SILAR, indicating that Sr/ZnO is a promising candidate for organic dye degradation. Collectively, these studies underscore the influence of material composition and synthesis methods on the photocatalytic efficiencies achieved.

IV.2.6.2. Photocatalysis kinetics

A pseudo-first-order kinetic model was utilized to analyze the photodegradation of methylene blue, rose bangal, and MB again, in the presence of NaOH, hydrogen peroxide (H_2O_2), and hydrochloric acid (HCl). The application of light irradiation resulted in a reduction of absorbance at the maximum wavelengths specific to MB (663 nm) and RB (546 nm).

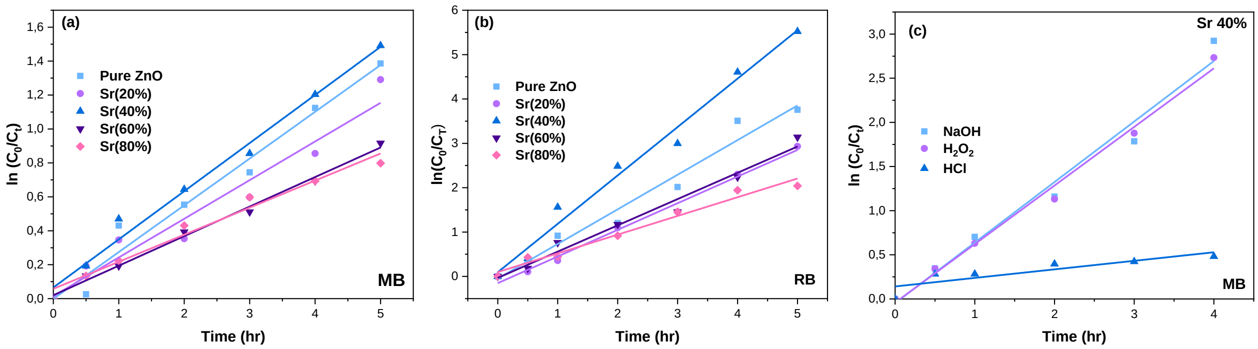

Figure IV.6. Pseudo-first-order kinetic plot of ln(C_0/C_t) vs time of : (**a**) MB; (**b**) RB degradation in the presence of different catalysts thin films and; (**c**) MB + (H_2O_2 or NaOH or HCl) of Sr 40%.

The figure **IV.6a-c** shows the linear relationship between ln(C_0/C_t) and time confirms pseudo-first-order reaction kinetics. Various doping levels of strontium on zinc oxide thin films influence the degradation rate of MB, with certain doping levels exhibiting enhanced photocatalytic performance.

Similarly, RB follows pseudo-first-order kinetics, with the performance varying across different strontium-doped thin films. The differences in the slope of the lines indicate changes in the reaction rate constants, reflecting the impact of the doping concentration on the catalytic activity.

The addition of NaOH, H_2O_2, or HCl significantly impacts the degradation kinetics of MB, as seen in the distinct slopes for each additive. The presence of NaOH or H_2O_2 accelerates the reaction, while HCl results in a lower rate constant, suggesting that the reaction environment strongly affects photocatalytic efficiency.

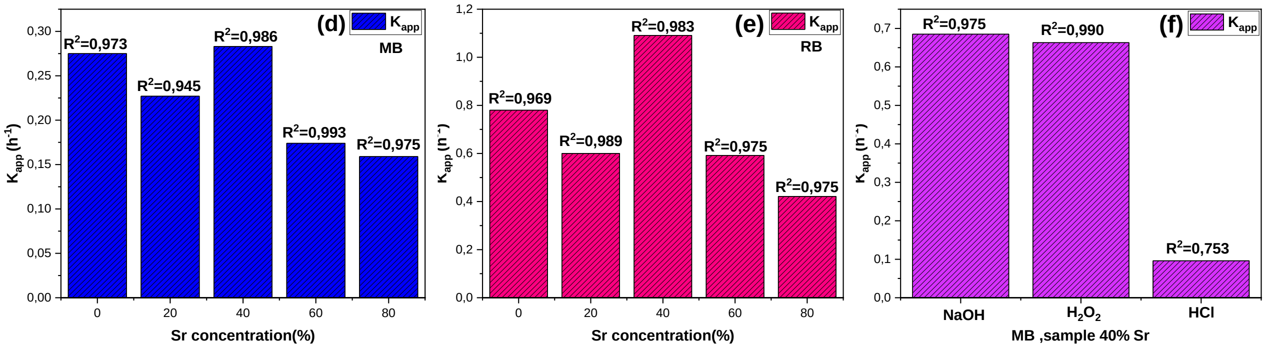

Figure IV.7. Reaction rate constants and R^2 values of kinetic data of pseudo-first-order model for MB **(d)**, RB **(e)** on Sr-coupled ZnO and MB + (H_2O_2 or NaOH or HCl) of Sr 40%under sunlight **(f)**.

The apparent reaction rate constant (K_{app}) for the photocatalytic materials were also determined using the following formula [65]:

$$K_{app} = \frac{1}{t} ln\left({}^{C_0}/_{C_t}\right) \qquad (10)$$

The concentrations C_0 and C_t represent the initial concentration at time t=0 and the concentration at a given time t, respectively. A linear relationship between $\ln(C_0/C_t)$ and time, observed for all dyes, confirms that the process follows pseudo-first-order reaction kinetics.

The photocatalytic degradation process was modeled using the Langmuir-Hinshelwood framework. The calculated rate constants (K_{app}) were 0.283 hr^{-1} for MB, 1.091 hr^{-1} for RB, and 0.685 hr^{-1}, 0.663 hr^{-1}, and 0.096 hr^{-1} for MB with NaOH, H_2O_2, and HCl additives (40%), respectively, as illustrated in Figure **IV.7 (d-f).** These rate constants highlight the efficiency and stability of the photocatalysis process.

IV.3. Conclusion

This chapter presented an in-depth investigation into the photocatalytic performance of Sr-coupled ZnO thin films synthesized using the successive ionic layer adsorption and reaction (SILAR) method. The study primarily focused on the structural, optical, and photocatalytic properties of these thin films, with a special emphasis on their application in degrading organic pollutants, namely methylene blue (MB) and rose bengal (RB).

X-ray diffraction (XRD) analysis revealed that Sr doping significantly influenced the crystalline structure of ZnO thin films by reducing the crystallite size and introducing lattice strain. Scanning electron microscopy (SEM) demonstrated morphological changes, transitioning from nanorod structures in pure ZnO to mixed nanorods and spherical clusters in Sr-doped samples. These structural modifications were accompanied by alterations in surface roughness and hydrophobicity, as evidenced by contact angle measurements, which confirmed the potential of Sr-doped ZnO thin films for applications requiring tailored wettability.

UV-visible spectroscopy indicated that Sr coupling effectively narrowed the bandgap of ZnO, enhancing its ability to absorb visible light. This bandgap reduction played a pivotal role in boosting the photocatalytic activity of the films under sunlight irradiation. Among the studied samples, the thin film doped with 40% Sr exhibited the highest photocatalytic degradation efficiency, achieving 89.62% for MB and 94.67% for RB. These findings underscore the importance of optimizing Sr concentrations to achieve the best performance.

Additionally, the study explored the effects of solution acidity and the presence of hole scavengers (e.g., NaOH, H_2O_2, and HCl) on the photocatalytic process. The addition of NaOH and H_2O_2 significantly enhanced the degradation efficiency by generating hydroxyl radicals, while the presence of HCl inhibited the process due to competitive adsorption effects. These results demonstrate the versatility of Sr-coupled ZnO thin films in adapting to various environmental conditions for effective pollutant removal.

In conclusion, this research highlights the potential of Sr-coupled ZnO thin films as cost-effective and efficient photocatalysts for water remediation. By addressing key limitations such as electron-hole recombination and limited visible-light absorption, Sr coupling significantly improves the photocatalytic properties of ZnO thin films. These findings contribute to the advancement of sustainable technologies for organic pollutant degradation and pave the way for future research on optimizing dopant concentrations and exploring new applications of doped ZnO materials.

References of chapter IV

[1] Li, Caifang, et al. "Preparation, characterization of graphitic carbon nitride photo-catalytic nanocomposites and their application in wastewater remediation: a review." *Crystals* 11.7 (2021): 723.

[2] Althamthami, Mohammed, et al. "Impact of surface topography and hydrophobicity in varied precursor concentrations of tenorite (CuO) films: a study of film properties and photocatalytic efficiency." *Scientific Reports* 14.1 (2024): 7928.

[3] Sun, Yue, et al. "Preparations and applications of zinc oxide based photocatalytic materials." Advanced Sensor and Energy Materials (2023): 100069.

[4] Ahmed, Shahzad, et al. "Electrochemical and optical-based systems for SARS-COV-2 and various pathogens assessment." *Advances in Natural Sciences: Nanoscience and Nanotechnology* 14.3 (2023): 033001.

[5] Sathya, M., et al. "Photocatalytic Degradation Properties of SILAR Grown ZnO: Ag Thin Films: Investigation on the Effect of Ag Loading." *Brazilian Journal of Physics* 52.1 (2022): 23.

[6] Boughelout, A., et al. "Photocatalysis of rhodamine B and methyl orange degradation under solar light on ZnO and Cu2O thin films". *React Kinet Mech Catal* 129 (2020): 1115–1130.

[7] Wang, Lili, et al. "Constructing recyclable photocatalytic BiOBr/Ag nanowires/cotton fabric for efficient dye degradation under visible light." *Arabian Journal of Chemistry* 16.4 (2023): 104624.

[8] Althamthami, Mohammed, et al. "Effect of different Cu: Co film concentrations on photocatalytic reactions of ethanol, MB, AMX, and Cr (VI): A study of film properties & effects of photooxidation." *Journal of Environmental Chemical Engineering* 11.6 (2023): 111247.

[9] Aslan, Esra, GulsenSahin, and Abdullah Goktas. "Facile synthesis of Sb2S3 micro-materials for highly sensitive visible light photodetectors and photocatalytic applications." *Materials Chemistry and Physics* 307 (2023): 128160.

[10] Hajji, Moez, et al. "Photocatalytic performance and solar cell applications of coupled semiconductor CuO–ZnO sprayed thin films: Coupling effect between oxides." *Optical Materials* 140 (2023): 113798.

[11] Sendi, Rabab Khalid. "Fabrication of high voltage gradient ZnO nanoparticle-Bi2O3-Mn2O3-based thick film varistors at various sintering temperature." *Journal of King Saud University-Science* 34.3 (2022): 101820.

[12] Mamtmin, Gulgina, et al. "Composite optical waveguide sensor based on porphyrin@ ZnO film for sulfide-gas detection." *Chinese Journal of Analytical Chemistry* 51.7 (2023): 100260.

[13] Widyastuti, Endrika, et al. "Photocatalytic antimicrobial and photostability studies of TiO2/ZnO thin films." *Arabian Journal of Chemistry* 16.8 (2023): 105010.

[14] Thirumoorthi, M., et al. "High responsivity n-ZnO/p-CuO heterojunction thin film synthesised by low-cost SILAR method for photodiode applications." *Optical Materials* 128 (2022): 112410.

[15] Mylarappa, M., et al. "Study of ZnO nanoparticle-supported clay minerals for electrochemical sensors, photocatalysis, and antioxidant applications." *ChemPhysMater* 3.1 (2024): 83-93.

[16] Klochko, N. P., et al. "Solution-processed flexible broadband ZnO photodetector modified by Ag nanoparticles." *Solar Energy* 232 (2022): 1-11.

[17] Al Farsi, B., et al. "Structural and optical properties of visible active photocatalytic Al doped ZnO nanostructured thin films prepared by dip coating." *Optical Materials* 113 (2021): 110868.

[18] Goktas, Abdullah, et al. "Facile synthesis and characterization of ZnO, ZnO: Co, and ZnO/ZnO: Co nano rod-like homojunction thin films: Role of crystallite/grain size and microstrain in photocatalytic performance." *Journal of Alloys and Compounds* 893 (2022): 162334.

[19] Goktas, Sultan, Ahmet Tumbul, and Abdullah Goktas. "Growth technique–induced highly C-axis-oriented ZnO: Mn, Zno: Fe and ZnO: Co thin films: a comparison of nanostructure, surface morphology, optical band gap, and room Temperature ferromagnetism." *Journal of Superconductivity and Novel Magnetism* 36.10 (2023): 1875-1892.

[20] Aba, Zekiye, Abdullah Goktas, and Ahmet Kilic. "Characterization of Zn1-xLaxS thin films; compositional, surface, optical, and photoluminescence properties for possible optoelectronic and photocatalytic applications." *Journal of Sol-Gel Science and Technology* 109.1 (2024): 260-271.

[21] Ravichandran, K., et al. "Improved solar light responsive photocatalytic activity of ZnO: W films: Effect of W loading level." *Materials Today: Proceedings* 48 (2022): 216-228.

[22] Xu, Linhua, et al. "Optical and structural properties of Sr-doped ZnO thin films." *Materials Chemistry and Physics* 148.3 (2014): 720-726.

[23] Nezzal, Hala, et al. "Photo-deposition of AgO thin films on TiO2 substrate for (PN) hetero-junction applications: Considering the degree of contamination." *Journal of Alloys and Compounds* 1010 (2025): 177331.

[24] Yatskiv, R., et al. "Defect-mediated energy transfer in ZnO thin films doped with rare-earth ions." *Journal of Luminescence* 253 (2023): 119462.

[25] Kirik, Nurdan Selin, and BünyaminŞahin. "Characteristics modification of ZnO/CuO composite films by doping rare-earth element Dy for real-time hydration level monitoring." *Micro and Nanostructures* 167 (2022): 207290.

[26] Raj, K. Pradeev, et al. "Structural, optical, photoluminescence and photocatalytic assessment of Sr-doped ZnO nanoparticles." *Materials Chemistry and Physics* 183 (2016): 24-36.

[27] Devi, K. Radhi, et al. "Enhanced room temperature ammonia gas sensing properties of strontium doped ZnO thin films by cost-effective SILAR method." *Materials Science in Semiconductor Processing* 119 (2020): 105117.

[28] Water, Walter, and Yin-Shiang Yan. "Characteristics of strontium-doped ZnO films on love wave filter applications." *Thin solid films* 515.17 (2007): 6992-6996.

[29] Rajan, Aneesiya K., and L. Cindrella. "Ameliorating the photovoltaic conversion efficiency of ZnO nanorod based dye-sensitized solar cells by strontium doping." *Superlattices and Microstructures* 128 (2019): 14-22.

[30] Goktas, S., and A. Goktas. "A comparative study on recent progress in efficient ZnO based nanocomposite and heterojunction photocatalysts: A review." *Journal of Alloys and Compounds* 863 (2021): 158734.

[31] Sahin, Gulsen, Abdullah Goktas, and Esra Aslan. "A new way to tune photocatalytic activity, surface morphology, and structural/optical parameters of ZrO2 thin films using different Zr sources along with annealing temperature and film thickness." *Journal of Sol-Gel Science and Technology* 112.2 (2024): 425-443.

[32] Bedia, Asma, et al. "Morphological and optical properties of ZnO thin films prepared by spray pyrolysis on glass substrates at various temperatures for integration in solar cell." *Energy Procedia* 74 (2015): 529-538.

[33] Gözükızıl, M. Fatih. "PH effect on structural, morphological and optical properties of ZnO thin films produced by chemical bath deposition method." *Eur Chem Bull* 9.10 (2020): 335-338.

[34] Althamthami, Mohammed, et al. "Improved photocatalytic activity under the sunlight of high transparent hydrophilic Bi-doped TiO2 thin-films." *Journal of Photochemistry and Photobiology A: Chemistry* 443 (2023): 114818.

[35] Balu, Krishnakumar, et al. "Porphyrins and ZnO hybrid semiconductor materials: A review." *Inorganic Chemistry Communications* 154 (2023): 110973.

[36] Al Hassan, Md Rahat, et al. "Synthesis of spray deposited transition metals doped (Cr, Mn, Fe, Ni, and Cu) compositionally complex ZnO thin films with enhanced band gap and magnetism." *Results in Materials* 13 (2022): 100263.

[37] Goktas, A. "High-quality solution-based Co and Cu co-doped ZnO nanocrystalline thin films: Comparison of the effects of air and argon annealing environments." *Journal of Alloys and Compounds* 735 (2018): 2038-2045.

[38] Barkat, Hadjer, et al. "Enhancing sunlight-driven photocatalysis: high transparency and hydrophilic advancements in Ba-Doped ZnO thin films." *Journal of Materials Engineering and Performance* (2024): 1-14.

[39] Althamthami, Mohammed, et al. "Influence of hole-scavenger and different withdrawn speeds on photocatalytic activity of Co3O4 thin films under sunlight irradiation." *Ceramics International* 48.21 (2022): 31570-31578.

[40] Syampurwadi, Anung, Indah Primadona, and Vivi Fauzia. "Facile photochemical reduction synthesis of bimetallic Au and Pd nanoparticles on ZnO nanorods for improved photocatalytic degradation of methylene blue." *Advances in Natural Sciences: Nanoscience and Nanotechnology* 13.2 (2022): 025013.

[41] Mrabet, C., et al. "CuO-ZnO nanocomposites-based thin films: Characterization, physical properties and sunlight photocatalytic degradation of organic pollutants." *Journal of Alloys and Compounds* 968 (2023): 172252.

[42] Zheng, Gaige, et al. "Enhanced photocatalytic activity of ZnO thin films deriving from a porous structure." *Materials Letters* 150 (2015): 1-4.

[43] Gupta, Prateek, and Bhubesh C. Joshi. "Influence of Cu incorporation on structural, optical, and electronic structure of ZnO thin films deposited by laser ablation." *Physica B: Condensed Matter* 668 (2023): 415251.

[44] Temam, Elhachmi Guettaf, et al. "Photocatalytic activity of Al/Ni doped TiO2 films synthesized by sol-gel method: Dependence on thickness and crystal growth of photocatalysts." *Surfaces and Interfaces* 31 (2022): 102077.

[45] Kumari, Vijaya, et al. "Synthesis and characterization of heterogeneous ZnO/CuO hierarchical nanostructures for photocatalytic degradation of organic pollutant." *Advanced Powder Technology* 31.7 (2020): 2658-2668.

[46] Raghavendra, P. V., J. S. Bhat, and N. G. Deshpande. "Enhancement of photoluminescence in Sr doped ZnO thin films prepared by spray pyrolysis." *Materials Science in Semiconductor Processing* 68 (2017): 262-269.

[47] Zhang, Lei, et al. "Core-shell structured ZnO homojunction for enhanced photocatalysis." *Inorganic Chemistry Communications* 148 (2023): 110281.

[48] Algün, Gökhan, et al. "Synthesis and ultrafast humidity sensing performance of Sr doped ZnO nanostructured thin films: the effect of Sr concentration." *Journal of Sol-Gel Science and Technology* 107.3 (2023): 640-658.

[49] Umarani, P., et al. "Tuning of optical and vapour sensing properties of manganese-doped cadmium oxide thin films for sensor applications." *Optical Materials* 149 (2024): 115126.

[50] Hirschle, Patrick, et al. "Exploration of MOF nanoparticle sizes using various physical characterization methods–is what you measure what you get?." *CrystEngComm* 18.23 (2016): 4359-4368.

[51] Mokrani, Nourelhouda, et al. "Boosting photocatalytic stability: hydrophilic Sr-doped ZnO thin films prepared via the SILAR method for enhanced performance over multiple cycles." *Physica Scripta* 99.9 (2024): 0959a4.

[52] Battal, W., et al. "Strontium doping effect on characteristics of ultrasonically sprayed zinc oxide thin films." *Applied Physics A* 126 (2020): 1-10.

[53] Fatemi, Ali, et al. "Author Correction: Optical and structural properties of Sn and Ag-doped PbS/PVA nanocomposites synthesized by chemical bath deposition." *Scientific Reports* 13.1 (2023): 9873.

[54] Serrà, Albert, et al. "Highly active ZnO-based biomimetic fern-like microleaves for photocatalytic water decontamination using sunlight." *Applied Catalysis B: Environmental* 248 (2019): 129-146.

[55] Sanakousar, F. M., et al. "Recent progress on visible-light-driven metal and non-metal doped ZnO nanostructures for photocatalytic degradation of organic pollutants." *Materials science in semiconductor processing* 140 (2022): 106390.

[56] Göktaş, Sultan. "Synergic effects of pH, reaction temperature, and various light sources on the photodegradation of methylene blue without photocatalyst: a relatively high degradation efficiency." *Chemistry Africa* (2024): 1-13.

[57] Patil, S. B., et al. "Sugarcane juice facilitated eco-friendly synthesis of solar light active CdFe 2 O 4 nanoparticles and its photocatalytic application." *The European Physical Journal Plus* 133 (2018): 1-16.

[58] Masekela, Daniel, et al. "Internal piezoelectric field produced by tri-component (FTO: Sb-ZnO/MoS2) thin film for enhanced photocatalytic degradation of organic pollutants and antibacterial activity." *Materials Today Communications* 38 (2024): 108500.

[59] Tański, Tomasz, et al. "Hydrophilic ZnO thin films doped with ytterbium and europium oxide." *Scientific Reports* 12.1 (2022): 11329.

[60] Vallejo, William, Alvaro Cantillo, and Carlos Díaz-Uribe. "Improvement of the photocatalytic activity of ZnO thin films doped with manganese." *Heliyon* 9.10 (2023).

[61] Cuadra, J. González, et al. "Functional properties of transparent ZnO thin films synthetized by using spray pyrolysis for environmental and biomedical applications." *Ceramics International* 49.20 (2023): 32779-32788.

[62] Velanganni, S., et al. "Nanostructure CdS/ZnO heterojunction configuration for photocatalytic degradation of Methylene blue." *Physica B: Condensed Matter* 534 (2018): 56-62.

[63] Sudrajat, Hanggara, and Sandhya Babel. "Photocatalytic degradation of methylene blue using visible light active N-doped ZnO." *Advanced materials research* 1101 (2015): 299-302.

[64] Jellal, Ilyass, et al. "Enhanced photocatalytic activity of supported Cu-doped ZnO nanostructures prepared by SILAR method." *Optical Materials* 111 (2021): 110669.

[65] Aouf, D., et al. "Facile preparation and characterization of nanostructured ZnS/PbS heterojunction thin films for enhanced microbial inhibition and photocatalytic degradation." *Materials Chemistry and Physics* 295 (2023): 127059.

Chapter V:

Effect of Different Additives on Sr-doped ZnO Thin Films For The Removal of MB and AMX Using The Photocatalytic Process

V.1.Introduction

As society advances and living conditions improve, environmental preservation and public well-being have emerged as critical areas of global concern [1]. Modern water purification methods, including membrane filtration, adsorption, and advanced oxidation processes, offer significant advantages over traditional techniques like coagulation, flocculation, and activated carbon filtration. Although cost-effective and technologically advanced, conventional methods often lead to secondary pollution and are less effective in addressing complex contaminants [2,3].Emerging technologies, such as photocatalytic oxidation and ion exchange, provide higher efficiency and reduced secondary pollution but are often constrained by high infrastructure costs [4]. Nanotechnology is revolutionizing modern water treatment by providing innovative solutions that surpass traditional methods. It utilizes nanomaterials such as carbon nanotubes and nanostructured membranes, which have unique properties such as high surface area and reactivity, enabling them to effectively remove a variety of contaminants from wastewater, including heavy metals, organic pollutants and emerging contaminants [5,6,7].Nanotechnology enhances processes such as ultrafiltration and advanced oxidation, leading to improved efficiency and cost-effectiveness in water treatment [8]. For instance, nanostructured membranes are particularly effective in desalination and can selectively separate contaminants, addressing the urgent need for clean water in arid regions [7]. Furthermore, the versatility of nanomaterials allows for their application in various treatment methods, including adsorption and catalysis, which are crucial for effective remediation of polluted water [9].

Strontium doping enhances the photocatalytic activity of zinc oxide (ZnO) by altering its structural and optical properties. Studies have shown that incorporating strontium ions into the ZnO lattice reduces the optical band gap, improving light absorption and charge separation. For instance, strontium-doped ZnO exhibited a band gap reduction from 3.27 eV to 2.98 eV, which correlates with improved photocatalytic efficiency, achieving over 80% degradation of methylene blue dye at optimal doping levels [10]. Additionally, the presence of strontium enhances the material's ability to absorb sunlight, shifting the bandgap into the visible region, which is crucial for effective photocatalysis under solar irradiation [11]. Excessive strontium doping, however, may adversely affect crystallinity and charge mobility, leading to reduced photocatalytic performance [12]. Overall, strontium doping emerges as a promising strategy to optimize ZnO photocatalysts for environmental applications.

Strontium (Sr) doping in zinc oxide (ZnO) significantly enhances its properties through various mechanisms involving specific chemical additives. The primary additive used for doping is strontium carbonate (SrCO3), which facilitates the incorporation of Sr into the ZnO lattice, leading to structural modifications without altering the wurtzite crystal structure of ZnO [13,14].

This chapter provides a comparative analysis of how various additives influence the structural, morphological, optical, and surface characteristics of strontium-doped zinc oxide (ZnO/Sr) thin films prepared using the Successive Ionic Layer Adsorption and Reaction technique. The incorporation of different additives was systematically linked to modifications in the crystal structure, surface roughness and optical properties of the ZnO/Sr layers, demonstrating their critical role in tuning photocatalytic efficiency. By tailoring these properties, the additives enabled enhanced light absorption, charge carrier dynamics, and surface activity, which are pivotal for the photocatalytic degradation of organic pollutants, such as methylene blue and amoxicillin.

V.2. Results and discussion

V.2.1.Structural analysis

The X-ray diffraction profile of chemically prepared Sr-doped ZnO thin films, in the range of $20° < 2\theta < 80°$ with a step size of 0.03° is shown in Figure **V.1**. All the visible peaks are indexed as characteristic peaks of ZnO wurtzite structure (**JCPDS No. 01-075-0576**).The results indicate that all thin films in the as deposited state have a wurtzite structure, and no additional peaks corresponding to Sr were detected [16,17].The ionic radius of strontium is 1.18 Å, while that of zinc oxide is 0.74 Å.

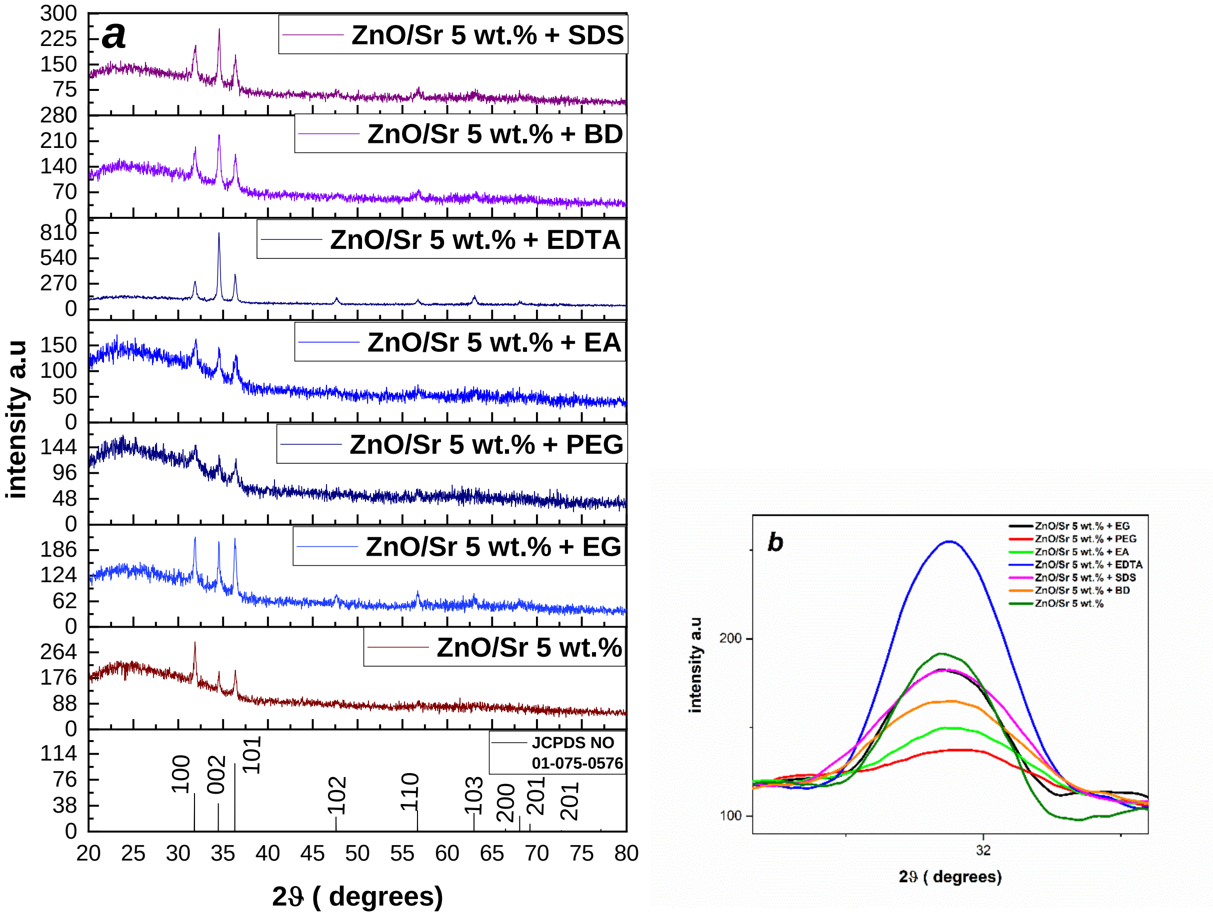

FigureV.1. (**a**) XRD patterns of Sr/ZnO 5 wt.% based thin films at different additives.; (**b**) Enlarged view of different additives dependent shift in the position of peaks due to (100) plane along 2ϑ axis.

The diffraction peak positions vary with different additives, shifting to lower angles in the presence of PEG, EG, and EA due to the distinct properties of these additives [18]. It is evident that films stabilized by EDTA exhibit proper crystallization, with crystals showing a preferential orientation along the (002) axis, which is perpendicular to the substrate. We notice the change in the type of adjective the peak intensity increases (002), except in the cases of PEG, EG and EA the peak intensity decreases. The additives used in the solution did not lead to the formation of a new compound, and we attribute the change in the (002) peak, the variability of its intensity and its oscillatory behaviour to the changes in the crystallinity of Sr-ZnO. The Scherrer equation was used to determine the crystallite dimensions (D_{hkl}) of Sr-doped ZnO thin films. The crystallite size of the samples differs from one another depending on the additives. The effect of the additives is also responsible for the changes in the Sr-doped ZnO lattice parameters, as shown in Table **V.1.**

In the hexagonal wurtzite structure, a=b≠c and $\alpha=\beta=90°$, $\gamma=120°$. Thus, the lattice parameter can be articulated within the hexagonal configuration using the two parameters a and c: equations 1 and 2 [19].

$$a = b = \frac{\lambda}{Sin\vartheta\sqrt{3}} \tag{01}$$

$$c = \frac{\lambda}{Sin\vartheta} \tag{02}$$

Table V.1. The estimated values of 2theta (deg), FWHM, crystallites size, number of crystallites and lattice paramaters for ZnO/Sr thin films at different additives of plan (002):

Samples	*2theta (deg)*	*FWHM*	*Crystallites size (nm)*	*Number of crystallites* $(\times 10^{15} m^{-2})$	*Lattice paramaters(A°)*	
					a	*c*
ZnO/Sr 5%	34.58	0.18	46.19	1. 07	2.995	5.187
ZnO/Sr 5% + EA	34.59	0.31	26.82	17.13	2.994	5.185
ZnO/Sr 5% + EDTA	34.59	0.23	36.15	6.08	2.994	5.185
ZnO/Sr 5% + EG	34.57	0.19	43.76	0.84	2.996	5.188
ZnO/Sr 5% + PEG	34.58	0.4	20.78	28.87	2.995	5.187
ZnO/Sr 5% + SDS	34.60	0.22	37.79	5.7	2.993	5.184
ZnO/Sr 5% + BD	34.59	0.33	25.19	13.01	2.994	5.185

The approximate dimensions of the Sr-doped ZnO particles are summarized in Table **V.1.** In the current study, the computed crystallites size is in the interval of 20–46 nm. It can be clearly seen that the particle size of Sr-doped ZnO decreases with the addition of the additives. The crystallites size increases in the EG sample and decreases in the PEG sample, and there are also good values for the crystallites size in the SDS sample.

V.2.1.1 Scherrer plot

The Scherrer equation was used to investigate the crystallite size, which is calculated by the following relationship:

$$D = \frac{k\lambda}{\beta_D \cos\vartheta} \tag{03}$$

where K (0.9) is the shape factor, D is the average crystallite dimension, λ=1.5408 is the wavelength associated with the Cu Kα radiation, β is the full width at half maximum (FWHM) and θ refers to the angle of Bragg diffraction. The instrumental widening was estimated using the following equation:

$$\cos\vartheta = (k\lambda/D)(1/\beta_{hkl}) \tag{04}$$

A graph correlating $1/\beta_{hkl}$ with cosϑ was created to examine the crystallite dimensions of the samples using the slope derived from linear regression analysis **Fig V.2.**

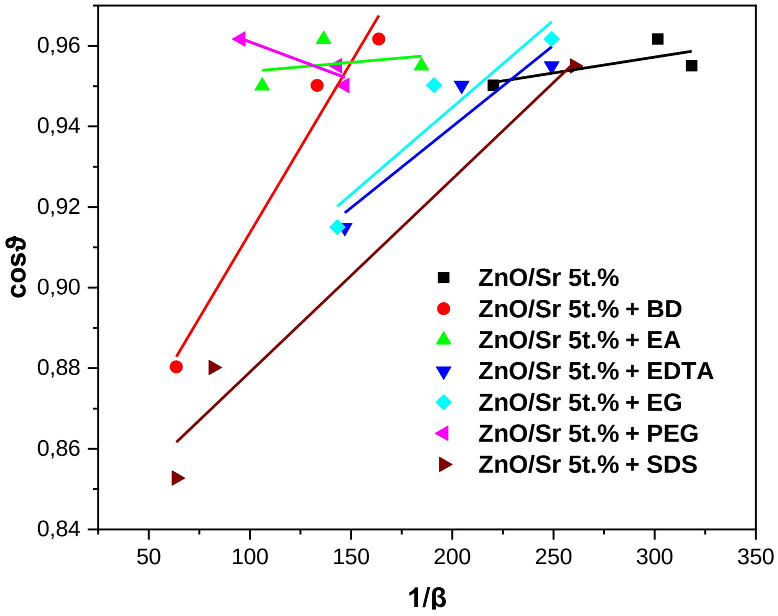

Figure V.2. Scherrer plot for Sr-doped ZnO 5 wt.% thin films at different additives.

The dislocation density (δ) is characterized as the quantification of dislocation lines within a given unit volume and is determined by the following equation [20]:

$$\delta = \frac{1}{D^2} \tag{05}$$

where, δ is the dislocation density. The lowest dislocation density is observed for EG, indicating high crystallinity. BD, PEG and EA show higher dislocation densities, suggesting a greater number of structural defects (**Table V.2**).

Table V.2. The estimated values of crystallites size (scherrer and plot scherrer methods) and dislocation density:

Samples	*ZnO/Sr 5%*	*EA*	*EDTA*	*PEG*	*SDS*	*BD*	*EG*
Scherrer method D(nm)	46.19	26.82	36.15	20.78	37.79	25.19	43.76
Scherrer Plot method D(nm)	32.14	23.29	29.84	13.76	37	23.59	30.07
Dislocation density $\delta(nm)^{-2} X\ 10^{-4}$	4.68	13.9	7.65	23.15	8.26	15.75	5.22

Scherrer Method directly calculates crystallite size using the Debye-Scherrer equation (3). Depends on the phenomenon of peak broadening observed in the X-ray diffraction (XRD) pattern. Results for crystallite sizes are typically higher than those obtained by the Scherrer Plot method, as shown in the table **V.2**.

Scherrer Plot Method more refined approach that takes into account the systematic distribution of errors across multiple peaks in XRD data. Smaller crystallite sizes correspond to higher dislocation densities, indicating greater imperfections in the crystal structure. Larger crystallite sizes correlate with lower δ, reflecting better crystalline quality. The additives have a decisive influence on the grain size and the overall quality of the ZnO thin films. In particular, PEG and BD contribute to an increased number of defects, while EDTA and EG promote the development of better crystalline structures.

V.2.2.Sr-doped ZnO thin films EDS analysis patterns and morphological

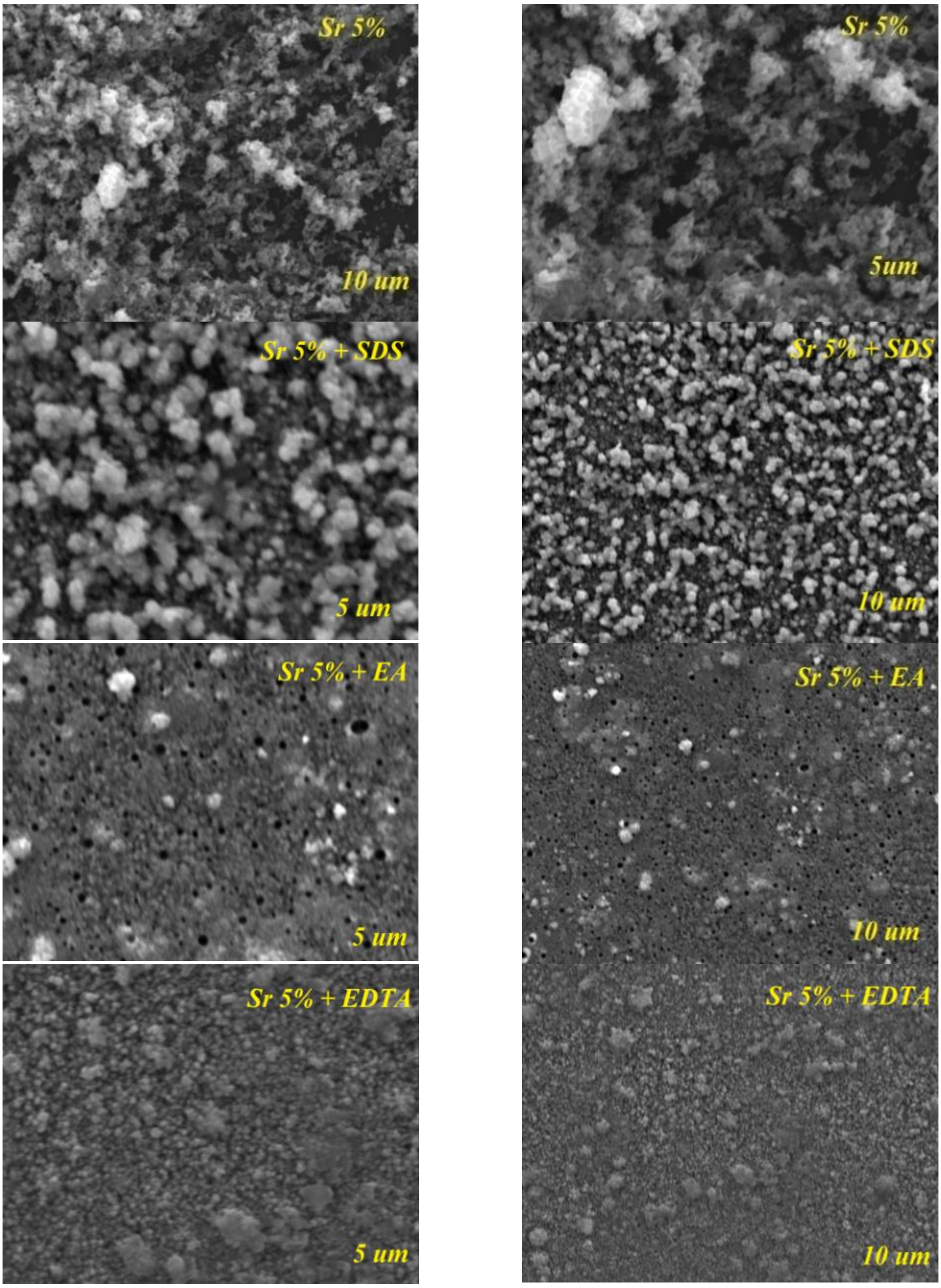

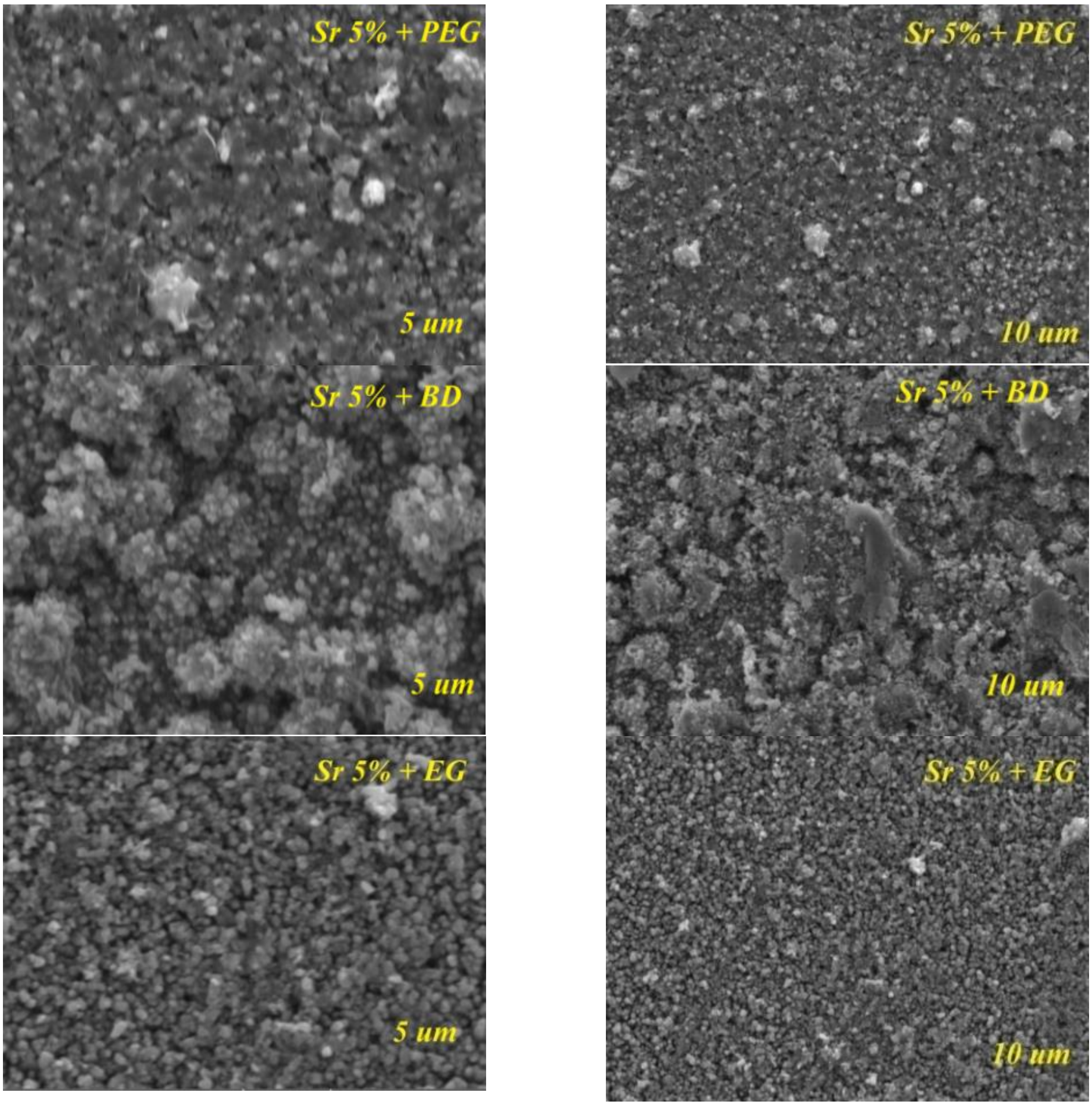

Figure **V.3.** SEM analyses of Sr/ZnO 5 wt.% based thin films at different additives.

The surface morphology of the Sr-doped ZnO thin films calcined at 450 °C was analyzed using Scanning Electron Microscopy (SEM), as shown in Figure **V.3**.The thin films exhibit a granular structure with particles of varying sizes. This suggests that the growth process may have involved nucleation and growth of multiple grains. In the instance of the specimen devoid of any additives, the resulting film exhibits a comparatively dense, agglomerated, and heterogeneous visual characteristic [21].When the EDTA sample, the surface morphological characterized by an combination of diminutive and intermediate-sized grains. The EA sample, it is noteworthy that the morphological characteristics exhibited a structure characterized by the presence of nanograins of a porous nature. Porous EA thin films exhibit favourable properties for photocatalytic applications, as shown by the results related to the degradation of

MB [22].In the case of EG and BD, it consisted of mixed. We also notice a large grain size in the SDS sample, which is consistent with the XRD results. Finally, for the PEG sample, do not observe small grains and pores granular like particles.

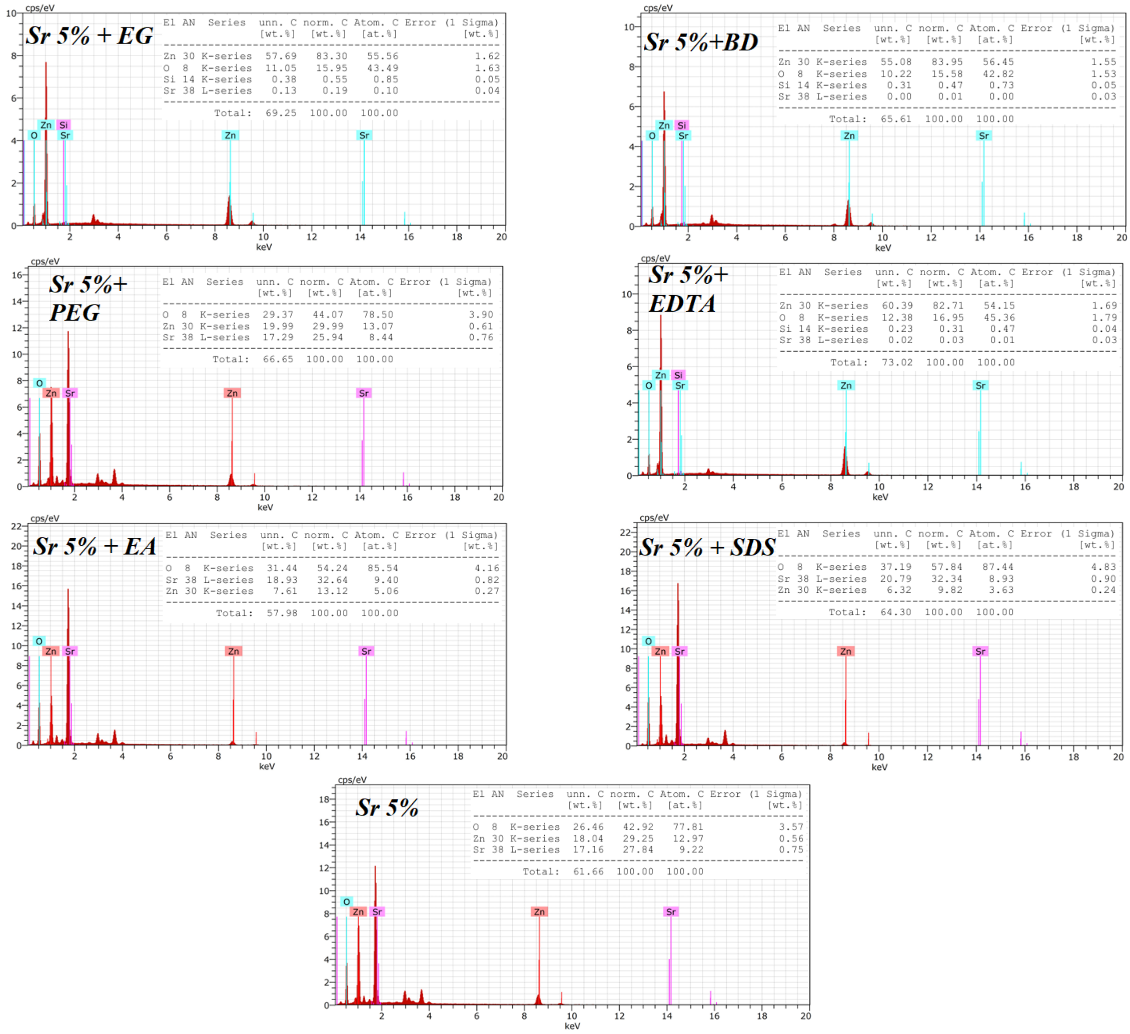

```
El AN  Series   unn. C norm. C Atom. C Error (1 Sigma)
                [wt.%]  [wt.%]  [at.%]          [wt.%]
------------------------------------------------------
Zn 30 K-series  57.69   83.30   55.56             1.62
O  8  K-series  11.05   15.95   43.49             1.63
Si 14 K-series   0.38    0.55    0.85             0.05
Sr 38 L-series   0.13    0.19    0.10             0.04
------------------------------------------------------
        Total:  69.25  100.00  100.00
```

```
El AN  Series   unn. C norm. C Atom. C Error (1 Sigma)
                [wt.%]  [wt.%]  [at.%]          [wt.%]
------------------------------------------------------
Zn 30 K-series  55.08   83.95   56.45             1.55
O  8  K-series  10.22   15.58   42.82             1.53
Si 14 K-series   0.31    0.47    0.73             0.05
Sr 38 L-series   0.00    0.01    0.00             0.03
------------------------------------------------------
        Total:  65.61  100.00  100.00
```

```
El AN  Series   unn. C norm. C Atom. C Error (1 Sigma)
                [wt.%]  [wt.%]  [at.%]          [wt.%]
------------------------------------------------------
O  8  K-series  29.37   44.07   78.50             3.90
Zn 30 K-series  19.99   29.99   13.07             0.61
Sr 38 L-series  17.29   25.94    8.44             0.76
------------------------------------------------------
        Total:  66.65  100.00  100.00
```

```
El AN  Series   unn. C norm. C Atom. C Error (1 Sigma)
                [wt.%]  [wt.%]  [at.%]          [wt.%]
------------------------------------------------------
Zn 30 K-series  60.39   82.71   54.15             1.69
O  8  K-series  12.38   16.95   45.36             1.79
Si 14 K-series   0.23    0.31    0.47             0.04
Sr 38 L-series   0.02    0.03    0.01             0.03
------------------------------------------------------
        Total:  73.02  100.00  100.00
```

```
El AN  Series   unn. C norm. C Atom. C Error (1 Sigma)
                [wt.%]  [wt.%]  [at.%]          [wt.%]
------------------------------------------------------
O  8  K-series  31.44   54.24   85.54             4.16
Sr 38 L-series  18.93   32.64    9.40             0.82
Zn 30 K-series   7.61   13.12    5.06             0.27
------------------------------------------------------
        Total:  57.98  100.00  100.00
```

```
El AN  Series   unn. C norm. C Atom. C Error (1 Sigma)
                [wt.%]  [wt.%]  [at.%]          [wt.%]
------------------------------------------------------
O  8  K-series  37.19   57.84   87.44             4.83
Sr 38 L-series  20.79   32.34    8.93             0.90
Zn 30 K-series   6.32    9.82    3.63             0.24
------------------------------------------------------
        Total:  64.30  100.00  100.00
```

```
El AN  Series   unn. C norm. C Atom. C Error (1 Sigma)
                [wt.%]  [wt.%]  [at.%]          [wt.%]
------------------------------------------------------
O  8  K-series  26.46   42.92   77.81             3.57
Zn 30 K-series  18.04   29.25   12.97             0.56
Sr 38 L-series  17.16   27.84    9.22             0.75
------------------------------------------------------
        Total:  61.66  100.00  100.00
```

Figure V.4. EDS analyses of Sr/ZnO 5 wt.% based thin films at different additives.

The elemental compositions of all samples were subjected to quantitative analysis utilizing energy dispersive spectroscopy (EDS) measurements. The resulting spectra reveal the predominance of Zn, Sr, and O as the principal elements, accompanied by elemental mapping. The inset of (**Fig V.4**) illustrates the quantitative weight percentages (wt%) of the compositional elements, specifically Zn, Sr, and O, present in all samples . The absence of other elemental traces within the spectrum further substantiates the samples' purity.

V.2.3.Study of 3D surface topography

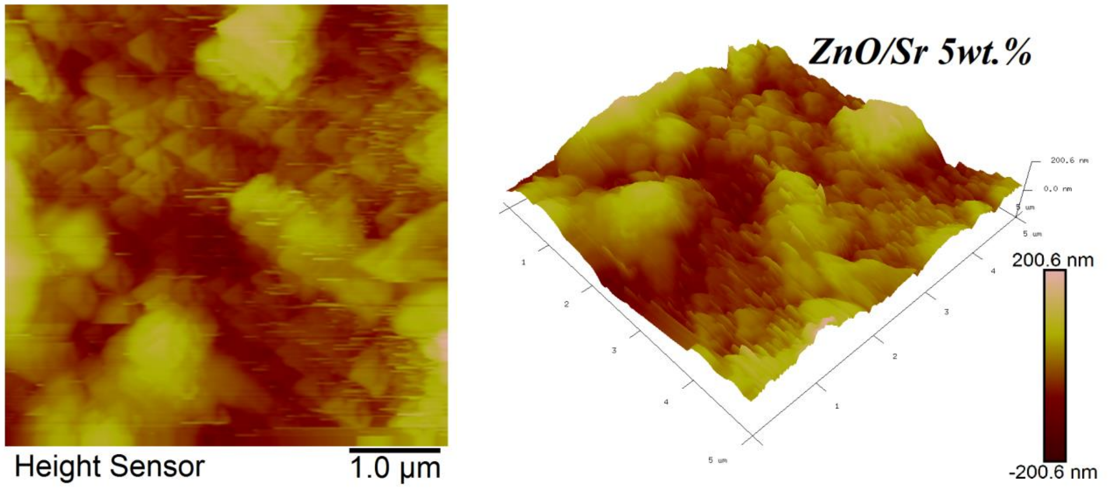

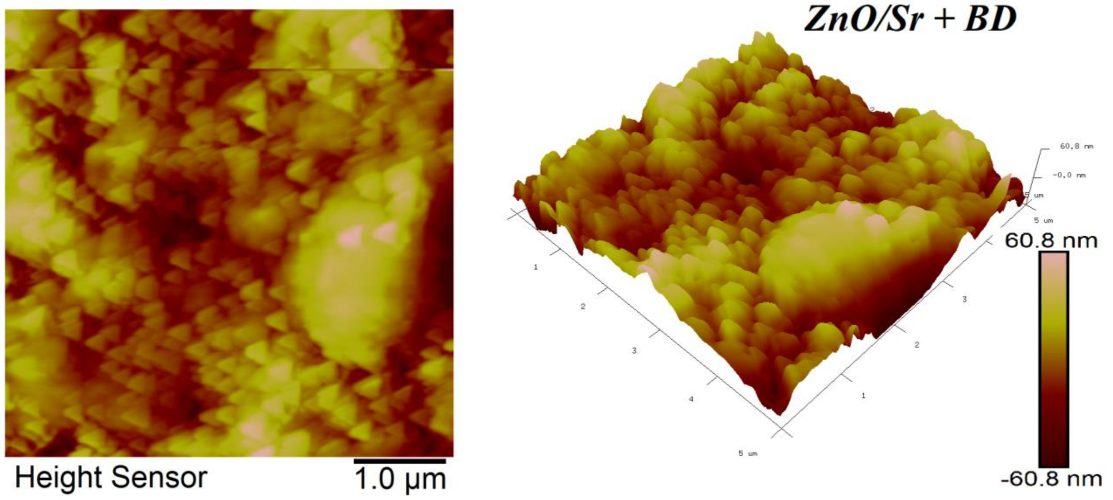

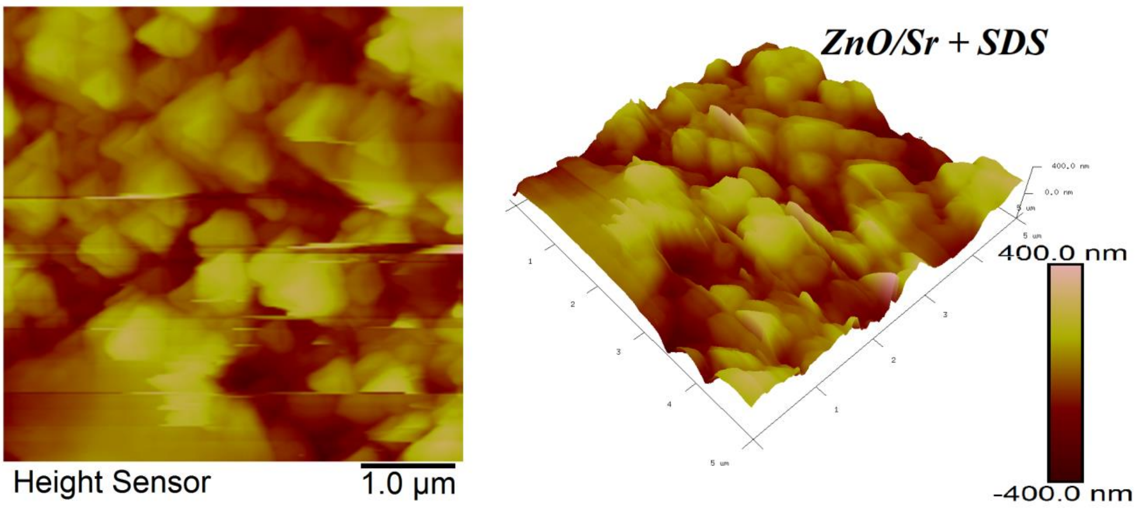

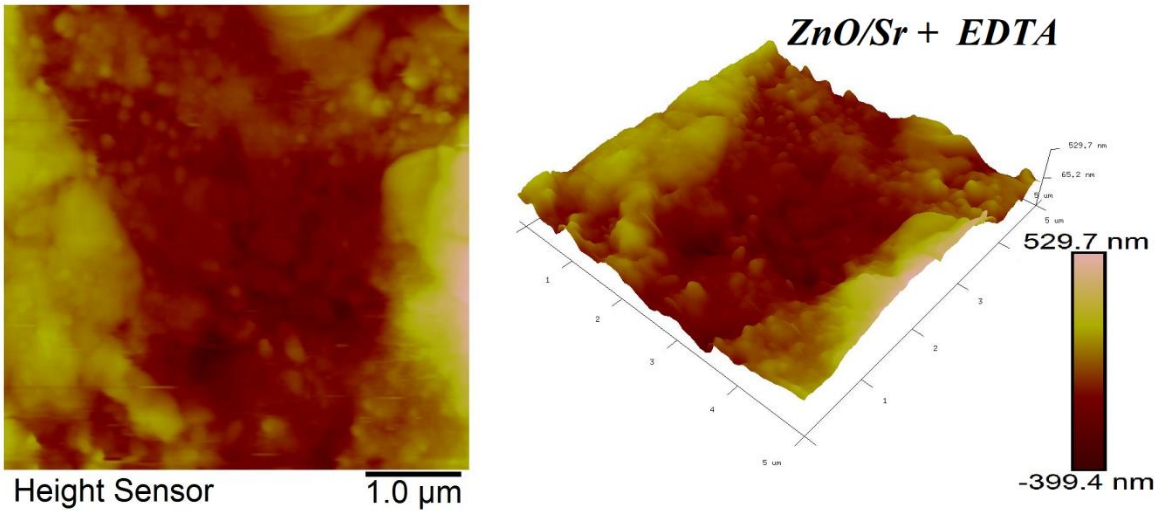
ZnO/Sr + EDTA
Height Sensor
1.0 µm
529.7 nm
65.2 nm
5 um
1
2
3
4
529.7 nm
-399.4 nm

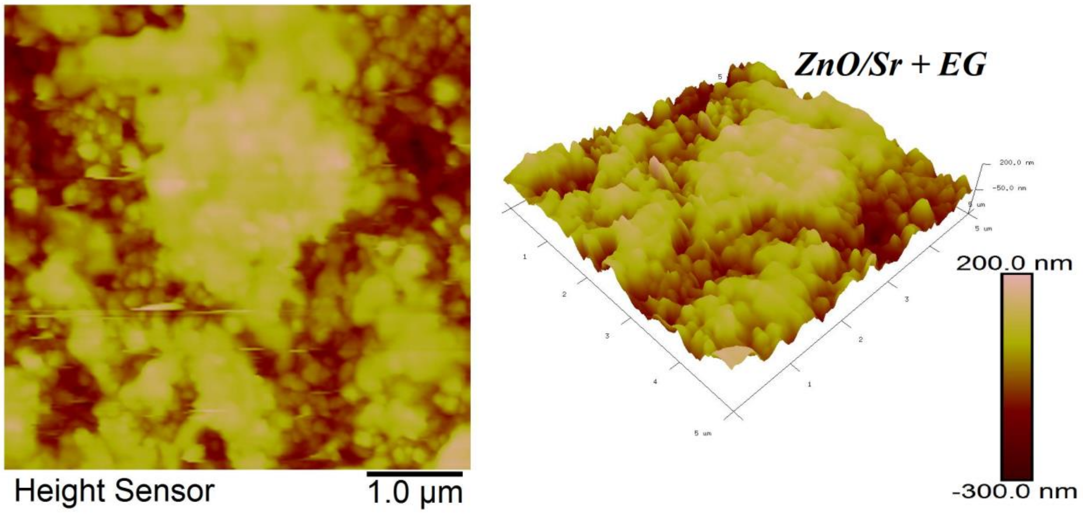
ZnO/Sr + EG
Height Sensor
1.0 µm
200.0 nm
-50.0 nm
5 um
1
2
3
4
200.0 nm
-300.0 nm

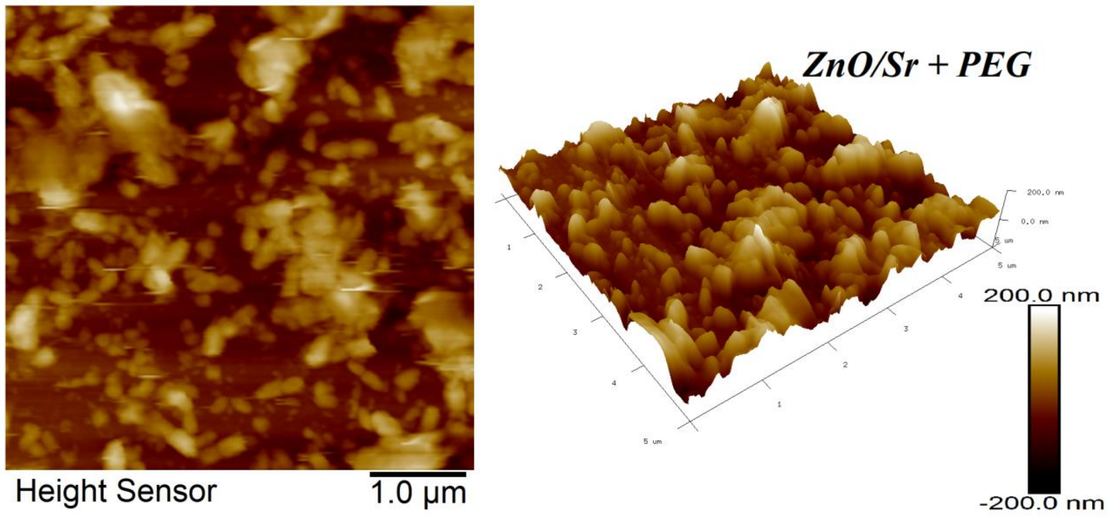
ZnO/Sr + PEG
Height Sensor
1.0 µm
200.0 nm
0.0 nm
5 um
1
2
3
4
200.0 nm
-200.0 nm

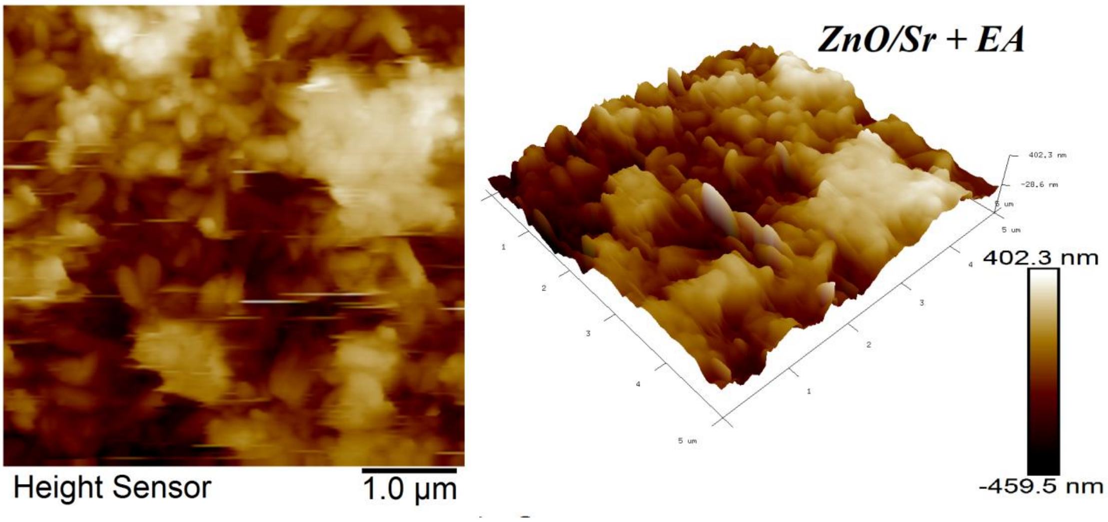

Figure V.5. AFM images (3D and 2D) of Sr/ZnO 5 wt.% based thin filmsat different additives.

Figure **V.5** of the atomic force microscopy (AFM) images of ZnO/Sr thin films with different additives, which were produced using the SILAR method, show clear differences in the surface morphology. For the sample with PEG, the surface exhibits a densely packed granular structure with uniform distribution, indicating effective grain growth and minimal voids. The EA modified thin film shows a similar dense structure, but with slightly larger grains, indicating that EA promotes coalescence of the grains during film formation. However, the thin film with EDTA shows a less uniform surface with significant agglomeration, suggesting that EDTA hinder homogeneous nucleation and growth processes. In contrast, the additive EG leads to a relatively smoother surface with smaller grains, reflecting its influence on limiting the grain size.

Table V.3. The estimated values of the root mean square (Rq), average roughness (Ra), contact angle (ϑ°) and film thickness for ZnO/Sr thin films at different additives:

Samples	***Root Mean Square Rq (nm)***	***Average Roughness (Ra) (nm)***	***contact angle (ϑ°)***	***Film thickness (nm)***
ZnO/Sr 5%	49.1	39.5	73.84	105.68
ZnO/Sr 5% + EA	128	107	50.05	330.64
ZnO/Sr 5% + EDTA	137	112	80.25	287.65
ZnO/Sr 5% + EG	78.7	65.2	94.13	200.50
ZnO/Sr 5% + PEG	50.5	41.7	58.43	219.11
ZnO/Sr 5% + SDS	110	88.5	78.84	240.39
ZnO/Sr 5% + BD	20.0	15.6	73.16	208.08

Table **V.3** contains quantitative data on the surface properties of Sr-doped ZnO thin films prepared with various additives. The values for the root mean square roughness (Rq) and the average roughness (Ra) illustrate the significant differences in surface morphology depending on the additive. The ZnO/Sr 5% + EDTA sample exhibits the highest roughness, with Rq and Ra values of 137 nm and 112 nm, respectively, indicating a highly textured surface. The ZnO/Sr 5% + EA sample also shows increased roughness values (Rq = 128 nm, Ra = 107 nm), indicating significant surface irregularities. In contrast, the ZnO/Sr 5% + EG sample exhibits much smoother surfaces. These differences in roughness also correlate with contact angle measurements, where smoother surfaces such as ZnO/Sr 5% + EG exhibits moderate hydrophilicity with contact angle of 94.13°.

In contrast, polyethylene glycol (PEG) and butyne-diol (BD) yield smoother films (Rq = 50.5 nm and 20.0 nm, Ra = 41.7 nm and 15.6 nm, respectively) with contact angles of 58.43° and 73.16°, suggesting improved wettability compared to rougher films. Sodium dodecyl sulfate (SDS) produces intermediate roughness (Rq = 110 nm, Ra = 88.5 nm) with a corresponding contact angle of 78.84°, showing a balance between hydrophilicity and hydrophobicity. These results highlight the critical role of surface roughness in determining the wettability of ZnO/Sr thin films, with smoother surfaces generally promoting hydrophilicity and rougher surfaces leading to increased hydrophobicity.

V.2.4.Analysis of contact angles

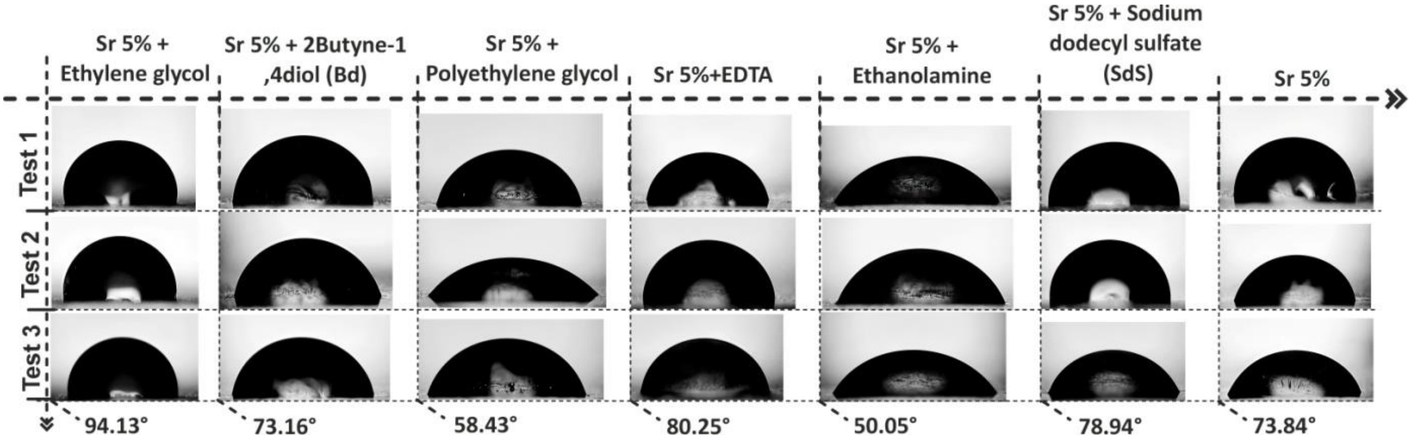

Figure V.6. The mean contact angle measurements of water droplets on Sr-doped ZnO thin films at different additives.

Figure **V.6** shows that Ethanolamine yields the most hydrophilic surface with a contact angle of (50.05°). This indicates that ethanolamine promotes strong surface wetting, possibly due to its chemical interaction with the ZnO film surface, leading to increased surface energy. Polyethylene glycol (PEG) also shows a good hydrophilic nature (58.43°), suggesting its role in producing a smooth and wettable surface. The surfaces with BD (73.16°), EDTA (80.25°), and SDS (78.94°) show moderate hydrophilicity. The most hydrophobic surface is produced with ethylene glycol (EG), which has a contact angle of 94.13°. This indicates lower surface energy, likely due to the properties of ethylene glycol during synthesis. Additives like ethanolamine and PEG promote hydrophilicity, which can enhance applications requiring water affinity, such as photocatalysis or sensors this is shown by the results of photocatalytic stimulation.

V.2.5. Optical properties

V.2.5.1. Transmittance

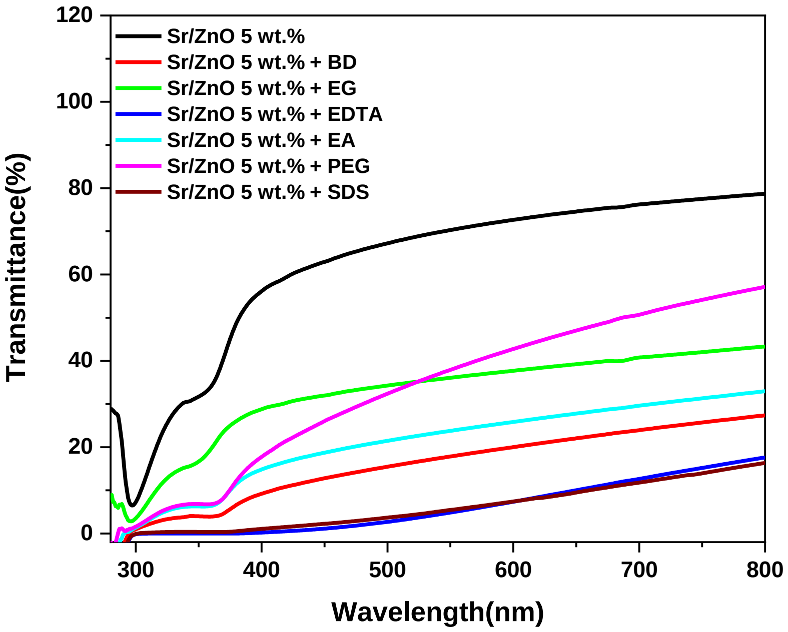

Figure V.7. Optical transmission spectra of the Sr-doped ZnO thin films.

The transmittance shows a gradual increase with increasing wavelength for each sample analyzed. At higher wavelengths (above 500 nm), the transmittance stabilizes for all films. Below approx. 400 nm, clear fluctuations can be seen, which indicates a different optical absorption behavior that depends on the additive used. PEG exhibits the most significant transmittance across the spectrum, particularly at extended wavelengths greater than 600 nm. This observation suggests that PEG enables improved optical clarity in the Sr-doped ZnO thin films. This is due to the lower thickness of this film and the smaller particle size [15]. EG films have a moderate light transmission, which indicates that EG influences the microstructure of the film to enable sufficient transparency. EA films display moderate transmittance but are visibly lower than EG and PEG. This suggests that EA results in less optical clarity, likely due to denser film morphology or scattering effects, as we observe in the SEM results the presence of a porous structure. BD films show lower transmittance compared to the other additives, particularly noticeable at longer wavelengths. EDTA and SDS films show the lowest transmittance across all wavelengths this indicates a more opaque film structure, likely caused by poor dispersion or particle aggregation.

V.2.5.2. Band gap

Figure **V.8** shows the band gap energy plots for Sr-doped ZnO thin films with different additives using Tauc's law. An increase in the band gap in combination with a certain additive could indicate a reduction in the defect states or an improvement in crystallinity. Conversely, a decrease in the band gap may indicate the occurrence of defect states or an increase in structural disorder.

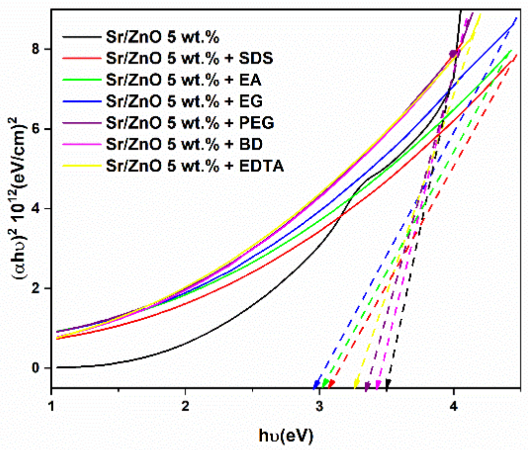

Figure V.8. Band gap energy plots for the Sr-doped ZnO thin films using Tauc’s law.

Additives such as SDS and EA can act as surfactants, thereby attenuating defects (including oxygen vacancies or zinc interstitials) in the film. The improved crystallinity reduces the defect states in the center of the band gap, resulting in an extended band gap. As a chelating agent, EDTA can complex with metal ions (Zn or Sr) during film preparation, which reduces defects and ensures an even distribution of the dopants. Reduced defects lead to a reduction in the band gap to 3.26 eV (**table V.5**). Additives such as EA can influence the grain size by controlling the growth rate of the ZnO crystals during deposition. Smaller grains can lead to quantum confinement effects that slightly increase the band gap. Organic additives BD can passivate surface defects, reducing electronic states within the band gap, which in turn deacrease the absorption edge and increases band gap to 3.43 eV. Additives generally reduce the band gap which indicates variations among additives indicate their differing efficiencies in defect passivation, crystal growth modification, and chemical interactions [23].

V.2.6.Photocatalytic for MB and AMX degradation

The degradation of methylene blue and antibiotic during the test period is primarily influenced by the increase in UV radiation and temperature. Fluctuations in humidity and wind speed can play an additional role. The increased ultraviolet radiation observed from the third hour onwards implies that the degradation efficiency probably peaked in the last hours of the experiment. As shown in the **tableV.4**.

Table V.4. Change in temperature, wind, humidity and solar radiation per hour in the MB and AB degradation test (Biskra, Algeria) on14 January, 2024:

Time (hr)	***1***	***2***	***3***	***4***	***5***
Wind speed (Km/h)	6	6	2	7	6
Temperature (c°)	12	12	14	14	16
Humidity (%)	50	50	37	47	41
Radiation amount (ultraviolet index)	0.99	0.99	1.86	2.42	2.7

The table **V.5** shows photocatalytic decomposition of methylene blue (MB) and the antibiotic amoxicillin using sunlight and thin films of ZnO/Sr 5 wt.% is enhanced by the addition of various additives. From the table we can see that with the addition of different additives, it effectively reduces the band gap, which enhances the absorption of visible light and increases the photocatalytic efficiency. When exposed to sunlight, photons provide energy to excite electrons from the valence band (VB) to the conduction band (CB) in the photocatalyst, leaving behind positively charged holes (h^+) in the VB. This process initiates the generation of charge carriers that drive photocatalytic reactions. In strontium-doped zinc oxide (ZnO/Sr) thin films, the photogenerated electrons (e^-) in the CB interact with molecular oxygen (O_2) adsorbed on the photocatalyst's surface, leading to the formation of reactive superoxide radicals (O_2^-). Simultaneously, the holes (h^+) in the VB oxidize water (H_2O) molecules or hydroxide ions (OH^-) to generate highly reactive hydroxyl radicals (•OH). These reactive oxygen species (ROS), including •OH and O_2^-, exhibit strong oxidative properties, enabling them to degrade complex organic pollutants such as methylene blue (MB) and amoxicillin (AMX) into smaller, non-toxic intermediates. Ultimately, these intermediates are mineralized into carbon dioxide (CO_2) and water (H_2O), completing the degradation process. The over all reactions can be summarized as follows:

$$ZnO{:}Sr + h\nu \rightarrow \mathrm{e}^- + \mathrm{h}^+ \tag{06}$$

$$\mathrm{e}^- + O_2 \rightarrow \mathrm{O}_2^- \tag{07}$$

$$h^+ + H_2O \rightarrow \bullet\,\mathrm{OH} + \mathrm{H}^+ \tag{08}$$

$$h^+ + OH^- \rightarrow \bullet\,\mathrm{OH} \tag{09}$$

$$\bullet\, OH + MB\ or\ AB \rightarrow CO_2 + H_2O + intermediates \tag{10}$$

The efficiency of this photocatalytic process depends significantly on the electronic and surface properties of the photocatalyst, which can be tuned by incorporating additives. For instance, the addition of ethylenediaminetetraacetic acid (EDTA) reduces the bandgap energy (Eg) of the ZnO/Sr thin films to approximately 3.26 eV, enhancing their ability to absorb visible light. This bandgap narrowing improves photocatalytic efficiency by suppressing the recombination of photogenerated electrons and holes, resulting in a higher production of ROS and increasing the degradation efficiency of amoxicillin to 23.68%.

Other additives, such as ethylene amine (EA) and sodium dodecyl sulfate (SDS), contribute to enhanced photocatalytic performance through mechanisms such as promoting ROS generation or modifying the surface activity of the photocatalyst. Conversely, additives like polyethylene glycol (PEG) and ethylene glycol (EG) provide stability to the photocatalyst but exhibit lower antibiotic degradation efficiencies due to limited contributions to ROS production or electron-hole separation.

Table V.5. Photocatalytic degradation efficiency of MB and AB, bandgap (Eg) and pseudo-first-order rate constant (R^2) for ZnO/Sr thin films at different additives:

Samples	*Efficiency 'η' (%) MB*	*R^2*	*Efficiency 'η' (%) AB*	*R^2*	*Bandgap (Eg) (eV)*
ZnO/Sr 5%	90.60	0.986	10.75	0.944	3.49
ZnO/Sr 5% + EA	92.53	0.982	13.67	0.969	3.02
ZnO/Sr 5% + EDTA	90.78	0.991	23.68	0.948	3.26
ZnO/Sr 5% + EG	88.94	0.999	12.38	0.750	2.94
ZnO/Sr 5% + PEG	88.85	0.999	10.81	0.791	3.34
ZnO/Sr 5% + SDS	87.77	0.980	14.75	0.991	3.07
ZnO/Sr 5% + BD	91.17	0.999	14.28	0.884	3.43

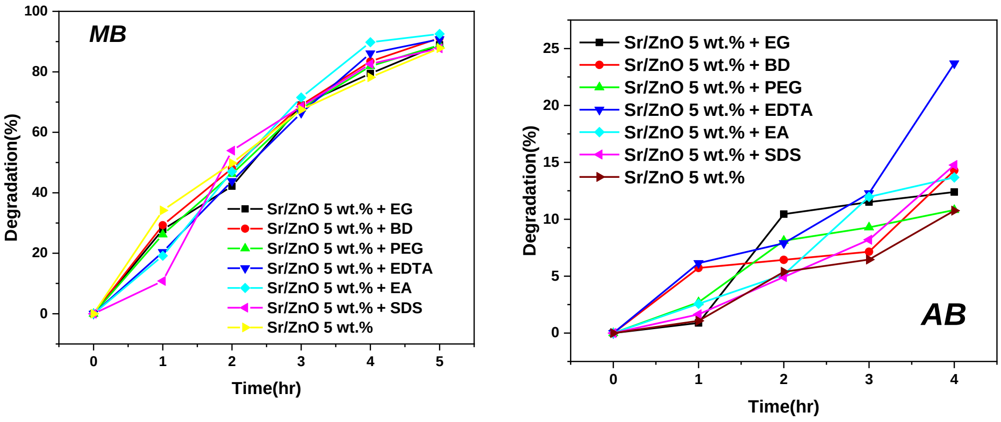

Figure V.9. The degradation efficiency of methylene blue (MB) and the antibiotic amoxicillin (AB) with ZnO/Sr 5 wt.% thin films modified with various additives.

For MB degradation, the efficiency approaches near-complete degradation (~90%) within 4-5 hours across all additives. The consistent performance is attributed to MB's relatively simpler molecular structure, which is more susceptible to oxidation by ROS like hydroxyl radicals ($\bullet OH$) and superoxide anions (O^{2-}) generated during photocatalysis. The differences between additives, though minimal, indicate varying levels of ROS generation and adsorption effects.

For AB degradation, a more complex and resistant organic molecule, the degradation efficiency is significantly lower (10-25%), with EDTA showing the highest yield. This is due to EDTA's ability to chelate metal ions, enhancing charge carrier separation and increasing ROS availability. Other additives such as SDS and BD also show improved yields due to their surface-modifying properties, facilitating better interaction between AB molecules and ROS. Factors such as molecular complexity, ROS reactivity, and catalyst surface area contribute to the slower degradation rate of AB compared to MB.

V.2.6.1. kinetic

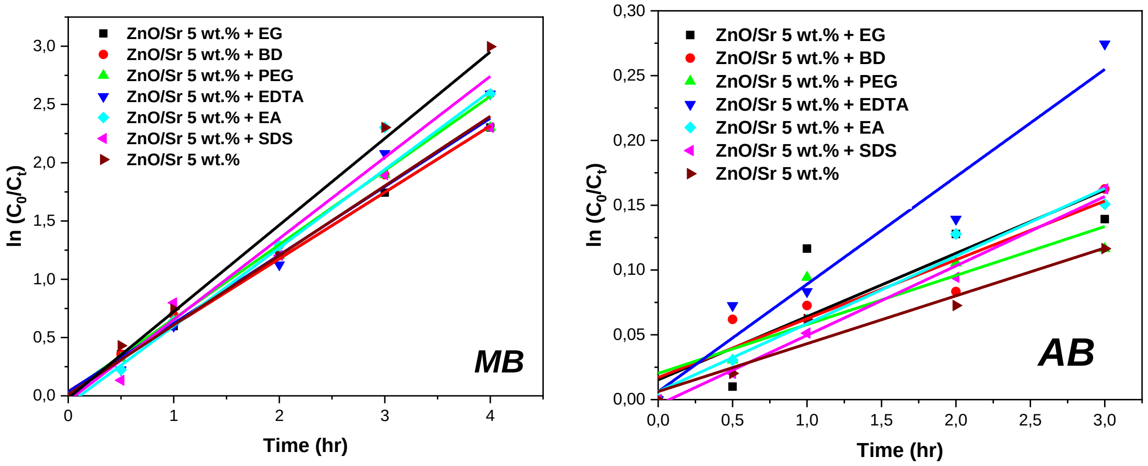

Figure V.10. Pseudo-first-order kinetic plot of ln(C_0/C_t) vs. time of (MB) Methylene Blue; (AB) Antibiotic degradation in the presence of Sr-doped ZnO 5 wt.% thin films at different additives.

Figure **V.10** illustrates the pseudo-first-order kinetic plots for the photocatalytic degradation of methylene blue (MB) and antibiotics (AB) using 5 wt% strontium-doped zinc oxide (ZnO/Sr) thin films in the presence of various additives. The linear relationship between $\ln(C_0/C_t)$ and time for both MB and AB degradation confirms that the degradation follows a pseudo-first-order kinetic model, as described by the Langmuir-Hinshelwood mechanism. The kinetic plots reveal that the photocatalytic performance of the ZnO/Sr thin films varies significantly with the type of additive employed.

For methylene blue degradation (MB plot), the film modified with ethylene glycol (EG) shows the highest slope, indicating the fastest degradation rate. Similarly, additives such as

BD and EA also exhibit relatively high degradation rates, as evidenced by their steeper slopes compared to films modified with polyethylene glycol (PEG) or sodium dodecyl sulfate (SDS). The unmodified ZnO/Sr film demonstrates the lowest slope, suggesting the slowest degradation rate for MB in the absence of additives.

For antibiotic degradation (AMX plot), the trends are consistent with those observed for MB. Additives like EDTA and EA enhance the photocatalytic degradation efficiency significantly, resulting in steeper slopes compared to PEG or SDS. The unmodified ZnO/Sr film again shows the least efficient degradation performance. This variation in performance can be attributed to the role of additives in modifying the surface properties, bandgap energy, and charge carrier dynamics of the ZnO/Sr films, thereby influencing the production of reactive oxygen species (ROS) and the overall degradation kinetics.

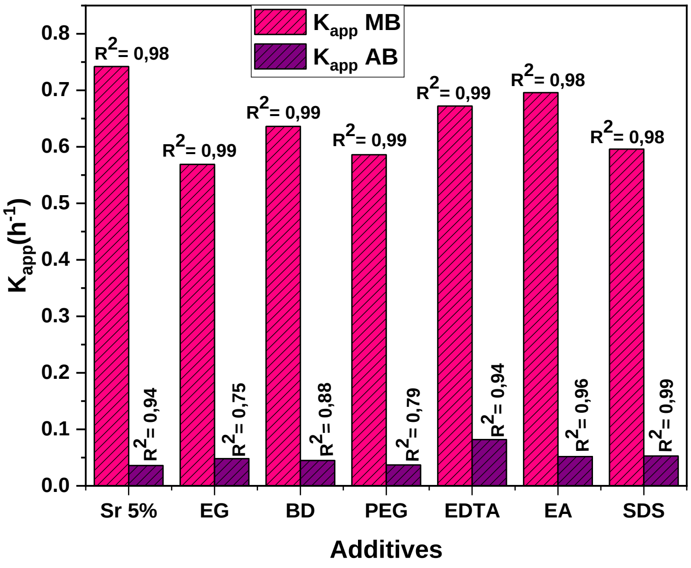

Figure V.11. Reaction rate constants and R^2 values of kinetic data of pseudo-first-order model for MB, RB on Sr-doped ZnO 5wt.%.

The figure **V.11** shows highlights the variation in k_{app} values for MB and AB at different additives. For MB, k_{app} is highest for ZnO/Sr + EA, demonstrating efficient photocatalytic activity due to enhanced electron-hole separation and the generation of reactive oxygen species (ROS). For AB, k_{app} is maximized with EDTA, likely due to its strong chelating properties and ability to suppress recombination of photogenerated charge carriers. Additives such as SDS and BD also improve *k*app by modifying surface properties and increasing ROS production. The high R^2 values (>0.98) confirm a good fit to pseudo-first-order kinetics, validating the reliability of the kinetic model. The results indicate that the choice of additive significantly impacts the degradation kinetics by enhancing visible light absorption, improving ROS generation, and optimizing the photocatalytic process.

V.2.6.1. Langmuir isotherm

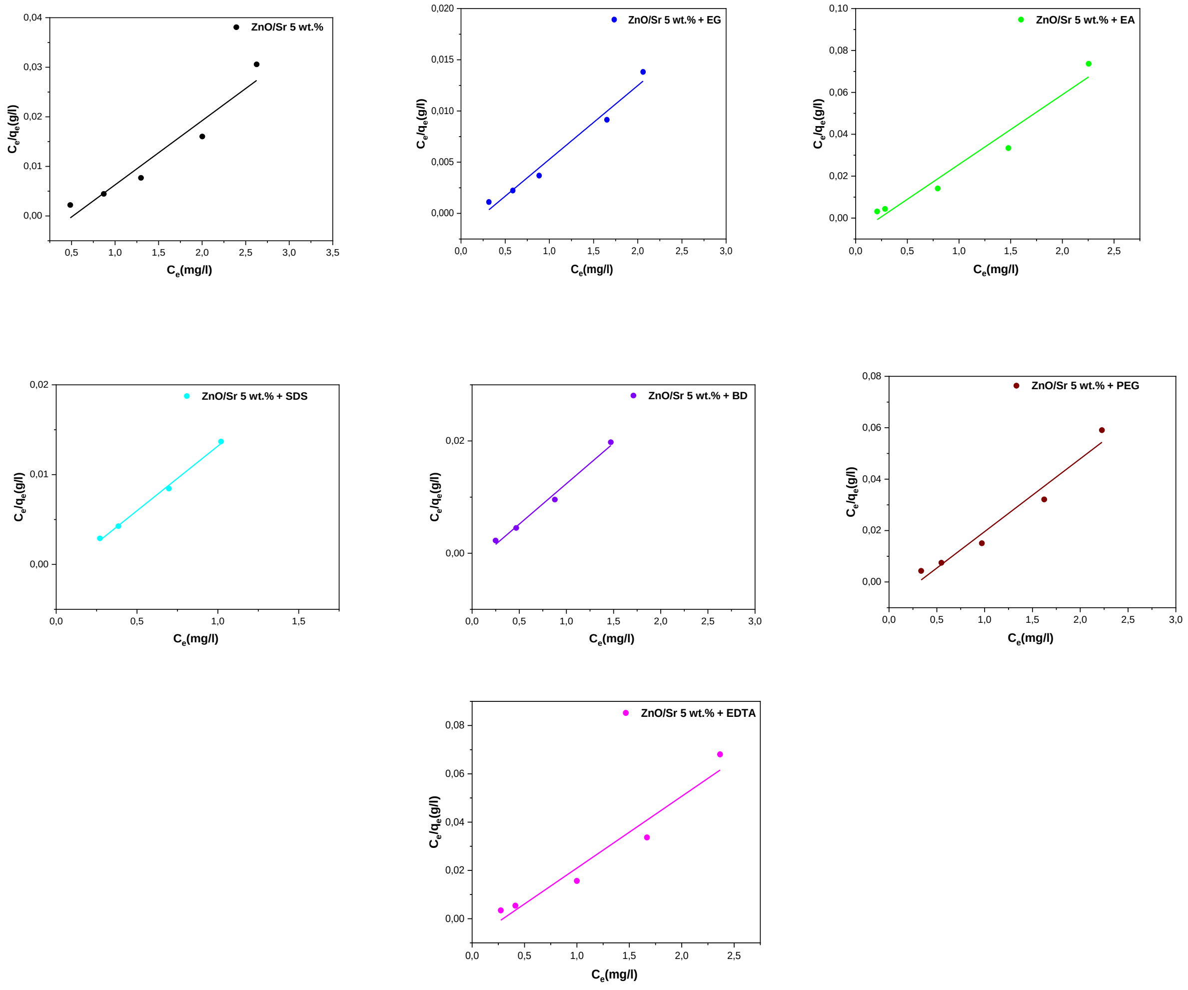

Figure V.12. Linear form of the Langmuir model of methylene blue on the Sr-doped ZnO 5wt.% thin films at different additives.

The Figure **V.12** represents the linear Langmuir isotherm model for the adsorption of methylene blue on Sr-doped ZnO thin films (5 wt.%) with different additives. Each subplot corresponds to a specific additive, as indicated in the legends, and shows a linear relationship between C_e/q_e (g/l) and C_e (mg/L), where C_e is the equilibrium concentration of methylene blue in solution, and q_e is the amount adsorbed per unit weight of the adsorbent.

The Langmuir model assumes monolayer adsorption on a homogeneous surface with finite adsorption sites. The linear fit provides key parameters such as the adsorption capacity (q_{max}) and the Langmuir constant (K_L), which are derived from the slope and intercept of the plots. The addition of different additives influences the adsorption efficiency by changing the surface properties of the adsorbent. The linear character of the diagrams shows that the Langmuir model is suitable for describing the adsorption process under these conditions. The different slopes and intersections between the plots indicate that each additive has a significant effect on the adsorption capacity and affinity for methylene blue.

Table V.6. Langmuir isotherm experimental constants for MB:

absorbent	***Equation (y=)***	***R^2***	***q_{max}(mg/g)***	***K_L(L/mg)***	***S_{MB}(10^{-20}km^2/kg)***
ZnO/Sr 5%	*0.012 x + 0.006*	0.936	77.51	1.95	0.246
ZnO/Sr 5% +EA	*0.007 x + 0.001*	0.976	138.88	3.78	0.440
ZnO/Sr 5% +EDTA	*0.029 x + 0.008*	0.950	33.67	3.41	0.106
ZnO/Sr 5% + EG	*0.033 x + 0.007*	0.957	30.03	4.32	0.095
ZnO/Sr 5% +PEG	*0.028 x + 0.008*	0.963	35.33	3.25	0.112
ZnO/Sr 5% +SDS	*0.014 x + 0.001*	0.996	69.93	11.91	0.222
ZnO/Sr 5% +BD	*0.014 x + 0.002*	0.988	69.44	7.20	0.220

The table **V.6** presents the parameters obtained from the linear Langmuir isotherm model for the adsorption of methylene blue on Sr-doped ZnO thin films (5 wt.%) with and without various additives. The Langmuir equation, represented as y= a*x*+b, describes the linear relationship between C_e/q_e and C_e. The regression coefficient (R^2) indicates the goodness of fit, with values close to 1 confirming the model's applicability.

The maximum adsorption capacity (q_{max}) and the Langmuir constant (K_L) are derived from the slope and intercept. The results show that the highest $q_{\max}$ (138.88 mg/g) is achieved with ethanolamine (EA), while the lowest (30.03 mg/g) occurs with ethylene glycol (EG), indicating significant variation in adsorption efficiency depending on the additive. The negative K_L values suggest limitations in adsorption affinity under the tested conditions. The specific surface area for methylene blue adsorption (S_{MB}) further highlights the variation, with EA yielding the highest value (0.440×10^{-20} km^2 /kg) and EG the lowest (0.095×10^{-20}). Overall, the additives strongly influence the adsorption behavior, likely due to modifications in the adsorbent's surface properties and interaction with the adsorbate.

V.3.Conclusion

This chapter presented a comprehensive analysis of the effects of various additives on the structural, morphological, optical, and photocatalytic properties of Sr-doped ZnO thin films synthesized via the Successive Ionic Layer Adsorption and Reaction (SILAR) method. The study highlights the critical role of additives, such as EA, EG, PEG, EDTA, SDS, and BD, in tailoring the thin films' properties for improved photocatalytic performance in the degradation of methylene blue and amoxicillin.

The structural analysis revealed that each additive significantly influenced the crystallinity and lattice parameters of the thin films. EDTA and EG additives promoted higher crystallinity with reduced dislocation densities, whereas PEG and BD introduced structural defects, resulting in smaller crystallite sizes and higher dislocation densities. These changes were evident in the XRD patterns and Scherrer analysis.

Morphological studies through SEM and AFM demonstrated distinct surface characteristics for each additive. The EA and EDTA samples exhibited porous and mixed grain structures, respectively, conducive to enhanced photocatalytic activity. In contrast, the PEG and BD samples showed smoother surfaces, leading to reduced hydrophilicity and moderate catalytic efficiency. These observations correlated with contact angle measurements, where EA exhibited the highest hydrophilicity (50.05°), and EG displayed the most hydrophobic surface (94.13°).

Optical characterization showed that additives like EDTA and EA effectively reduced the bandgap energy, enhancing visible light absorption and photocatalytic performance. The bandgap narrowing, combined with optimized surface properties, enabled efficient generation of reactive oxygen species (ROS), critical for the degradation of organic pollutants. Among the additives, EDTA achieved the highest AMX degradation efficiency (23.68%), while EA demonstrated superior MB degradation efficiency (92.53%).

The photocatalytic tests confirmed that the additives significantly impact electron-hole separation, ROS production, and degradation kinetics. Kinetic studies revealed that the photocatalytic degradation of MB and AMX followed pseudo-first-order kinetics, with additives like EDTA and EA exhibiting the highest rate constants. The Langmuir isotherm analysis further validated the role of additives in enhancing adsorption efficiency, particularly for EA, which achieved the highest adsorption capacity for MB (138.88 mg/g).

In conclusion, this study underscores the potential of Sr-doped ZnO thin films as versatile photocatalysts for environmental remediation. By strategically incorporating additives, the structural, morphological, and optical properties of the thin films can be fine-tuned to achieve superior photocatalytic performance. These findings pave the way for further research into optimizing additive combinations and exploring their applications in advanced water treatment technologies.

References of chapter V

[1] Sun, Yue, et al. "Preparations and applications of zinc oxide based photocatalytic materials." *Advanced Sensor and Energy Materials* (2023): 100069.

[2] Ayach, Jana, et al. "Comparing conventional and advanced approaches for heavy metal removal in wastewater treatment: an in-depth review emphasizing filter-based strategies." *Polymers* 16.14 (2024): 1959.

[3] Zhang, Qiyue. "Characteristics of Traditional and Emerging Water Treatment Technologies and Their Comparison." *Highlights in Science, Engineering and Technology* 83 (2024): 8-13.

[4] Wahba, Monier M., et al. "Treating polluted water with modern technologies." *Data Plus* 2.1 (2024): 13-21.

[5] Sayan, Bhattacharya, et al. "Role of nanotechnology in water treatment and purification: potential applications and implications." *Int J Chem Sci Technol* 3.3 (2013): 59.

[6] Hu, Anming, and Allen Apblett, eds. Nanotechnology for water treatment and purification. Book: Vol. 22. *Switzerland: Springer International Publishing*, 2014.

[7] Aydin, Didem, İlkayHilalGübbük, and Mustafa Ersöz. "Recent advances and applications of nanostructured membranes in water purification." *Turkish Journal of Chemistry* 48.1 (2024): 1-20.

[8] Pradeep, Verma, and Maulin P. Shah. "Clean Technologies Toward a Sustainable Future: Physicochemical, Biochemical and Biotechnological Approaches." (2023).

[9] Shukla, Bishnu Kant, et al. "Application of Nanomaterials in Water Purification: A Thematic Review." *International Conference on Water Technologies. Singapore: Springer Nature Singapore,* 2022.

[10] Javaid, Alqa Saeeda, et al. "Synthesis and characterization of efficient Sr-doped ZnO nanostructures for optoelectronic, and photocatalytic applications." *Inorganic Chemistry Communications* 162 (2024): 112175.

[11] Selvaraj, Saravanan, et al. "Effect of Sr doping in ZnO microspheres for solar light-driven photodegradation of organic pollutants." *Journal of Materials Science: Materials in Electronics* (2022): 1-12.

[12] Alsubaie, Modi Nasser, et al. "Ferroelectric-assisted enhancement of the photocatalytic activity of g-C3N4/TiO2 nanotubes heterojunctions through the addition of strontium." *Journal of Photochemistry and Photobiology A: Chemistry* 454 (2024): 115699.

[13] Rajasekar, S., et al. "Synthesis and characterization of cobalt-strontium co-doped zinc oxide nanoparticles by chemical precipitation." *Inorganic Chemistry Communications* 158 (2023): 111607.

[14] Chen, Haoxian, et al. "Effect of Sr doping on nonlinear current–voltage properties of ZnO-based ceramics." *Journal of Electronic Materials* 50.7 (2021): 4096-4103.

[15] Man-Lin, Tan, et al. "Optical characteristics of zinc oxide nanoparticles with surface modification using polyethylene glycol." *Journal of Inorganic Materials* 29.10 (2014): 1039-

1043.

[16] Akshata, G., and Santhosha Acharya. "Synthesis and characterization of undoped and strontium doped ZnO thin films." *Materials Today: Proceedings* 55 (2022): 109-112.

[17] Nadeem, Muhammad Shahid, et al. "Sr-doped ZnO thin film on a silicon substrate (100) grown by sol-gel method: Structural and optical study." *Optical Materials* 157 (2024): 116106.

[18] Ouhaibi, A., et al. "The effect of strontium doping on structural and morphological properties of ZnO nanofilms synthesized by ultrasonic spray pyrolysis method." *Journal of Science: Advanced Materials and Devices* 3.1 (2018): 29-36.

[19] Yarahmadi, Mohadeseh, et al. "Synthesis and characterization of Sr-doped ZnO nanoparticles for photocatalytic applications." *Journal of Alloys and Compounds* 853 (2021): 157000.

[20] Pujar, Swati, and Gowrish K. Rao. "Annealing induced strong NBE emission of SILAR deposited ZnO thin films." *Materials Today: Proceedings* 55 (2022): 56-61.

[21] Devi, K. Radhi, et al. "Enhanced room temperature ammonia gas sensing properties of strontium doped ZnO thin films by cost-effective SILAR method." *Materials Science in Semiconductor Processing* 119 (2020): 105117.

[22] Zheng, Gaige, et al. "Enhanced photocatalytic activity of ZnO thin films deriving from a porous structure." *Materials Letters* 150 (2015): 1-4.

[23] Anand, T. Joseph Sahaya, Mohd Zaidan, and S. Shariza. "Effect of additives on optical measurements of $NiSe_2$ thin films." *Procedia Engineering* 53 (2013): 555-561.

General Conclusion and Perspectives

The global water scarcity crisis arises from waste, pollution, and the uneven distribution of freshwater resources. Developing innovative, cost-effective, and efficient water purification methods is essential. Photocatalysis has recently emerged as an eco-friendly method for degrading organic pollutants in liquids and gases. Specifically, photocatalysts such as zinc oxide (ZnO) offer several advantages, including low cost, chemical and physical stability, and environmental friendliness. However, this promising platform faces challenges such as rapid recombination of photogenerated electron-hole pairs, limited visible-light responsiveness, and a low specific surface area.

To address these aspects, this Ph.D. study is divided into three distinct chapters. The first chapter examines the effect of small strontium concentrations on the structure of ZnO thin films for methylene blue degradation under sunlight. The second chapter involves the design of high concentrations of strontium-doped ZnO films using the SILAR process for photocatalytic applications involving methylene blue and rose Bengal. The final chapter investigates the effect of various chemical additives on 5% strontium-doped ZnO films. Each of these chapters is discussed separately as follows:

In the chapter III, pure ZnO and Sr-doped ZnO thin films were successfully synthesized and analyzed on glass substrates using the SILAR method. Comprehensive characterization, including X-ray diffraction, scanning electron microscopy, 3D surface topography analysis, and UV-visible spectroscopy, provided essential insights into the properties and performance of the films. XRD analysis confirmed the thin films' polycrystalline structure. Furthermore, Sr doping induced significant changes in surface morphology. Contact angle measurements with water droplets revealed that all Sr/ZnO thin films exhibited hydrophilic behavior, with contact angles ranging from 57.10° to 70.30°, whereas pure ZnO demonstrated hydrophobic properties. The primary objective of this study was to evaluate the photocatalytic performance of the films, particularly in degrading methylene blue (MB) under natural sunlight. Sr doping notably enhanced the photocatalytic activity, with the 5 wt.% Sr-doped ZnO sample achieving a remarkable 94.82% degradation rate in the first cycle. Additionally, this sample exhibited excellent stability and reusability, retaining its original photocatalytic efficiency over three consecutive cycles. This study highlights the potential of Sr-doped ZnO thin films for eco-friendly and efficient photocatalytic applications, especially in degrading organic pollutants under natural sunlight, providing sustainable solutions for water purification.

The chapter IV examines the photocatalytic activity of Sr-coupled ZnO thin films for coupled ZnO thin films were synthesized using the successive ion layer adsorption and reaction (SILAR) method, with high Sr concentrations. X-ray diffraction (XRD) analysis confirmed the crystalline structure of the films and showed a decrease in crystallite size with increasing Sr content. Scanning electron microscopy (SEM) revealed that pure ZnO displayed nanorod morphology, whereas Sr doping resulted in a mixed morphology comprising nanorods and spherical structures. UV-visible spectroscopy demonstrated that Sr doping reduced the bandgap of ZnO, thereby potentially enhancing its light absorption properties. The study compared the photocatalytic degradation efficiencies of MB and RB under sunlight irradiation using these catalysts and examined the influence of solution acidity and hole scavengers under simulated wastewater treatment conditions. Among the photocatalysts, the Sr40% sample achieved the highest degradation rates, with 89.62% for MB and 94.67% for RB under sunlight.

This research highlights the potential of ZnO as a photocatalyst for water purification, despite challenges such as rapid electron-hole recombination and limited visible-light absorption. The findings demonstrate that Sr doping effectively addresses these issues, significantly enhancing the photocatalytic performance of ZnO thin films for degrading organic dyes. These results contribute to the advancement of efficient photocatalysts for the removal of organic pollutants from water.

In last chapter, Sr-doped ZnO thin films were synthesized using the SILAR method with various additives, including EA, EG, PEG, EDTA, SDS, and BD. These additives serve as chelating agents, surfactants, solvents, or reducing agents and play a critical role in influencing the structural, morphological, and optical properties of the Sr-doped ZnO thin films. Additionally, they impact the films' photocatalytic performance in degrading methylene blue (MB) and amoxicillin (AMX).

Morphological analysis revealed distinct surface features for each additive. The EA sample exhibited a porous structure with nanograins, while the EDTA sample presented a mix of small and intermediate-sized grains. The EG and BD samples displayed a mixed grain morphology, and the SDS sample showed larger grains, consistent with XRD findings. In contrast, the PEG sample lacked small grains and pores, instead featuring granular, particle-like structures.

The EA (50.05°) and PEG (58.43°) samples exhibited the highest hydrophilicity due to increased surface energy, while the EG sample was the most hydrophobic (94.13°). EDTA produced the roughest surface (Rq = 137 nm, Ra = 112 nm), while PEG resulted in the smoothest surface (Rq = 50.5 nm, Ra = 41.7 nm), which facilitated uniform grain distribution. The correlation between roughness and hydrophilicity identified PEG and EA as optimal additives for applications requiring smooth, wettable surfaces.

Additives such as EDTA enhanced photocatalytic efficiency by lowering bandgap energy and suppressing charge carrier recombination, achieving 23.68% AMX degradation. EA and SDS improved activity by increasing ROS production or optimizing surface properties, while PEG and EG enhanced film stability but contributed less to photocatalysis. Notably, Sr-doped ZnO + EA films showed the highest photocatalytic efficiency for MB degradation (92.53%), whereas PEG exhibited the lowest efficiency for AMX degradation (10.81%).

Pure ZnO and Sr-doped ZnO thin films were synthesized using the SILAR method and thoroughly characterized to understand their structural, morphological, optical, wettability, and photocatalytic properties. X-ray diffraction analysis confirmed the polycrystalline structure of all thin films. Scanning electron microscopy showed that the rod-shaped grains increased in size at 3 wt.% Sr doping. The EA sample exhibited a porous structure characterized by the presence of nano-grains. The 7% Sr-doped sample was the most transparent, while the EA sample was the most hydrophilic, with the lowest contact angle of 50.05°. A comparative analysis of methylene blue (MB) degradation efficiencies across the samples highlighted the influence of Sr concentration and their corresponding performances. All samples yielded good results; the highest MB decomposition was achieved by the 5% Sr-doped sample, while the 40% Sr-doped sample achieved a yield of 97.6% in the basal medium. The EA sample performed well, with a yield of 92.53%. This sample had the most coarse, hydrophilic, and porous structure, with a band gap (Eg) of 2.65 eV.

This study underscores the stability and reusability of Sr-doped ZnO thin films, positioning them as excellent candidates for various scientific explorations. Additionally, there is significant potential to improve these films through diverse strategies, including leveraging experimental findings for simulations. The combination of Sr-doped ZnO with other materials, such as TiO_2 or carbon-based compounds, can form heterojunctions that enhance charge separation and boost photocatalytic efficiency. These composites can extend light absorption into the visible spectrum, enhancing their effectiveness under natural sunlight. Techniques like coating or functionalizing the surfaces of Sr-doped ZnO thin films can further enhance their stability and performance across multiple applications. This may involve the application of protective layers or the introduction of additional active sites for photocatalytic reactions. Fabricating Sr-doped ZnO into specific nanostructures (e.g., nanorods or nanoparticles) can improve surface area and light absorption, resulting in better photocatalytic activity. Methods such as chemical bath deposition or sol-gel techniques can be utilized to achieve the desired morphologies. By concentrating on these areas, the performance of strontium-doped zinc oxide thin films can be significantly improved, expanding their applicability in environmental remediation, energy harvesting, and sensing technologies.

Supplements

The present thesis is based on the following supplements:

1. Mokrani, N., Temam, E. G., Barkat, H., Temam, H. B., Rahmane, S., & Althamthami, M. (2024). Boosting photocatalytic stability: hydrophilic Sr-doped ZnO thin films prepared via the SILAR method for enhanced performance over multiple cycles. *Physica Scripta*, *99*(9), 0959a4.
2. Mokrani, N., Temam, E. G., Temam, H. B., Barkat, H., & Althamthami, M. (2025). Enhancing water purification with light-activated strontium-doped ZnO thin films. *Advances in Natural Sciences: Nanoscience and Nanotechnology*, *16*(1), 015012.

Parts of this work have been presented at the following conference:

1. Mokrani, N., Temam, E. G., Temam, H. B., Barkat, H. *Synthesis, structural evolution and wettability characterization of Sr-ZnO thin films prepared by SILAR method.* 1st International Seminar on chemical Process & Environment (ISCPE2022), Biskra.
2. Mokrani, N., Temam, E. G., Temam, H. B., Barkat, H. *Influence of Sr doping on the microstructure, morphology and optical properties of ZnO thin films prepared by SILAR method*. International Conferences on Science and Technology Engineering Science and Technology, 2023 Budva, Montenegro.
3. Mokrani, N., Temam, E. G., Temam, H. B., Barkat, H. *Photocatalytic Performance of Sr-coupled ZnO Thin Films Prepared by the SILAR Method. 8th International Conference on Mechanics and Energy,* Sousse, TUNISIA ICME'2023.
4. Mokrani, N., Temam, E. G., Temam, H. B., Barkat, H., & Althamthami, M. *Effect of different ZnO:Sr film concentrations on photocatalytic reactions Bangal rose: A study of film properties*. The first national conference on chemistry and life, Bashar 2024.
5. Mokrani, N., Temam, E. G., Temam, H. B., Barkat, H., & Althamthami. *The effects of zinc acetate, zinc chloride and sulfate zinc precursors on the preferred crystalline orientation of ZnO thin films obtained by SILAR technique*. Le 2ème colloque national de chimie (CNC2@2024), M'sila.
6. Mokrani, N., Temam, E. G., Temam, H. B., Barkat, H., & Althamthami. *SILAR Method Derived Sr-doped ZnO Thin Films: Effect of Different Additives on the Efficient Removal of Antibiotics with Visible Light*. 58th ISTANBUL International

Conference on Research in “Science, Engineering and Technology” (IRSET-24) December2024 / Istanbul, Turkey.

Other works not included:

1. Barkat, H., Temam, E. G., Ben Temam, H., Mokrani, N., Rahmane, S., & Althamthami, M. (2024). Enhancing sunlight-driven photocatalysis: high transparency and hydrophilic advancements in Ba-Doped ZnO thin films. *Journal of Materials Engineering and Performance*, 1-14.
2. Barkat, H., Guettaf Temam, E., Ben Temam, H., Mokrani, N., Rahmane, S., & Althamthami, M. (2025). Thickness-dependent photocatalytic performance and wettability of barium-doped ZnO thin films synthesized via SILAR technique. *Transition Metal Chemistry*, 1-20.